NORTHWESTERN UNIVERSITY

Supramolecular and Covalent Polymer Hybrids

A DISSERTATION

SUBMITTED TO THE GRADUATE SCHOOL
IN PARTIAL FULFILLMENT OF THE REQUIREMENTS

For the degree

DOCTOR OF PHILOSOPHY

Field of Materials Science and Engineering

By

Thomas J. Cotey

EVANSTON, ILLINOIS

June 2022

Abstract

Supramolecular and Covalent Polymer Hybrids

Thomas J. Cotey

The development of functional materials with rationally designed hierarchical structure is an interdisciplinary challenge. Looking to nature for inspiration, we use small molecules that engage in directed self-assembly through carefully tuned intermolecular interactions to construct materials that have structure at multiple length scales. In this work, supramolecular structures formed using peptide amphiphiles (PA) are used to create novel biomaterials. First, this work examines the formation of bulk gels through the interfacial complexation of PA nanofibers with an oppositely charged covalent polymer. These gels were formed by the rapid mixing of solutions, one containing negatively charged PA nanofibers and the other the positively charged biopolymer chitosan. During mixing, complexation occurs at the interface of the two solutions, leading to the formation of a contact layer that locks in the fluid structure formed during mixing, yielding a hydrogel with a lamellar microstructure and many internal interfaces between the supramolecular and covalent components. The nanofiber morphology of the PA is essential to this process because gels do not form when solutions of supramolecular assemblies form spherical micelles. We found that rheological properties of the gels can be tuned by changing the relative amounts of each component. Furthermore, both positively and negatively charged proteins are easily encapsulated within the contact layer of the gel. Building off these findings, we sought to gel peptide amphiphiles during flow using controlled laminar flow in flow focusing microfluidic devices. PA fibers align in the flow direction, and a solution of inorganic multivalent ions is used to gel the PA

stream within the microfluidic device, leading to the continuous formation of a highly aligned microgel that we termed a "superbundle." We explored the processing parameter space of this flow-focusing microfluidic system and developed design rules for producing superbundles with a variety of supramolecular nanofibers and gelators. We found that high concentrations of PA nanofibers as well as high volumetric flow rate ratios between the gelator flow and the PA flow were necessary to form superbundles. We noted a remarkable similarity between the superbundles structure and the structure of the extracellular matrix, the biological framework that provides an environment which supports cellular migration, proliferation, and differentiation. In addition to mimicking the structure of the extracellular matrix, we demonstrated the superbundles' ability to encapsulate a range of proteins. Using lessons learned from the preceding studies, we investigated the ability to form superbundles using complexation with covalent polyelectrolytes as well as other peptide amphiphiles as gelators. We confirmed the general design principles that we developed for microfluidic production of superbundles using inorganic multivalent ions were relevant for a broad range of gelators. The structure of the supramolecular polymer, high supramolecular polymer concentration, and the confinement of the supramolecular polymer solution by an impinging gelator flow were all crucial to the formation of superbundles regardless of the gelation mechanism used. We also demonstrated that both negatively and positively charged proteins can be encapsulated in superbundles made by complexing covalent and supramolecular polymers as well as those formed by complexing oppositely charged supramolecular polymers. Collectively, the systems investigated in this work demonstrate that rationally designed processing methods can be used to create a diverse set of supramolecular materials with tunable chemistry and hierarchical order.

Acknowledgements

Professor Sam Stupp – Thank you for bringing me into this lab and giving me the opportunity to explore my scientific passions. The Stupp Laboratory is truly special; researchers here are given enormous freedom to pursue their goals in an incredibly collaborative environment. This has been a time of both personal and professional growth, and I'm thankful for all the support that I've received.

Professors Ken Shull, Monica Olvera de la Cruz, and Nathan Gianneschi – Thank you for contributing your time to serve on my committee and providing helpful advice and feedback.

Research Associate Professor Liam Palmer – Thank you for all of the advice that you've given me through the years. You're an essential resource to getting up and running in the group and I've always enjoyed stopping by your office for impromptu science discussions. Your assistance with paper writing is also very much appreciated.

Hiroaki Sai – I was incredibly fortunate to have you as a mentor during my time in graduate school. Few are lucky enough to have a mentor that is so supportive and inquisitive. Whenever I had a problem or question, you always took the time to talk me through (or out of) any crazy idea I had. You've shown me the importance of thinking both critically and creatively about scientific problems. You've pushed me to be the best scientist I can be and taught me that there is always more to be learned.

Eric Bruckner – Thank you for always being there. We didn't know each other that well before we got here, but at this point it's hard to imagine going through grad school without you. Whether it was about science or otherwise, you were always helping with any problem. Graduate school is a lot easier when there's a friend along for the ride.

Jack Kolberg-Edelbrock – Thank you for welcoming me into the lab and for our fruitful collaboration. I can't imagine a better partnership. You're always there to pick up the slack, and you're always there to help when I need it. Who would have thought after meeting at Case all those years ago, we'd be doing this?

Allie Kolberg-Edelbrock – Thank you for helping me figure out how to navigate the start of graduate school. I didn't make it to the downtown campus too often but it was always fun to chat and get lunch.

Mark Hendricks – Thank you for being a constant source of joy, merriment, and wisdom. Whenever I wanted to learn or just talk, I knew all I had to do was go find you.

Ivan Sasselli – We've really been through it. Thank you for all your help, some of our projects didn't work out the way we hoped, but we still had a great time together.

Adam Dannenhoffer – Thank for all of the advice and scientific discussion as well as all of the good times in and outside of lab

Cara Smith – Thank you for all of the helpful chats and all of the support. It was nice to see a friendly face when I made the trek downtown.

James Passarelli – Thank you for everything. It rare to find someone so kind and helpful who asks for no thanks or acknowledgement. I could always count on you when I needed help, and I could always look to you for advice and perspective. The Cook labs just weren't the same without you.

Cynthia Perez, Steven Ma, and Litsa Kapsalis – Thank you for all of the hard work and fantastic contributions. I was lucky to have undergraduate students that were so dedicated and creative. You

all brought energy to the lab that made me want to do my best. Mentoring was a learning experience for me too, so thank you for being part of that journey.

Laura Fields and Maura Walsh – Thank you so much for your hard work and help throughout this whole process from the start of graduate school. You make all the work in our lab possible and your support is truly appreciated.

Ashwin Narayanan – Thank you for all of the helpful discussions and wisdom throughout the years.

Garrett Lau – Thank you for all the chats and help in the lab. I always enjoyed talking through ideas and getting your help crafting experiments.

Nick Sather – Thank you for all of the help getting started in the lab and helpful discussions about science and engineering.

Kristen Wek – Who would have thought after the short stint at VT we'd end up working together. It's always been fun dreaming up engineering solutions only to find more challenges.

Jacob Kupferberg – Thanks for making lab a fun place. If I ever want to talk through an idea, I know I can count on getting a good perspective from you.

Luka Đorđević – Thank you for all of the helpful discussions and support over the years. I count myself lucky to have worked with you. You bring a sense of humor to the lab as well as remarkable ideas and feedback.

Ruth Lee – Thank you for being so kind and encouraging. Thanks for always helping whenever I asked.

Oliver Dumele – Thank you for all of the good times and fantastic scientific discussions.

Zach Thompson, Kelly Parker, Will Kellogg, and Daniel Hickox-Young – Thank you for all the support and fun throughout graduate school. Whether we were planning some MSSA event, studying for an exam, playing DnD, or just hanging out, it was always a good time.

Will Brenn, Patrick Thomas, Katie Rose, Alex Prossnitz, Susan Kozawa, Megan Zangara, and Madeline Gelb – The polymer squad. Need I say more? Thank you for all of the good times and all of the support.

Mark Karver, Chris Tarcyznski, Charles Bressan, Emily Testa, and Suvendu Biswas – Thank you for all of the help with PA synthesis.

Samuel, Hannah, Sara, and Liam – Thank you for all the support. Few people have as many or as good of siblings as I do. You've made me feel lucky my whole life.

Grandma and Grandpa – Thank you for all the love. You showed me the importance of dedication, hard work, and positivity.

Mom and Dad – Thank you for always being there for me. You've pushed me to be my best and try my hardest. You're always understanding and always there to lend an ear whenever I call. It's easier to take a risk and challenge myself when I know there's a loving home waiting for me.

List of Abbreviations

BSA	Bovine Serum Albumin
CPD	Critical Point Drying
DCM	Dichloromethane
dECM	Decellularized Extracellular Matrix
DMF	Dimethylformamide
ECM	Extracellular Matrix
EGF	Epidermal Growth Factor
FITC	Fluorescein Isothiocyanate
Fmoc	9-Fluorenylmethoxycarbonyl
HA	Hyaluronic Acid
HPLC	High Performance Liquid Chromatography
LCMS	Liquid Chromatography-Mass Spectrometry
MAX	Maximum Intensity Projection of Confocal Laser Micrograph
MW	Molecular Weight
PA	Peptide Amphiphile
PBS	Phosphate Buffered Saline
PDMS	Polyditheylsiloxane
PEC	Polyelectrolyte Complex
POM	Polarized Optical Microscopy
PTFE	Polytetrafluoroethylene
SB	Superbundle

SEM	Scanning Electron Microscopy
TAMRA	5-Carboxytetramethylrhodamine
TEM	Transmission Electron Microscopy
TFA	Trifluoroacetic Acid

Table of Contents

List of Figures

List of Tables

CHAPTER 1: Introduction

1.1 Supramolecular Chemistry and Materials

Macromolecular science has revolutionized the world, affecting nearly every aspect of human life. Hermann Staudinger pioneered research in field of polymer science by hypothesizing the existence of large molecular weight molecules that were made of long chains of repeating monomeric units linked together via covalent bonds.[1] This amazing discovery would earn Staudinger the Nobel Prize in chemistry in 1953. Later in the twentieth century, the new field of supramolecular chemistry, which studied weak, non-covalent intermolecular interactions, emerged. Supramolecular chemistry and the development of the field of directed self-assembly have greatly increased the scope of soft matter research. Hierarchical self-assembly, the formation of organized supramolecular structures at multiple length scales from individual molecules via noncovalent interactions, has been of high scientific interest for decades and remains a deeply active field of study. Due to their tunability and responsiveness, self-assembled materials have applications ranging from energy storage[2,3] to regenerative medicine.[4,5]

Self-assembly occurs due to noncovalent interactions between molecules.[6] The diversity of potential supramolecular polymers is shown in Figure 1.1. Self-assembled structures usually involve a combination and balance of multiple interactions. For instance, multi-domain peptides self-assemble into nanofibers and have molecular designs that consider the interplay between hydrogen bonding, hydrophobic interactions, as well as other parameters such as electrostatic repulsion.[7] In another example, the Stupp group reported the supramolecular self-assembly of a perylene monoimide amphiphile into crystalline ribbons that can be used to create scaffolds for

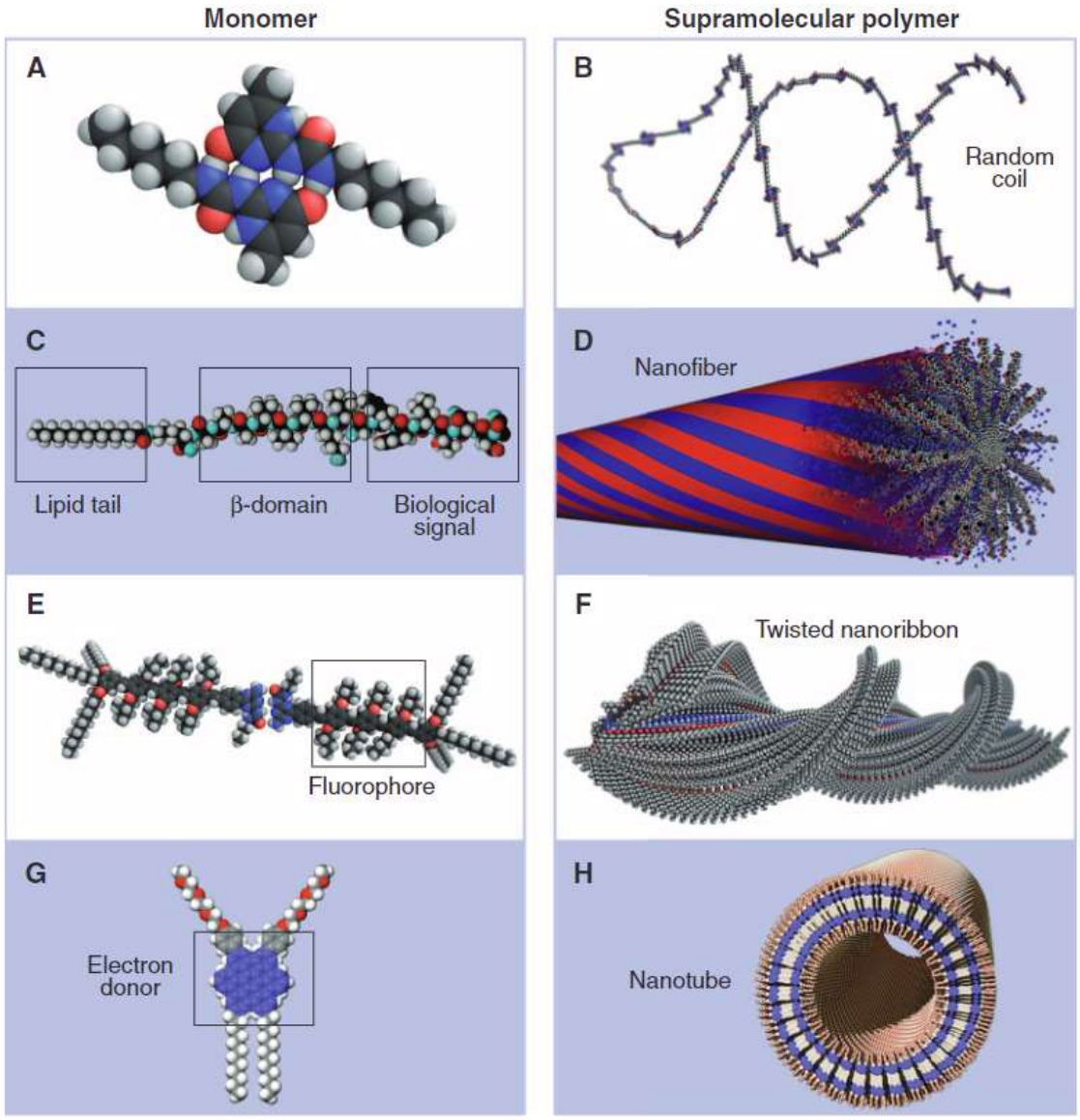

Figure 1.1: Schematic depicting supramolecular monomers (A,C,E,G) as well as the supramolecular polymers (B,D,F,H) that they assemble into. Careful molecular design leads to the formation of a diversity in supramolecular structure. Image reproduced from Stupp *et al.*[8]

photocatalytic hydrogen production.[9] The self-assembly of these molecules is dependent on electrostatic screening, dipole-dipole associations, hydrophobic forces, and π–π stacking. When considering the dimensionality of the supramolecular structures formed via self-assembly, the results are equally diverse. Supramolecular materials can be formed that are zero dimensional in

the case of liposomes,[10,11] micelles[12–14], and small clusters.[15] There are a great many one-dimensional supramolecular materials such as fibers[8,16–20], cylindrical micelles[21–23], tubes[24–26], and ribbons.[27–30] Two-dimensional structures can also be formed using self-assembly.[31–34] Additionally, one-dimensional or two-dimensional assemblies can be used to form three-dimensional networks.

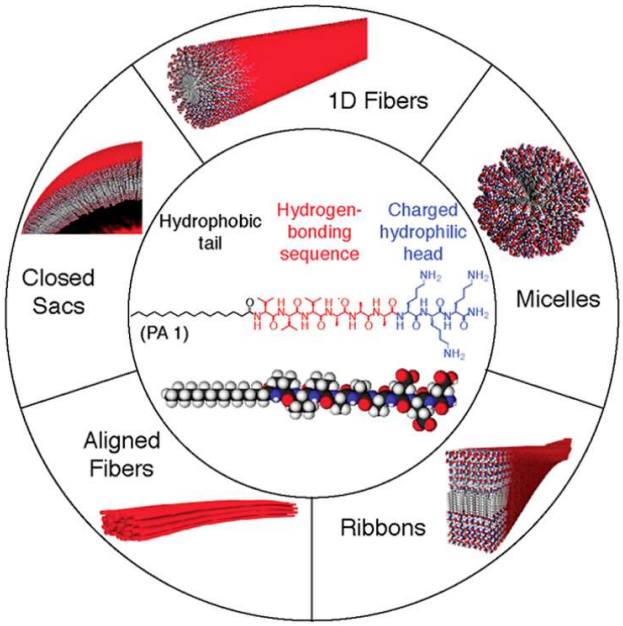

Figure 1.2: PA general chemical structure is shown (middle) surrounded by the possible assembly states that can be achieved by tuning PA chemical structure as well as environmental factors such as pH and salt concentration. Figure reproduced from Hendricks et al.[35]

Biological structures and chemistries are a tremendous source of inspiration for scientists interested in supramolecular assembly. Proteins are critical in biological systems and play important roles in biochemical processes as well as structural functions necessary for supporting life. Proteins are biopolymers composed of amino acids that are linked by amide bonds, also known as peptide bonds. The multitude of combinations in which amino acids can be ordered in their

primary structure, the different secondary structures that the polypeptides can take, the three dimensional shape also known as the tertiary structure, as well as the way in which proteins can arrange themselves together in their quaternary structure leads to incredible complexity in protein systems.[36] Proteins therapies and protein delivery has received large amounts of interest from researchers due potential in medicine for treatments, diagnostics, vaccines, and other applications.[37–39] Futhermore, peptide assembly is a subject of great interest due to the potential to achieve desired biological responses in controllable and carefully designed chemical systems.[40] In addition to peptides composed solely of amino acids, other systems that involve synthetic schemes to include other chemical functionalities are also advantageous. One example in particular that has garnered significant attention is class of molecules called peptide amphiphiles (PAs).[5] The varied self-assembly states of PAs are shown in Figure 1.2. Peptide amphiphiles are composed of amino acid chains that are modified with hydrophobic groups such that the molecule has hydrophilic and

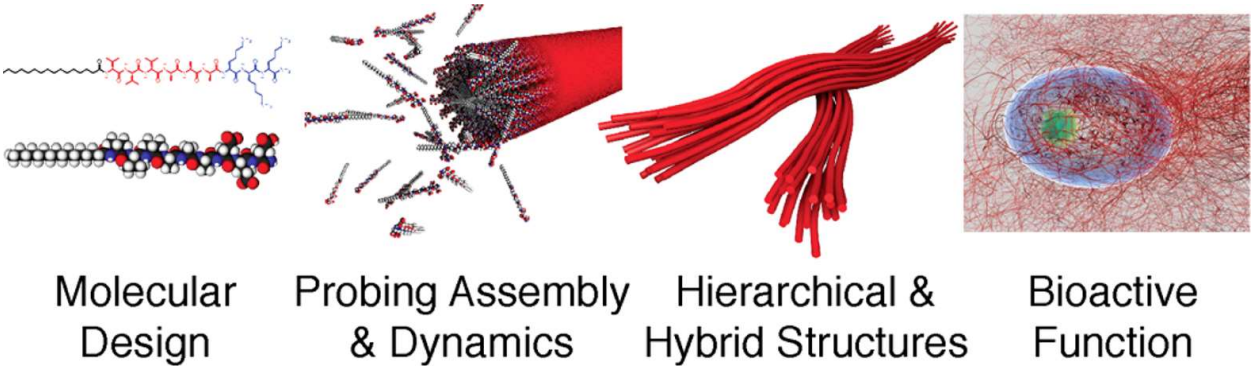

Figure 1.3: Molecular design is used to tune assembly, dynamics, and hierarchical structure of peptide amphiphiles in order to impart specific biological function. Image reproduced from Hendricks *et al.*[35]

hydrophobic regions. While there is earlier work from the Tirrell group that showed the solid-phase synthesis of PAs for use in the formation of monolayers and membranes,[41] the Stupp Laboratory has meticulously studied PA nanostructures that utilize competing interactions

between charged peptide sequences that promote solubility and β-sheet forming peptide sequences that promote intermolecular hydrogen bonding.[4,42,43] The first example that showed PAs self-assembling into long nanofibers was in a 2001 report from the Stupp Laboratory.[19] In this work, it was shown that changes in pH could lead to the self-assembly of PAs into a scaffold of fibers that the authors remarked was similar to extracellular matrix. Further biomimicry was shown by directing mineralization of hydroxyapatite on the self-assembled fibers. The alignment was similar to that found in bone between hydroxyapatite and collagen fibrils.[19] Additionally, the PAs could be reversibly crosslinked by using the formation of disulfide bonds.[19,44] This foundational work inspired future study of PAs in scaffolds for regenerative medicine. One of the first such works was published in 2004 and showed that PAs could be designed to include a bioactive peptide epitope, self-assemble in aqueous media, and form gel networks.[45] By including bioactive epitopes on the PAs, the gels were intended to be capable of presenting large amounts of signal for cells on and in the gels. Cells were encapsulated in the gels and had good viability for large amounts of cells over long periods of time. The peptide epitope that was chosen was IKVAV, a sequence found in laminin that positively affects neurites. The cells encapsulated in the scaffold experienced quick and selective differentiation into neurons, demonstrating the promise of this system in biomedical applications.[45] By tuning molecular structure and self-assembly, researchers are able to elicit specific bioactive function (Figure 1.3). Further works have shown the utility of peptide amphiphiles in bone regeneration,[46–48] neuro-regeneration,[17,49,50] and cardiovascular applications.[51,52]

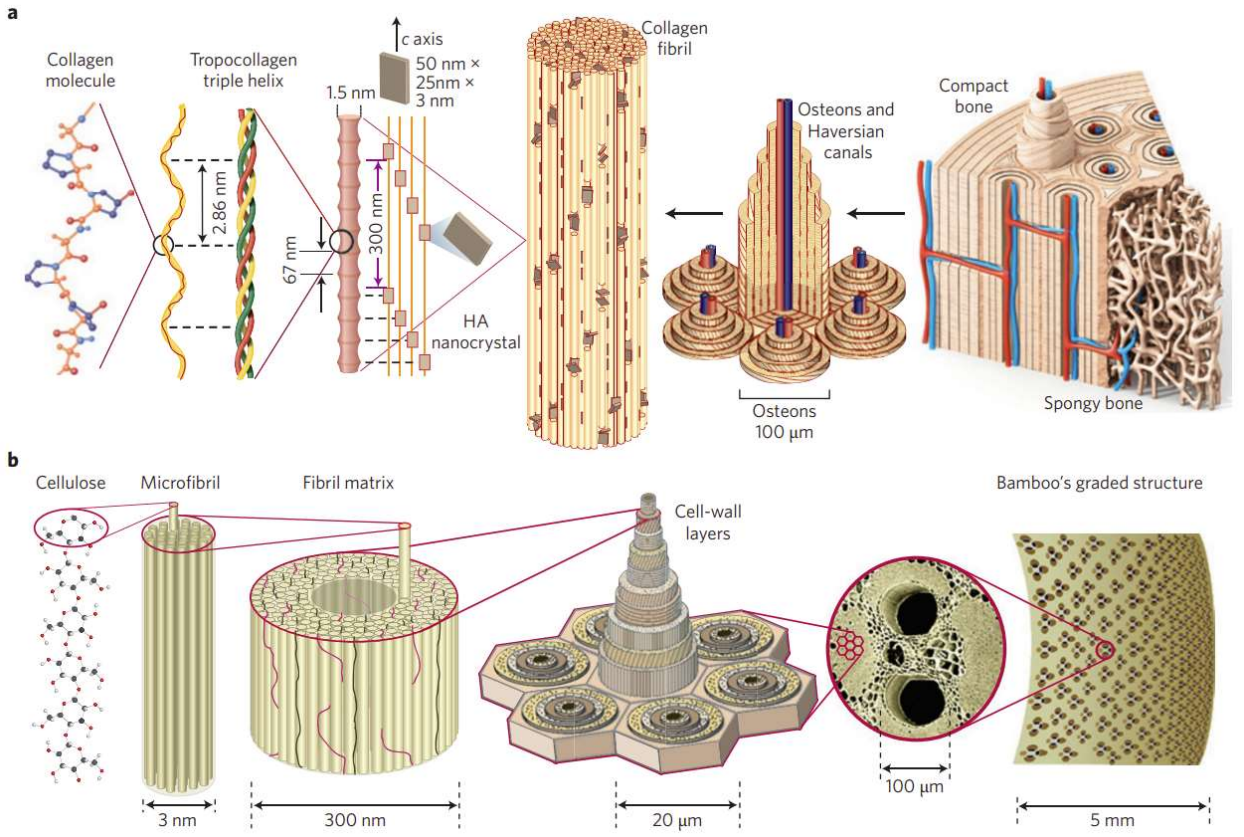

Figure 1.4: The anisotripic hierarchical structure of both (a) bone and (b) wood ranging from the molecular level to the microlevel. The orientation of polymers at the molecular level leads directly to the features seen in the nano-level which leads to the structure at the microlevel. These structures lead to material properties that enable their biofunctions, where bone and wood are able to act as lightweight structural materials. Figure reproduced from Wegst *et al.*[53]

Hierarchical structure is often sought or achieved serendipitously in supramolecular systems and is of great interest to researchers due to the effects on material properties and function. Hierarchical structure involves the organization of structure at many length scales, or simply put, hierarchical materials have structural features which have structure themselves at other length scales.[54] There are both natural and manmade hierarchical materials.[53] Muscle is commonly cited example of a natural hierarchical material. In muscle, there are highly ordered proteins, actin and myosin, that form filaments via self-association that can be either thick or thin. These filaments

assemble into sarcomeres, which link to form myofibrils. These myofibrils connect and align to form the interior of muscles. This complex structure has features at several length scales, and the alignment of these features at multiple length scales within muscle tissue gives rise to the anisotropic material properties and function.[55] There are many other naturally occurring hierarchical materials including wood and bone, as shown in Figure 1.4, and the hierarchical structure of these materials also has profound effects on their mechanical properties.[53,56] Scientists also use hierarchical biological materials as sources of inspiration for synthetic supramolecular material design. For example, Chin *et al*. reported the creation of supramolecular hydrogel tubes that showed anisotropic actuation due to thermal stimulus, and the material was inspired by skeletal muscle structure and function. In order to make the hydrogel tubes, a solution of supramolecular fibers was aligned using shear force. These fibers were used as a scaffold for polymerization of covalent polymers that were thermoresponsive. The anisotropy of the hydrogel tubes stems from the hierarchical structure.[57] In another work, gelation of PAs during manual extrusion using a pipette was used to make aligned monodomain gels. This resulted in the formation of a gel millimeters in diameter, with a gel architecture made up of microfibers that were composed of peptide amphiphile nanofibers. Interestingly, The aligned hierarchical structure of this material was shown to direct the growth of cells in the network, showing how controlling the hierarchical structure can have important biological implications.[58]

1.2 Polymer-Peptide Amphiphile Membranes and Complexes

Though aqueous solutions of peptide amphiphile nanofibers have shown great promise many applications, the ability to form materials with solid-like mechanical properties, greatly expands the scope of potential clinical targets. Generally, peptide amphiphile nanofibers have

charged surfaces, and they are easily gelled via the addition of oppositely charged multivalent inorganic ions,[59,60] i.e., a concentrated solution of negatively charged PA nanofibers can be gelled with a solution containing Mg^{2+}, Ca^{2+}, Al^{3+}, etc. While gelation using inorganic ions is the most common way to prepare peptide amphiphile materials with solid-like mechanical properties, oppositely charged covalent polymers can also be used, as first reported by Capito *et al.* in 2008.[61] In this work, a solution of the positively charged PA C16V3A3K3 (K3) was complexed with a solution of the negatively charged covalent biopolymer hyaluronic acid (HA). Once the solutions were brought into contact, an interfacial layer formed as a result of the electrostatic interactions between the negatively charged covalent polymer and the positively charged supramolecular nanofiber (Figure 1.5). After the contact layer formed, an osmotic pressure difference between the HA and PA solutions led to the diffusion of the HA into the PA compartment. This osmotic pressure difference can be described by the following equation.

$$\Delta\prod \equiv \prod HA - \prod PA = k_B T \sum_i n_i \left(e^{-\frac{e v_i \Psi(R)}{k_B T}} - 1 \right)$$

$\Delta\prod$ is the difference in osmotic pressures, k_B is the Boltzmann constant, n_i is the concentration of mobile ions, v_i is the valence of mobile ions, R is the Wigner cell radius, T is the temperature, and $\Psi(R)$ is the local electrostatic potential. This diffusion driven by this osmotic pressure difference is described by the following expression.

$$\frac{\partial}{\partial t} w(s,t) = D_o \frac{\partial}{\partial s} \left[\frac{\partial}{\partial s} + \frac{\Delta\prod \lambda b^2 - F}{k_B T} \right] w(s,t)$$

In this expression, w(s,t) determines the probability at time t that a segment of s monomers of a polymer chain have based through a diffusive barrier, λ is the thickness of the diffusive barrier, $F \propto k_B T \ln(N\text{-}s)$ is the entropic free energy of a chain with N repeat units that has s monomer units

that passed through the diffusive barrier, and D_o is the bare diffusion coefficient. Capito *et al.* reported that this diffusion of the covalent polymer into the PA solution resulted in the nucleation of self-assembly of PA fibers, which grew perpendicular to the initial interfacial contact layer, leading to the growth of the membrane over time. This led to the formation of three zones in this hierarchical membrane, an amorphous layer, a layer with nanofibers parallel to the interface, and a third region with nanofibers that grow perpendicular to the initial layer. By injecting one solution into the other, a sac can be produced, and by layering one solution on top of the other, a planar membrane can be formed. Additionally, the authors found that the K3-HA sacs could support the *in vitro* culture and differentiation of human mesenchymal stem cells, demonstrating the utility of PA-polymer membranes in bioapplications.

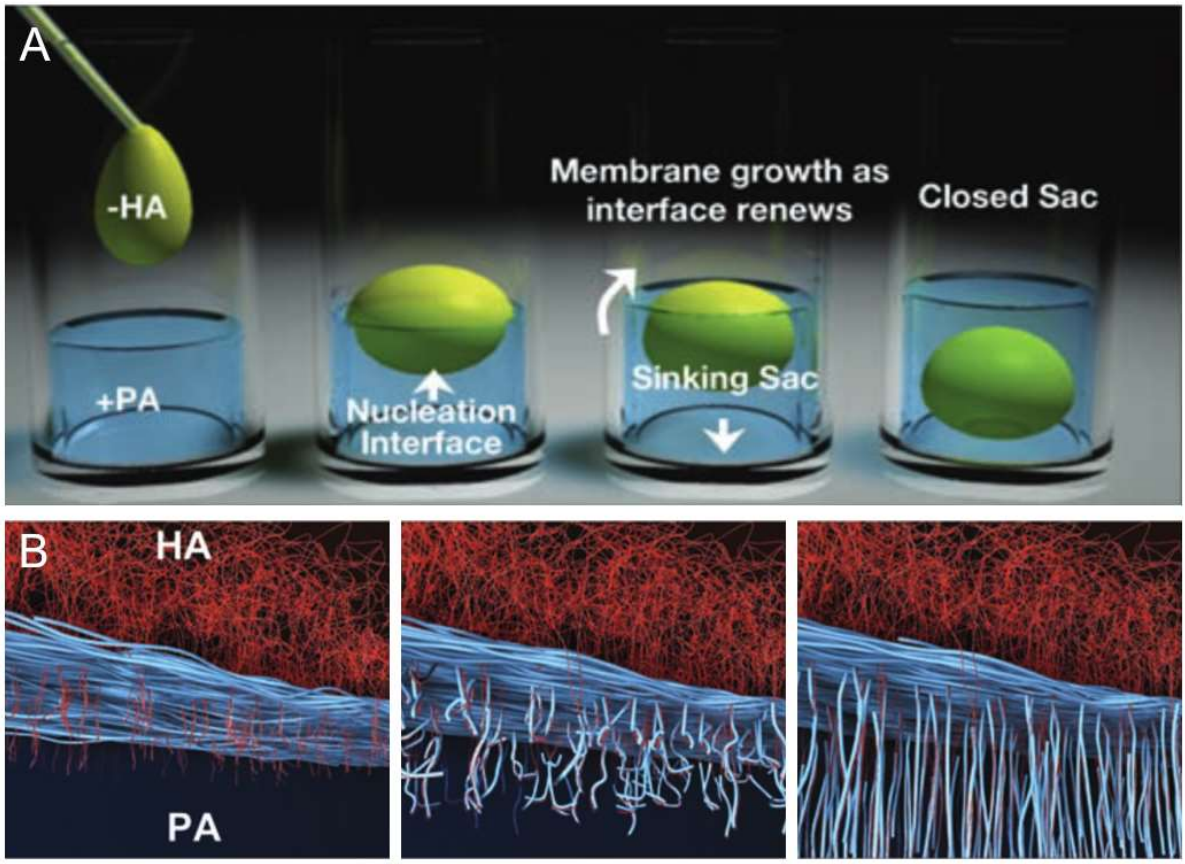

Figure 1.5: (A) A schematic that depicts the formation of a membranous sac when a solution of the negatively charged polymer hyaluronic acid is pipetted into a solution of positively charged PA. Nucleation occurs at the interface followed by growth of the membrane and the closing of the sac. (B) A schematic that depicts the interface at the nano-level. Hyaluronic acid chains diffuse into the PA compartment where it leads to growth of fibers perpendicular to the interface and complexation with the PA. Figure adapted from Capito *et al.*[61]

In a subsequent work by Carvajal *et al.*, the physical properties of K3-HA membranes were studied.[62] Osmotic swelling and membrane inflation experiments showed that increased incubation time during the production of the membrane as well as higher concentrations of HA increased the area modulus of the hierarchical membranes. Scanning electron microscopy (SEM) taken at different incubation times with varied HA concentration showed that the membrane was growing over time due to the diffusion of HA into the PA compartment. Additionally, the longer incubation

times led to a decrease in the permeability of the membranes. In a study by Bitton *et al*. it was shown that hierarchical PA-polymer membranes with structures described previously could be formed with a range of oppositely charged polyelectrolytes, so long as the polyelectrolytes were sufficiently charged so as to induce rapid interfacial aggregation. Relatively weaker interactions between the polyelectrolytes and the oppositely charged PAs led to the formation of PA-polymer membranes with dramatically different internal structures.[63] In addition to work displaying electrostatic control of these hierarchical membranes, it was found that electric fields could be used to control the structure of the membranes as well. Specifically, the presence of an electric field can induce a compressive field or a pulling field, and these fields will lead to either the promotion of diffusion the suppression of diffusion, respectively, of the complexing species through the diffusion barrier. This control of diffusing species allowed for the control of the kinetics of membrane growth as well as control over the morphology membranes.[64] Further study into complexation between oppositely charged peptide amphiphile fibers and covalent polymers showed that layer-by-layer films could be produced with alternating layers of peptide amphiphiles and covalent polymers.[65] Interestingly, a system that utilized complexation between peptide amphiphile nanofibers and elastin like protein that undergoes conformational changes produced a membrane that had dynamic morphogenesis.[66] To demonstrate that these materials could be useful in bio-ink applications, Hedegaard *et al.* used a droplet on demand system to jet a droplet of PA into a solution of keratin that complexed the PA (Figure 1.6). Due to the hydrodynamic forces that resulted from the droplet of PA hitting the gelling solution, a toroidal structure formed that was then locked in place by complexation with the polymer keratin. These toroidal structures could be printed in patterns and arranged into specific shapes.[67] While previous studies into the

complexation of oppositely charged covalent polymers and peptide amphiphile nanofibers yielded fantastic functional materials, nearly all of these studies were concerned with either static solutions or the formation of single membranes, the study of complexation during flow and the formation of many interfaces is relatively unexplored.

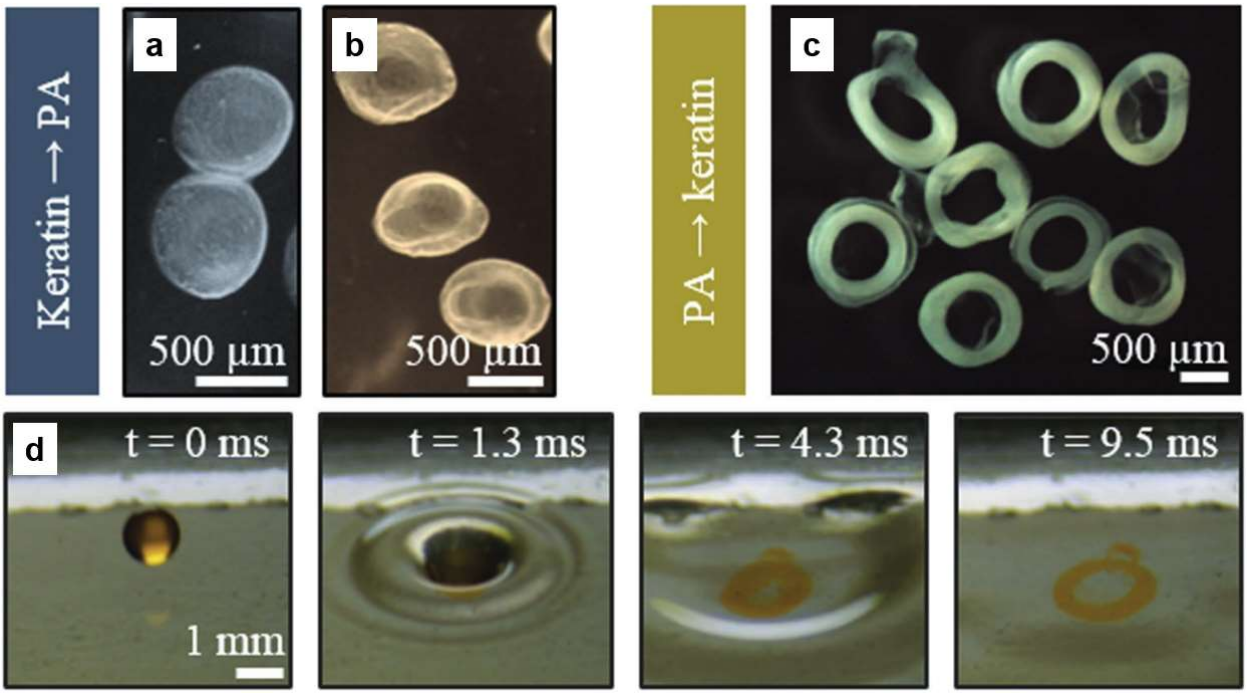

Figure 1.6: Examples of sacs made by droplet-on-demand inkjet printing with keratin at (A) 20 mg/mL and (B) 10 mg/mL being jetted into oppositely charged PA solution. (C) Examples of toroidal structures that are formed when a PA droplet is jetted into keratin. (D) Pictures depicting the formation of a toroidal structure due to hydrodynamic force during inkjet droplet printing. Image adapted from Hedegaard *et al.*[67]

In addition to investigating the physical properties of PA-polymer membranes, researchers have also investigated their use as biomaterials in multiple applications. In the seminal work on hierarchical PA membranes, the authors demonstrated K3-HA sacs could support the *in vitro* culture and differentiation of human mesenchymal stem cells.[61] A later work utilized a membrane that was formed with the polymer HA and a PA that had a peptide chain with a $(KLAKLAK)_2$ sequence.[68] This PA was termed a KLAK PA and has been shown to kill breast cancer cells with

some specificity.[69,70] When coassembled with K3 PA, the PA mixtures could be complexed with HA to form membranes that had sustained cytotoxicity against breast cancer cells, showing that these materials could be useful in anti-cancer therapies.[68] In another study, a hierarchical PA-polymer membrane was formed using HA, the biopolymer heparin, and a PA designed to display a heparin binding sequence in order to bind heparin loops that can localize angiogenic growth factors on the surface of the PA nanofibers. It was found that the HA-heparin binding PA membranes that contained heparin and growth factors had sustained growth factor release and could lead to angiogenesis in an *in vivo* model.[71] Researchers have also shown that HA-PA membranes can be useful in osteoregenerative medicine for cartilage repair. In a study by Arslan *et al.*, a hierarchical HA-PA membrane was used in both *in vitro* and *in vivo* experiments. It was demonstrated that the membranes supported stem cell culture and preserved cartilage morphology and protected cartilage tissue from deterioration, showing that these materials may be useful in clinical applications for osteoarthritis. The varied applications researchers have studied indicates the incredible breadth of PA-polymer complexes as a biomaterial platform.

1.3 Microfluidic Biomaterials and Scaffolds

Control over microstructure has been a constant pursuit in biomaterial research. Across diverse applications such as tissue engineering, drug delivery, and biosensing, the precise fabrication of materials with desired shape, size, network architecture, and material composition is critical for success. Microfluidic materials synthesis provides the ability to address these challenges through fine control of fluids in microscale devices. Diverse device fabrication methods[72–77] allow for the production of microfluidic devices with many different geometries and channel sizes with designs that can be as simple or complex as desired. Droplet microfluidics has

been of interest due to the ability to make microparticles for a myriad of applications including cell encapsulation,[78–81] drug delivery,[82–84] and the formation of artificial cells.[85–89]

Many bioapplications cannot be addressed through the use of microparticles, so alternative strategies have been developed. One area of increasing interest to researchers is the development of materials that are biomimetic, both in structure and composition. Many biological tissues and structures have been the target of biomimetic research[90–94]; a notable example is the extracellular matrix (ECM). The extracellular matrix is a three-dimensional network made up of proteoglycans, glycosaminoglycans, collagen, elastin, laminin, fibronectin, and glycoproteins that provides a stable environment which supports cellular proliferation, migration, and differentiation.[95–98] This dynamic matrix is ubiquitous and crucial to the structure and function of tissues and organs. Systems using fiber geometries have been of particular interest because fibers matrices more closely resemble the structure of biological tissues than spherical particles. The formation of fibers using microfluidics has recently been the subject of great attention.[99–104] The process generally involves a continuous flow of a precursor solution which is composed of monomers, polymers, or macromolecules. After injection into the microfluidic device, the precursor solution is surrounded by a sheathing solution. This is often referred to as a "core-sheath" flow. The sheath flow must prevent the core flow from sticking to the device channel walls, and in conjunction with the channel geometry, the sheath flow is responsible for the shaping of the core flow while the core flow undergoes a solidification/gelation process that results in fiber formation. This shaping is usually referred to as "hydrodynamic focusing" or "flow focusing."[99–101] After solidification/gelation, the fiber is extruded from the device in a continuous process. Device geometries can broadly be grouped into cross-flow geometries,[105–111] concentric-flow

geometries,[112–119] and three-dimensional shaping geometries.[120–124] There are also a breadth of methods used for the solidification of the microfluidic fibers as shown in Figure 1.6 including diffusion controlled covalent crosslinking,[125,126] photochemical crosslinking,[120,123,127,128] and ionic crosslinking.[111,113,129–134] The diversity of available chemistries and device geometry leads to an incredible wealth of microfluidic material systems.

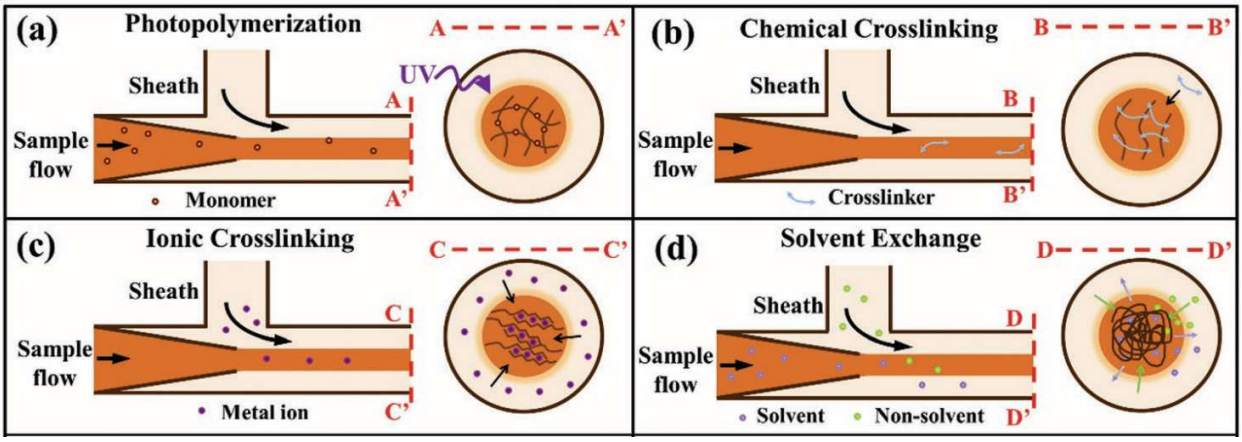

Figure 1.7: microfluidic fiber solidification strategies include (A) photopolymerization, (B) chemical crosslinking, (C) ionic crosslinking, and (D) solvent exchange. Figure adapted from Du *et al.*[101]

Fibers produced using microfluidic fabrication have been the subject of biomaterials research for over a decade. Drug encapsulation and delivery has been an area of interest for these microfibers. In the seminal work by Beebe *et al.*, the enzymes horseradish peroxidase and glucose oxidase were trapped within the fibers in order to demonstrate that the fibers could be used as biosensors. Subsequent studies have shown that microfluidic microfibers can encapsulate a range of proteins[135] as well as small molecule drugs,[136] with some of these systems demonstrating controlled drug release.[137,138] In addition to encapsulating proteins and drugs, the ability to encapsulate cells has been researched extensively.[99,101] In one such study by Wei *et al*., cells were

encapsulated within a tunable microfiber made with alginate functionalized with RGD to promote binding, and the microfiber could be manipulated into desired shapes.[139] A subsequent work demonstrated that by orienting collagen fibers using flow in the microfluidic device, cell orientation could be directed in the microfiber.[140] By producing hollow helical microfibers that encapsulated cells, perfusable blood vessel mimics were created, showing the importance of diverse microfluidic architectures when encapsulating cells.[141] Microfluidic microfibers have also been used in neuroregenerative research. Kim *et al.* showed that the encapsulation of astrocytes within an RGD-alginate microfiber could accelerate the outgrowth of neurites seeded on the fiber, showing the interesting interplay between cells seeded within as well as upon wet-spun microfluidic fibers.[142] In addition to cell encapsulation, other studies have demonstrated that cells could be seeded on the fibers as well.[113,132,143,144] Through the diverse materials chemistry, tunable geometry, and gentle biofriendly synthesis, fibers produced using microfluidics are a promising material platform for a wide range of bioapplications including biosensing, tissue engineering, and drug delivery.

1.4 Thesis Overview

This thesis is based on developing novel soft materials with hierarchical structures by controlling the gelation of supramolecular assemblies. Using nature as inspiration, we use self-assembling molecules composed of peptide chains that are modified with a hydrophobic tail to make functional materials with structure at multiple length scales by controlling chemistry, intermolecular interactions, as well as solution dynamics.

This work begins with the formation of bulk hybrid hydrogels using supramolecular nanofibers and a covalent polyelectrolyte. In Chapter 2, the complexation of oppositely charged

supramolecular and covalent polymers during flow is shown to lock in the fluid structure that develops during rapid mixing. This results in the formation of a gel with a sheet-like architecture with interfaces that display morphological separation between the supramolecular and covalent polymer. We found that the nanofiber structure of the supramolecular polymer was crucial to the formation of these gels, as gels are unable to form when supramolecular micelles were used. Additionally, the gels' rheological properties could be tuned by varying the concentrations of supramolecular polymer as well as the mixing ratio of covalent and supramolecular polymers. Finally, we probed the ability of the hybrid hydrogels to encapsulate protein and found that negatively and positively charged proteins could be encapsulated and localized within the dense contact layer of the hydrogel.

In Chapter 3, peptide amphiphile nanofibers are gelled during a controlled laminar flow using multivalent inorganic salts, drawing a striking contrast to the flow conditions used for gelation in Chapter 2. A flow-focusing microfluidic device with cross flow was used to create a highly aligned peptide amphiphile core flow that was gelled with a variety of inorganic multivalent ions. This continuous extrusion technique resulted in the creation of microgels that we termed "superbundles." Using electron microscopy, we found remarkable morphological similarity to decellularized extracellular matrix. To develop design rules for producing these matrix mimetic microgels, we explored a parameter space that varied flow rates, peptide amphiphile concentration, peptide amphiphile chemistry, as well as gelator chemistry. Additionally, we demonstrated that a variety of proteins can be encapsulated in superbundles.

Chapter 4 takes inspiration from both Chapters 2 and 3 to develop materials using microfluidic gelation *via* complexation of oppositely charged peptide amphiphiles and polymers.

In this work, we take a similar methodological approach as used in Chapter 3 for gelation during flow using a flow-focusing microfluidic device with cross flow. A core flow of peptide amphiphiles is gelled using a sheathing flow of oppositely charged covalent polymer. Once again, a broad parameter space was explored by varying flow rates, peptide amphiphile concentration, peptide amphiphile chemistry, as well as gelator chemistry. Interestingly, we also found that superbundles could be produced by complexing oppositely charged peptide amphiphiles within the microfluidic device. Finally, we demonstrate that positively and negatively charged proteins can be encapsulated in superbundles produced by complexing covalent polymers and peptide amphiphiles in addition to those produced formed by complexing two solutions of oppositely charged peptide amphiphiles.

Chapter 5 concludes with a summary of the findings detailed in Chapters 2 through 4 as well as a future outlook for hybrid covalent and supramolecular materials and the next steps to advance the development of these functional materials.

CHAPTER 2: Bulk Interfacial Complexation of Oppositely Charged Supramolecular Polymers and Polyelectrolytes

2.1 Background

The mixing of oppositely charged polyelectrolytes in aqueous solution resulting in associative phase separation with polymer-rich phases is referred to as polyelectrolyte complexation.[145] These polymer-rich phases are known as polyelectrolyte complexes (PECs) and can take the form of films,[146–148] micelles,[149,150] gels,[151,152] solutions,[145,153] or precipitates.[154] PECs are prevalent in nature, such as in membrane-less organelles[155,156] and also have applications in tissue engineering[157,158] and drug delivery,[147,159,160] An obvious benefit of using polyelectrolyte complexes for biomedical applications is their spontaneous formation without requiring catalysts or initiators required in hydrogels that form through chemical reactions.[161] Most research of PECs focuses on interactions between covalent polymers, and complexation between covalent and supramolecular polymers remains relatively unexplored.

Self-assembly offers a path to create dynamic and responsive hierarchical materials with applications including regenerative medicine,[4,162] drug delivery,[163] and biosensing.[164] Peptide amphiphiles (PAs) are composed of amino acid sequences that have been modified with a hydrophobic moiety to promote their self-assembly.[19,35,41] The Stupp Laboratory has developed PA nanostructures based on the competition between strong β-sheet hydrogen bonding and a charged region that promotes solubility.[19,42,44,165,166] In water, hydrophobic collapse due to the aliphatic tail and β-sheet formation induce assembly of the molecules into one-dimensional supramolecular nanostructures.[19,35,44] These PA nanostructures have shown the ability to bind

growth factors and amplify signaling, which could enable future therapies that incorporate proteins.[47,167] The PA nanofibers have highly charged surfaces and can be gelled with multivalent ions.[59,60,168]

The Stupp Laboratory previously reported the formation of hierarchical membranes and closed sacs formed with the negatively charged polymer hyaluronic acid (HA), and the positively charged PA $C_{16}V_3A_3K_3$.[61] Due the electrostatic interactions between the negatively charged HA and positively charged $C_{16}V_3A_3K_3$, a contact layer formed at the interface of the two solutions which lead to self-assembly of PA nanofibers at the interface. The HA then diffused through the contact layer into the PA compartment, nucleating self-assembly of PA fibers perpendicular to the contact layer, which in turn lead to growth of PA-HA membrane.[61] Subsequent works explored the physical properties[62,64] of these membranes as well as their ability to be used for anti-cancer therapeutics[68] and promote angiogenesis.[71] In these examples, the two solutions were put in contact without mixing, resulting in a single, complexed interface. More recently, oppositely charged PA-polymer systems have been reported in the formation of layer-by-layer films,[65] hydrogels that develop without the formation of a contact layer,[169] printed toroidal structures,[67] and systems that undergo morphogenesis during membrane formation due to conformational changes of the polymer.[66] These examples involve bringing the solutions in contact without further mixing. We investigate here the formation of bulk gels through interfacial complexation between negatively charged PA and the positively charged polymer chitosan utilizing combination of scanning electron microscopy, confocal microscopy, X-ray scattering, rheology, and absorbance spectroscopy. Since hydrogels have been reported to aid delivery of proteins,[38,170] we also explore

the hypothesis that the emergent structure could promote encapsulation, localization, and retention of proteins within the hydrogel.

2.2 Results and Discussion

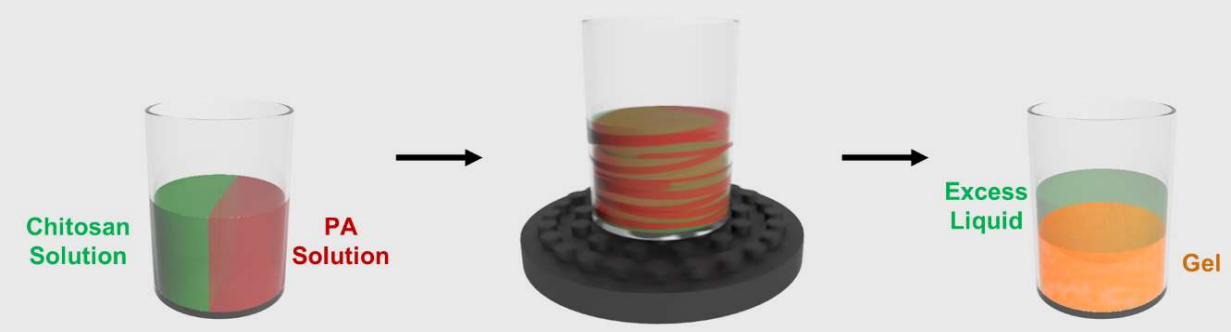

Figure 2.1: Schematic representation of gel formation by adding PA and chitosan solutions to opposite sides of a vial followed by immediate mixing.

Chitosan is a water soluble positively charged polysaccharide derived from chitin which is biodegradable, biocompatible, and previous work has investigated its use as a biomaterial for wound dressings.[161,171,172] Gels were produced using 1 wt% solutions of chitosan and PA with the sequence $C_{16}V_3A_3E_3$-OH (E3OH), which has its peptide chain terminated by a carboxylic acid group. The two solutions were added simultaneously to opposite sides of a glass vial, followed immediately by mixing with a vortex agitator, resulting in the rapid formation of a gel within chitosan rich excess fluid (Figure 2.1). As shown in Figure 2.2A-C, scanning electron micrographs of the resulting gels revealed a sheet-like morphology with fibrous textures. The structure of PA nanofibers is retained in the final gel, as shown by X-ray scattering experiments (Figure 2.2D). These sheets approach millimeter length scales in width and are micrometers thick.

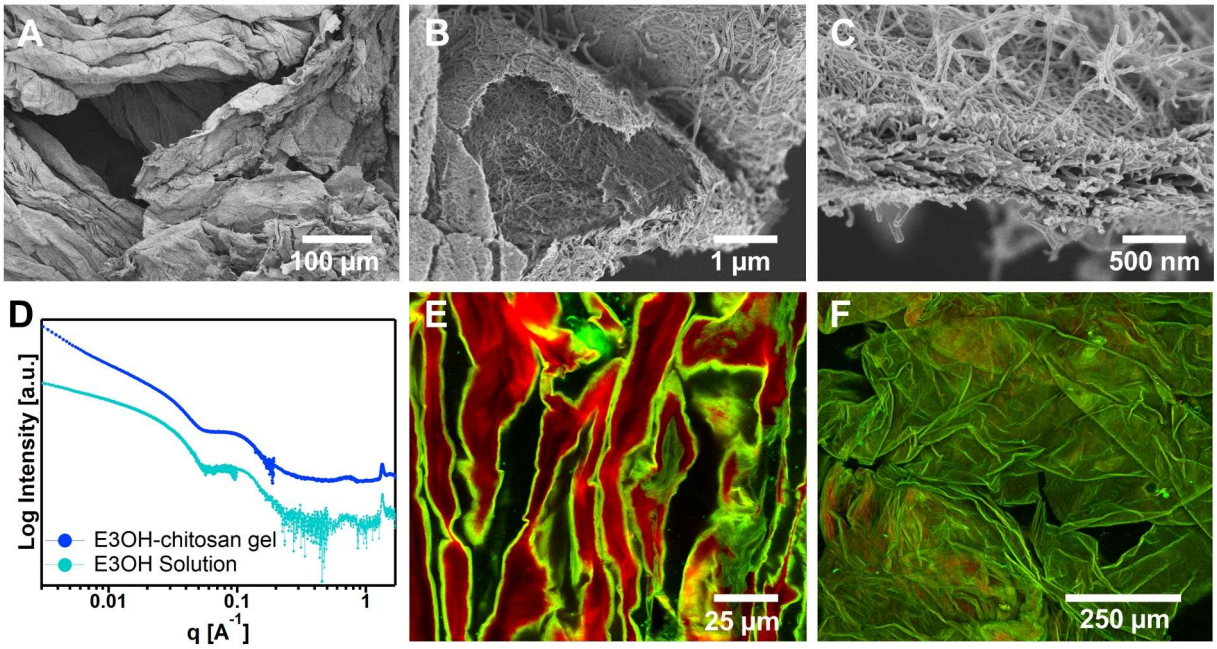

Figure 2.2: (A-C) Scanning electron micrographs of critical point dried E3OH-chitosan gels at various magnifications. (D) Small, medium, and wide-angle x-ray scattering of E3OH-chitosan gel and an E3OH solution. (E) Confocal micrograph of a gel cross section revealing the presence of PA (red channel) and chitosan (green channel). (F) Maximum intensity projection of a z-stack Confocal micrograph with PA channel in red and chitosan channel in green.

Because electron microscopy cannot determine the distribution of PA and chitosan molecules, confocal laser scanning microscopy was used to explore these domains using specific fluorescent labels on each molecule. The chitosan polymer was labeled with fluorescein isothiocyanate (FITC), and PA molecules labeled with 5-carboxytetramethylrhodamine (TAMRA). By using different dye labels for each component, it was possible to determine the extent of colocalization of both components versus separation into distinct morphologies. In the E3OH-chitosan polyelectrolytic complex, we see a clear distinction between the chitosan and the PA domains (see Figure 2.2E). Based on confocal micrographs, the PA component of the gel appears to be encapsulated by a layer of chitosan. By obtaining a z-stack in confocal microscopy, it is possible to explore the three-dimensional structure of the material. The confocal z-stack

imaging (Figure 2.2F) indeed confirmed the morphology observed by SEM. The gel is made up of sheets that are crumpled and folded over each other, and they contain PA nanofibers in their interior encased by chitosan outer layers. We hypothesize that the PA nanofibers are always found at the core of these structures because the PA solution is a higher viscosity solution composed of rigid high aspect ratio nanofibers, and during the rapid mixing process, this viscous PA solution cuts through the relatively less viscous chitosan solution. While cutting through the covalent polymer solution, the PA domains are coated with chitosan, which then complexes on the surface of these PA domains, depleting the concentration of chitosan in the surrounding fluid. Similar structures to those formed during rapid vortex mixing were also observed when mixing was performed with a dual-barrel syringe with a mixing tip (Figure 2.3).

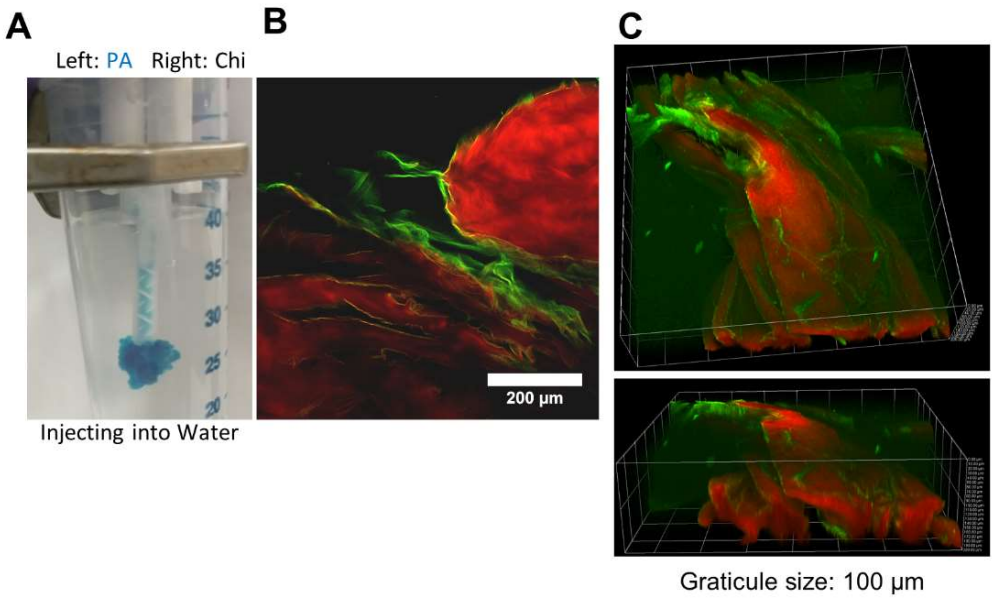

Figure 2.3: (A) 1.5% PA solution with blue food dye for contrast in left barrel of dual barrel syringe, 1 wt% chitosan solution in right barrel were injected through a mixing head attachment into water to form a gel. Water bath does not take part in gelation and was used for demonstration purposes. (B) confocal micrographs of gel prepared with dual-barrel syringe mixer (FITC chitosan in green, TAMRA-E3 in red) confocal micrograph shows similar interfacial gel structure as seen in vortex mixing. (C) 3D reconstruction of confocal microscopy z-stack of gel prepared with dual barrel syringe (FITC chitosan in green, TAMRA-E3 in red)

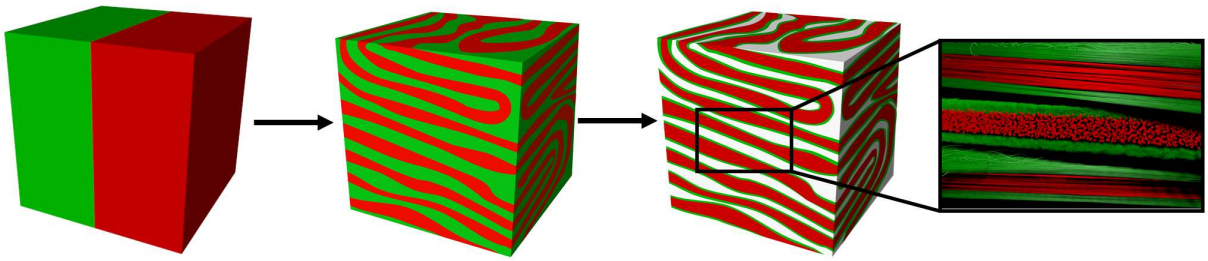

Figure 2.4: Schematic representation of the morphology formed by the positively charged biopolymer chitosan (green) and an oppositely charged PA (red). Mixing leads to stretching and folding of the fluids and results in the formation of a material with many interfaces due to electrostatic complexation at their interfaces, which prevents further mixing and locks a nonequilibrium structure. The spaces between the lamellae, shown in white in the third cube and shaded in the zoomed inset, are composed of fluid in the final gel.

Chaotic mixing of both components is characterized by the generation of increasing amounts of interfacial area between them as well as the development of a lamellar fluid structure [173–175] as shown schematically in the first transformation of Figure 2.4. The deformations that fluids experience during chaotic mixing are commonly referred to as "stretching and folding," and the amount of interfacial area generated is related to the amount of stretching experienced by the fluid elements.[173,174] If the fluids are miscible, extensive mixing eventually results in the formation of a homogeneous phase. During the mixing of chitosan and the oppositely charged PA, we observed complexation at the interfaces of the two fluids, leading to the formation of robust contact layers that lock in the striations that make up the lamellar structure of the mixing fluids as depicted schematically in Figure 2.4, preventing further chaotic mixing from taking place between each fluid. As a result, the rapid interfacial gelation leads to nonequilibrium, sheet-like structures composed of both PA and chitosan. Though this complexation relies on strong electrostatic interactions between the PA nanofibers and the covalent polymer; thermodynamically, this

complexation has large entropic contributions. The complexation between these oppositely charged supramolecular and covalent polymers frees counterions from each complexed polymer as well as associated water which increases the entropy of the system, thus driving the complexation. Scanning electron microscopy and confocal microscopy confirmed the lamellar structure of the gel and showed that our material was heterogeneous in terms of dimensions of the sheets as well as their random orientation relative to each other, which we hypothesize is a result of the chaotic manner in which the two solutions were mixed.

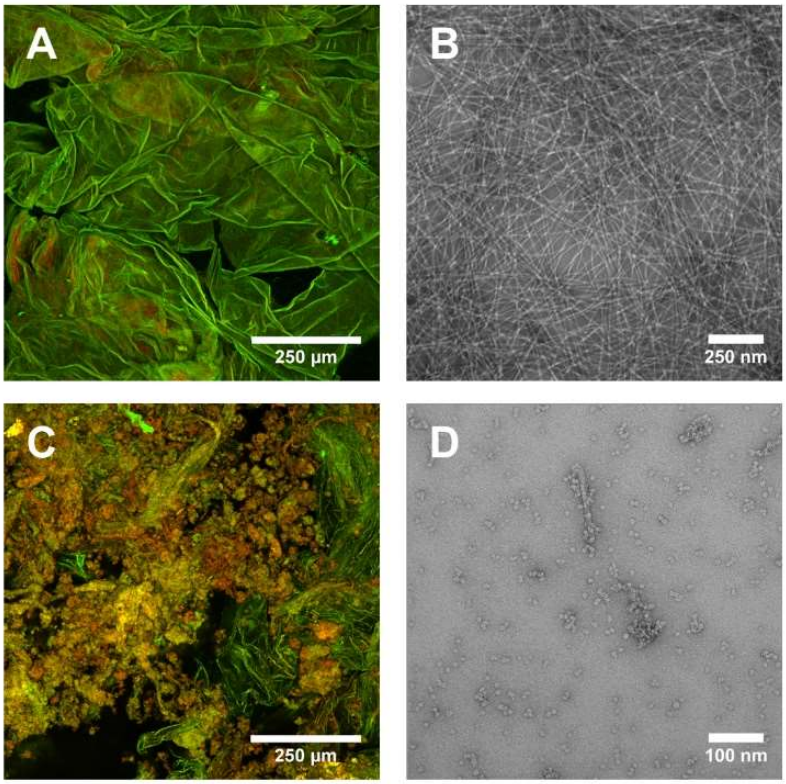

Figure 2.5: (A) Composite channel maximum intensity projection of confocal z-stack of PA-chitosan gel with the FITC-chitosan in green and the TAMRA-PA in red. Gel was prepared by mixing a 1 wt% solution of 10:1 chitosan/FITC-chitosan with an equal volume of a 2 wt% E3OH solution (pH 7) containing 0.1 mol% TAMRA-E3. (B) TEM image of PA nanofibers from an E3OH solution of pH 7. (C) Composite channel maximum intensity projection of confocal z-stack of PA-chitosan precipitates with the FITC-chitosan in green and the TAMRA-PA in red. Precipitates were created by mixing a 1 wt% solution of 10:1 chitosan/FITC-chitosan with an equal volume of a 2 wt% E3OH solution (pH 10) containing 0.1 mol% TAMRA-E3. (D) TEM image of PA micelles and nanofibers from an E3OH solution of pH 10.

The ability of the mixed components to form gels was found to greatly depend on pH of the PA solutions as well as their concentration. Gel formation required fibrous PA solutions at neutral a pH, but PA solutions at high pH, which contain predominantly spherical micelles due to electrostatic repulsive interactions among PA molecules,[176–178] lead to the formation of precipitates during complexation with chitosan (Figure 2.5). This result demonstrates the importance of the PA nanofiber morphology in the development of gels with fibrous sheet-like morphology. This agrees well with previous work that found that spherical assemblies of PAs did not result in formation of a noticeable diffusion barrier or nanofiber growth when exposed to oppositely charged polyelectrolytes.[179] These findings demonstrate the importance of the formation of a robust contact layer at the interface of the PA and covalent polymer solutions that locks in the sheet-like morphology. These contact layers provide structural robustness as well as prevent further mixing from taking place.

We also found that a sufficiently high PA concentration was required for gel formation. When the concentration of PA in solution was below 0.75 wt%, gel microparticles were obtained rather than a percolating network. This is likely because at lower PA concentration viscosity decreases and the striations become thinner and weaker, thus leading to tearing into these gel microparticles during rapid mixing. Because the sheets are smaller due to tearing, they were unable to make a cohesive network. On the other hand, at higher PA concentrations, we consistently observed sheet-like structures, and the formation of small particles was not observed (Figure 2.6). It was also found that the ratio of the polymer solution to the PA solution affects the mechanical properties of the gel. As shown in Figure 2.7A, increasing the volume ratio of polymer solution used results in increased modulus and strain at break. A gel formed from a mixture of 1.5 wt% PA

solution and 1 wt% chitosan solution in a 1:1 volume ratio has a storage modulus in the linear viscoelastic region that is approximately 2.4 times higher than a 3:1 mixing ratio and 4.8 times higher than a 5:1 mixing ratio. This is consistent with previous work that found that increasing the amount of polymer increased the modulus of planar PA-polymer membranes.[62]

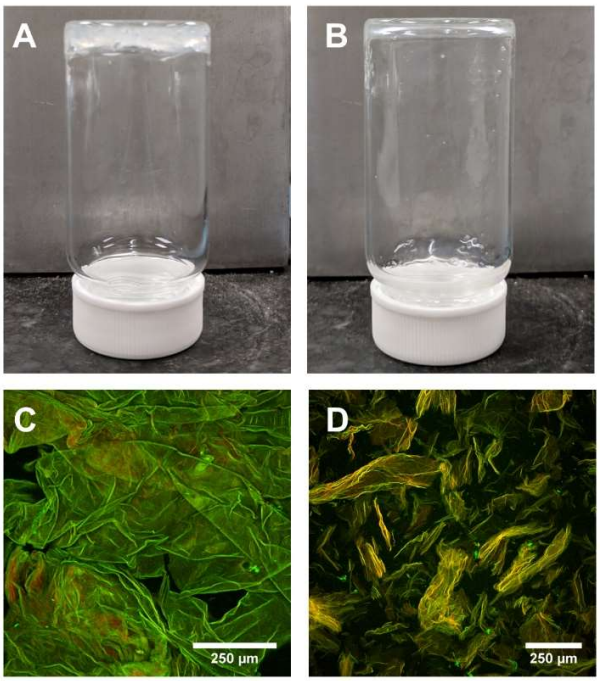

Figure 2.6: (A) image of a gel undergoing a tilt test, gel was prepared by mixing a 1 wt% solution of chitosan with an equal volume of a 2 wt% E3OH solution (pH 7). (B) image of a sample undergoing a tilt test with the samples contents, gel particles, sliding down the vial, the gel particles were prepared by mixing a 1 wt% solution of chitosan with an equal volume of a 0.5 wt% E3OH solution (pH 7). (C) Composite channel maximum intensity projection of confocal z-stack of PA-chitosan gel with the FITC-chitosan in green and the TAMRA-PA in red. Gel was prepared by mixing a 1 wt% solution of 10:1 chitosan/FITC-chitosan with an equal volume of a 2 wt% E3OH solution (pH 7) containing 0.1 mol% TAMRA-E3. (D) Composite channel maximum intensity projection of confocal z-stack of PA-Chitosan gel particles with the FITC-Chitosan in green and the TAMRA-PA in red. Particles were created by mixing a 1 wt% solution of 10:1 Chitosan/FITC-Chitosan with an equal volume of a 0.5 wt% E3OH solution (pH 7) containing 0.1 mol% TAMRA-E3.

The mechanical properties of the hydrogels can also be tuned by varying the concentration of the PA solution while keeping the chitosan concentration constant. In these experiments, the

chitosan solution used was 1 wt%, and the E3OH solution used was either 1 wt%, 1.5 wt%, or 2 wt% with constant volume ratios of both solutions (Figure 2.7B). As the concentration of the PA solution increases from 1 wt% to 2 wt%, the storage moduli of the gels in the linear viscoelastic region decreases from approximately 10 kPa to 6 kPa, respectively. This was unexpected because gels typically show an increase in moduli with as the concentration of gelator increases. We hypothesize that this phenomenon is a result of how effective the mixing of the chitosan and PA solutions is as gelation takes place at the interfaces between both. Increasing the concentration of PA in solution from 1 wt% to 2 wt% increases the viscosity of the solution, with all of the PA solutions showing non-Newtonian shear thinning behavior and higher concentrations consistently showing a higher viscosity for a given shear rate (Figure 2.7C). This increase in viscosity lowers the amount of mixing that can occur before mixing is arrested by gelation at interfaces. Decreased mixing results in lower surface area, thus reducing interactions among sheets in the resultant gel. The shear moduli of the gels are highly dependent on the interactions between the surfaces of the sheets in the gels, so we assume that as proper mixing of the two solutions deteriorates, the moduli of gels decrease.

To explore this hypothesis, we determined the composition of the gels by quantifying the amount of FITC-labeled chitosan in fluid excluded from the gels using absorbance spectroscopy. Absorbance spectroscopy shows that as the concentration of PA increases, we observe higher amounts of chitosan in the excluded fluid, corresponding to less chitosan in the gel as well as a lower ratio of chitosan to PA in the gel (Figure 2.8). Increasing the amount of the negative component would not decrease the amount of the positive component that was complexed in a typical polyelectrolyte complex. However, in this system, as the mixing efficiency is decreased

due to increased viscosity, we expected to create lower moduli gels with less gelled interfacial area as suggested by rheometry and absorbance spectroscopy data.

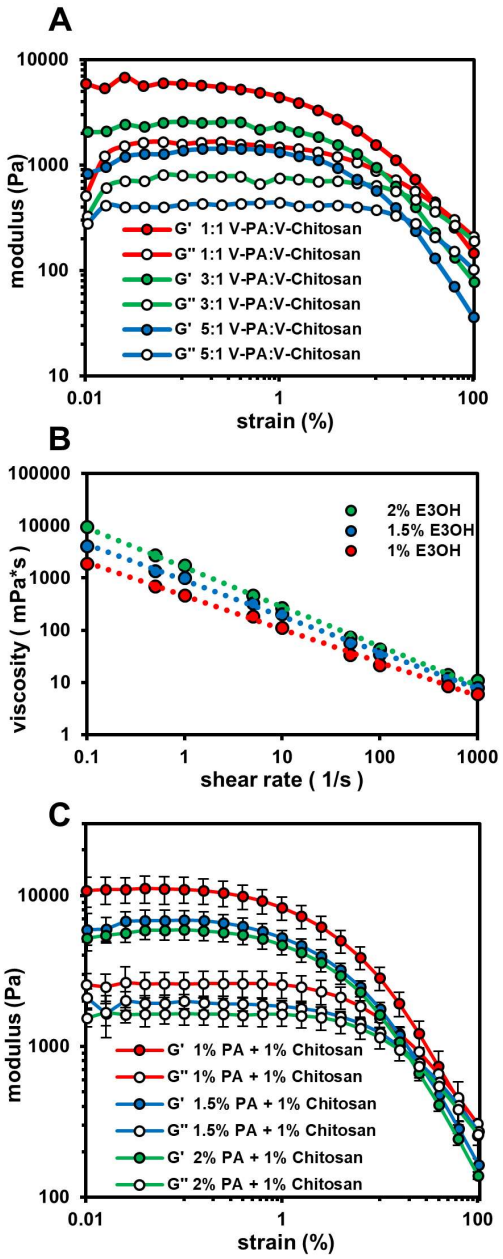

Figure 2.7: (A) Oscillatory rheology amplitude sweeps of gels made by mixing solutions of 1.5 wt% PA with a 1 wt% chitosan solution in varied volume ratios. (B) Oscillatory amplitude sweep of gels prepared by mixing 1 wt% chitosan solution with an equal volume of PA solutions of varying concentration. (C) Viscosity of PA solutions as a function of concentration with power law fits that all have negative slopes indicating shear thinning behavior in all PA samples.

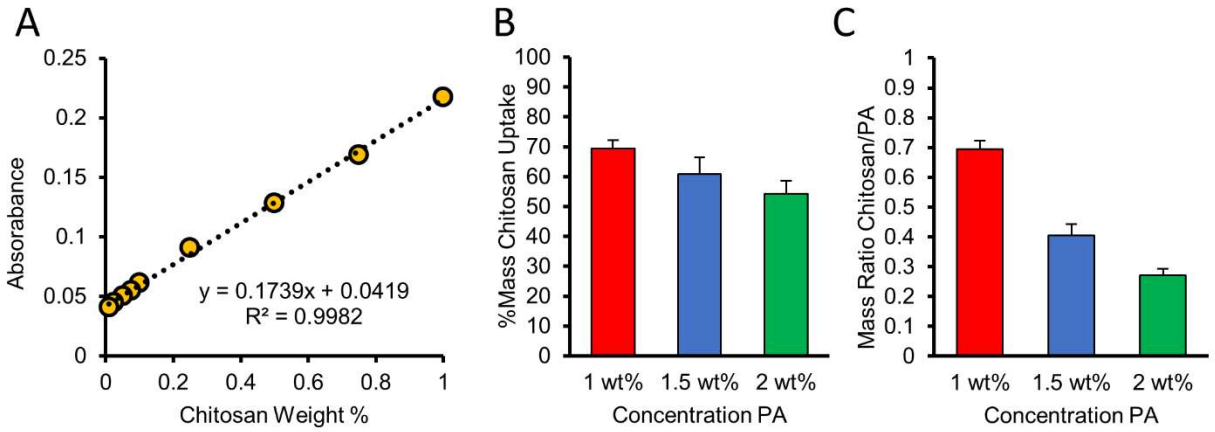

Figure 2.8: (A) Absorbance calibration curve of 10:1 chitosan/FITC-chitosan. (B) Mass percent of chitosan incorporated into gels during the gelation of PA solutions at various concentrations with a 1 wt% chitosan solution. (C) Mass ratio of chitosan to PA in gels prepared via the gelation of PA solutions at various concentrations with a 1 wt% chitosan solution.

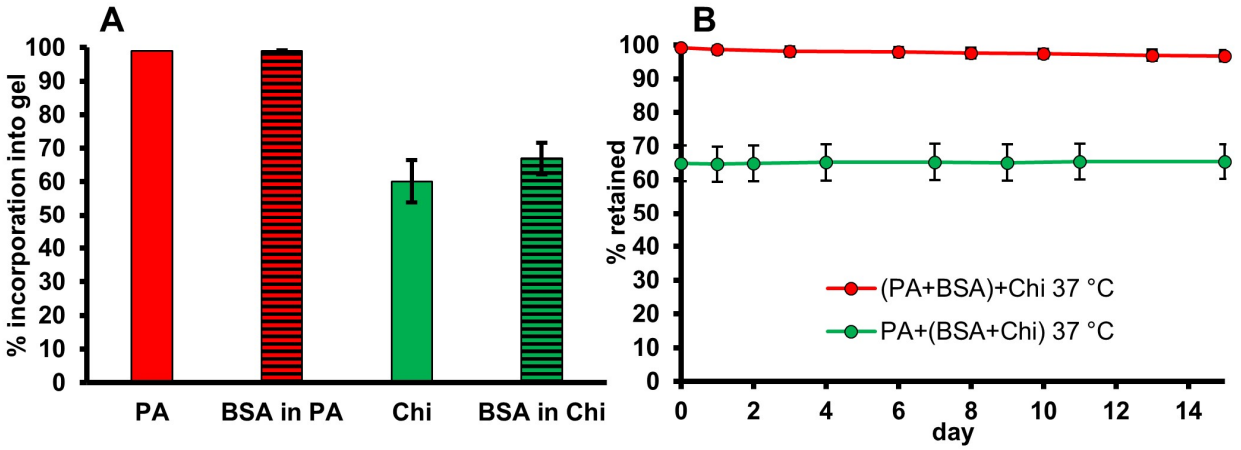

Figure 2.9: (A) Graph of the amount of PA and chitosan that are incorporated into hydrogel during gelation as well as the amount of BSA that is incorporated when it is dissolved in either PA solution or chitosan solution prior to mixing. (B) Plot of BSA retention in hydrogels when placed in a PBS bath at 37 °C (BSA was dissolved in either PA solution (red) or chitosan solution (green) prior to gelation).

Because the PA solution is effectively encapsulated by the contact layer, we hypothesized that this gel would offer a platform for protein encapsulation and delivery. We explored this possibility using bovine serum albumin (BSA) labeled with FITC so that the release and encapsulation could be monitored. We found that encapsulation depended on which solution the

protein was dissolved in prior to gel formation (Figure 2.8A). The initial encapsulation efficiency was found to be 99% when the FITC-BSA was dissolved in the PA solution prior to mixing. However, the initial encapsulation efficiency was found to be 67 ± 5% when the FITC-BSA was dissolved in the chitosan solution prior to mixing. The higher encapsulation that occurs when the protein is dissolved in the PA solution is likely a result of the PA solution itself being nearly entirely incorporated into the gel. In contrast, only 60 ± 6% of the chitosan is incorporated into the gel. Because a significant amount of the chitosan solution is not incorporated into the gel, it is not surprising that a corresponding amount of protein that was in the chitosan solution is also not incorporated into the gel.

In addition to measuring the encapsulation of the protein in E3OH-chitosan hydrogels, retention in the hydrogels was also measured (Figure 2.9B). For this experiment, protein loaded hydrogels were produced by dissolving FITC-BSA in either the PA solution or the chitosan solution prior to gel formation during mixing. Gels were washed and then placed in PBS solutions at 37 °C, and the absorbance of FITC-BSA in the supernatant PBS solution was monitored over time. The amount of protein retained in the gels produced with BSA dissolved in the chitosan solution starts off lower because a relatively lower amount of FITC-BSA is encapsulated in these gels. In the gels produced with FITC-BSA dissolved in the chitosan solution, there was no significant release detected over the course of 15 days, resulting in a 65 ± 5% retention. In gels produced with FITC-BSA dissolved in the PA solution prior to gel formation, after 15 days, 97 ± 0.5% of the protein was retained. While it is difficult to make a direct comparison, the retention of BSA in these gels appears to be higher than previously reported PA-polymer gels that do not have

a diffusion barrier.[169] We hypothesize that the slower protein release observed is due to the dense diffusion barrier at the polymer-PA interface.

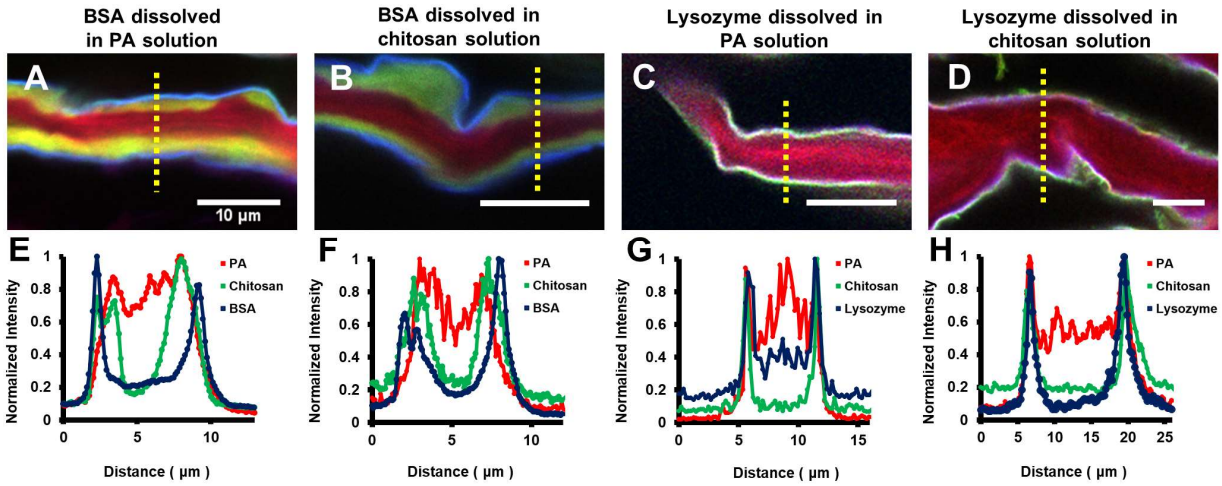

Figure 2.10: (A-D) Confocal micrographs of PA-chitosan gels containing either Alexa Fluor 647-labeled BSA or Alexa Fluor 647 labeled lysozyme (FITC chitosan in green, TAMRA-E3 in red, and BSA or lysozyme in blue) all scale bars 10 micrometers. (E-H) Plots of the normalized intensity values of each channel (FITC chitosan in green, TAMRA-E3 in red, and Alexa Fluor 647 lysozyme in blue) for the line cut (yellow dashed line) of the composite confocal image above each respective plot.

Confocal experiments were performed to determine where BSA was located in gels (Figure 2.10 A,B,E,F). For these experiments, protein loaded hydrogels were produced by dissolving Alexa Fluor647 labeled BSA in either the PA solution (Figure 2.10A and 2.10E) or the chitosan solution (Figure 2.10B and 2.10F) prior to gel formation during mixing. In both experiments the FITC-chitosan and TAMRA-E3 were used so that all gel components could be studied. As shown in Figure 2.10A and 2.10B, the Alexa Fluor 647 labeled BSA was found to have its highest concentration in the outermost region of the sheets, regardless of whether or not the BSA was dissolved in the PA solution or the chitosan solution prior to mixing. To better understand the role of electrostatics, we also explored encapsulation of the protein lysozyme which bears a net positive charge (isoelectric point ~11). Alexa Fluor 647 labeled lysozyme was also localized in the

outermost region of the gel, whether the protein was dissolved in the PA solution or the chitosan solution, as shown by the confocal microscopy (Figure 2.10C and 2.10D). The fluorescence intensity line cuts (Figure 2.10E-H) show high density of both chitosan and PA on the outermost region of the gel sheets as a result of their complexation. This dense region acts as a diffusion barrier that can trap proteins regardless of their charge. This area has both positively and negatively charged motifs that could interact with the negatively and positively charged domains on either protein that was encapsulated. Additional noncovalent interactions beyond electrostatics such as hydrogen bonding can occur between the protein and network. The density of the network in the contact region increases the density of potential noncovalent interactions that can take place between the network and proteins.

2.3 Conclusion

We have shown that mixing of a supramolecular polymer with a polyelectrolyte of opposite charge leads to rapid formation of a hydrogel containing crumpled sheets, and the complexation at the interfaces of the mixing solutions leads to nonequilibrium structures with distinct domains. Interestingly, decreasing concentrations of the supramolecular polymer were found to lower the solution viscosity, allowing greater complexation during mixing, resulting in gels with higher shear moduli. The hydrogels have tunable rheological properties and the ability to encapsulate and retain proteins. The formation of a dense contact layer at the interface of the supramolecular polymer and polyelectrolyte during gelation localizes both positively and negatively charged proteins in the outermost layer of the gel. These gels, with their tunable mechanical properties and the ability to encapsulate proteins, could be useful biomaterials for protein delivery in regenerative medicine and wound healing.

2.4 Materials and Methods

Peptide amphiphile synthesis: The peptide amphiphiles (PAs) C16-VVVAAAEEE-COOH (E3OH) and C16-VVVAAAEEE-K(TAMRA)-CONH2 were synthesized via standard 9-fluorenyl methoxycarbonyl (Fmoc) solid-phase peptide chemistry on pre-loaded glutamic acid Fmoc-Glu-Wang resin and Rink amide MBHA resin respectively using a CEM Liberty Blue automated microwave peptide synthesizer. Automated coupling reactions were performed using 4 equiv. Fmoc-protected amino acid, 4 equiv. *N*,*N'*-diisopropylcarbodiimide, and 8 equiv. ethyl(hydroxyimino)cyanoacetate (Oxyma pure). Removal of the Fmoc groups was achieved with 20% 4-methylpiperidine in DMF. Peptides were cleaved from the resin using standard solutions of 95% TFA, 2.5% water, 2.5% triisopropylsilane for 3 h, precipitated with cold ether, and then purified by reverse-phase HPLC on a Waters Prep150 or Shimadzu Prominence HPLC using a water/acetonitrile (each containing 0.1% NH_4OH v/v) gradient. Eluting fractions containing the desired peptide were confirmed by mass spectrometry using an Agilent 6520 QTOF LCMS. Confirmed fractions were pooled and the acetonitrile was removed by rotary evaporation before freezing and lyophilization. Purity of lyophilized products was tested by LCMS.

For 5-carboxytetramethyrhodamine (TAMRA) labeled PA, the methyltrityl (Mtt) protecting group was removed from the lysine after automated synthesis while still on resin using 3% TFA in DCM with 5% triisopropylsilane. After washing with DCM and DMF, TAMRA was then coupled to the now free epsilon amine of lysine using 1.2 equiv. carboxy-TAMRA, 1.2 equiv. PyBOP (benzotriazol-1-yl-oxytripyrrolidinophosphonium hexafluorophosphate), and 8 equiv. *N*,*N*-diisopropylethylamine (DIEA) for approximately 18 h.

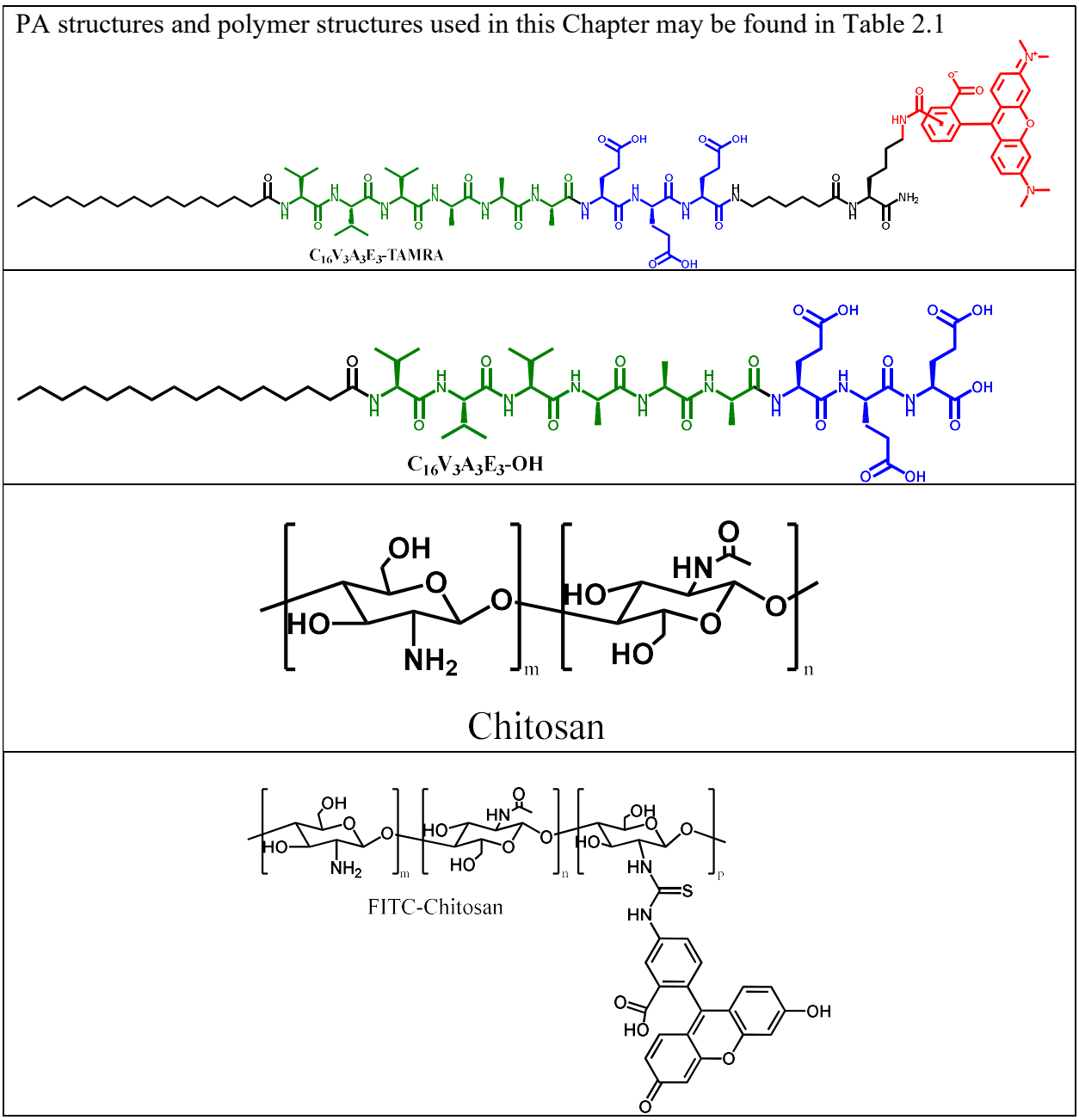

Table 1.1: Chemical structures of E3OH, TAMRA-E3, chitosan, and FITC-chitosan

E3OH solutions: E3OH solutions were prepared by adding deionized water to the PA and adjusting pH using 1 M NaOH. Unless otherwise specified, PA solutions were adjusted to pH 7 and sonicated

until all PA was dissolved. Solutions were placed in a water bath at 80 °C for 30 minutes, and then slowly cooled to room temperature.

TAMRA-E3/E3OH co-assemblies: TAMRA-E3 co-assembled with E3OH were prepared by mixing a solution of TAMRA-E3 at 0.1 wt% in deionized water with a solution of E3OH such that the final concentration of the TAMRA-E3 relative to E3OH was either 0.1 mol% or 1 mol% depending on how much dye was desired for imaging. The TAMRA-E3 co E3OH mixtures were then sonicated to ensure dissolution and mixing. Solutions were placed in a water bath at 80 °C for 30 minutes and then slowly cooled to room temperature.

Chitosan: Medium molecular weight chitosan (190,000-310,000 Da) was purchased from Sigma-Aldrich (#448877). The chitosan was dissolved in 2 vol% acetic acid, the remaining solid was filtered off, and the solution dialyzed in 12-14 kDa molecular weight cutoff Spectra/Por tubing against deionized water and then freeze dried.

Chitosan solutions: Chitosan solutions were prepared by dissolving filtered and lyophilized chitosan at 2 wt% in 2 vol% acetic acid. After the chitosan was dissolved, it was diluted to 1 wt% chitosan with a 500 mM sodium acetate solution.

FITC-labeled Chitosan: Filtered and lyophilized chitosan was dissolved in 2 vol% acetic acid, and the solution diluted to 1 wt% using methanol. While the chitosan solution was stirred, a 2 mg/mL fluorescein isothiocyanate (FITC) methanol solution was added to a final volume ratio of chitosan to FITC solution of 2:1. After stirring for 4 hours the chitosan was precipitated by adding 1 M NaOH solution, and the precipitate was washed with aqueous 30% methanol solution. The precipitate was collected using vacuum filtration and redissolved in 1 vol% acetic acid. This

solution was dialyzed in Spectra/Por 12-14 kDa molecular weight cutoff tubing against deionized water and then freeze dried.

FITC-Chitosan solutions: 2 wt% aqueous FITC-chitosan solutions (filtered and lyophilized) were prepared in 2 vol% acetic acid. Solutions were diluted to 1 wt% chitosan with a 500 mM sodium acetate solution, and they could be mixed with a 1 wt% chitosan solution in order to vary the amount of FITC.

Alexa Fluor 647-Labeled Lysozyme: 20 mg of lysozyme from chicken egg white was obtained from Sigma Aldrich and dissolved in 0.1 M sodium bicarbonate to achieve a lysozyme concentration of 10 mg/mL. Alexa Fluor 647 carboxylic acid succinimidyl ester (1 mg) was dissolved in 100 μL of dimethylformamide and added to the stirring lysozyme solution at room temperature. After reacting for 1 hour while stirring, the reaction was quenched by adding 200 μL of 1 M hydroxylamine in water (pH 8) and stirred for 1 additional hour. The Alexa Fluor 647-labeled lysozyme was purified by dialyzing for 48 hours in deionized water using Spectra/Por 3.5 kDa molecular weight cutoff tubing and then freeze dried and stored at -20 °C.

Gelation: Unless otherwise noted, equal volumes of PA and chitosan solutions were injected into opposite sides of a 20 mL scintillation vial. The solutions were then immediately vortex mixed together for ten seconds on the highest mixing setting of a Scientific Industries Vortex Genie.

Scanning Electron Microscopy: Gels were placed into microporous specimen capsules (Electron Microscopy Sciences) and solvent exchanged into absolute ethanol by placing the capsule into 30%, 40%, 50%, 60%, 70%, 80%, 90%, 95% ethanol-water solutions for 10 minutes, followed by 15 minutes in a 100% ethanol solution. Following solvent exchange into absolute ethanol, the gel

was critical point dried in the specimen capsule using a Tousimis Samdri-795 Critical Point Dryer. The dry gel was then coated with 10 nm of osmium using a Filgen Osmium Plasma Coater OPC60A, and micrographs were taken using a Hitachi S-4800 scanning electron microscope.

Solution Rheology: Viscosity measurements were performed using an Anton Paar MCR 302 Rheometer. The CP50-1 fixture (50 mm cone with 1° angle) was used to measure viscosity of 600 μL solutions (25 °C). Mean viscosities were calculated at each shear rate by averaging the measured viscosities in a 100 second interval after the experiment reached steady state.

Rheology of E3OH-Chitosan Gels: Measurements were performed using an Anton Paar MCR 302 Rheometer. The PP20 fixture (20 mm plate) was used with a normal force gap setting of 0.1 N and a temperature of 25 °C. Gels were solvent exchanged in deionized water for 24 hours prior to testing to ensure that all gels remained at the same pH and ionic strength. Amplitude sweeps were performed using a logarithmic ramp from 0.01% strain to 100% strain with constant frequency of 10 rad/s.

X-ray Scattering: X-ray scattering experiments were performed at Beamline 5-ID-D, DND-CAT, Advanced Photon Source at the Argonne National Laboratory. An X-ray energy of 17 keV was selected using a double monochromator, and the scattering patterns for an empty cell, water-filled cell and sample-filled cell were recorded using a set of three charge coupled device (CCD) detectors.[180] The hydrogel samples were sealed in Grace Bio-Labs silicone isolators with Chemplex 7.5 μm Kapton windows and placed in the beam. The solution samples were placed in a vacuum flow cell comprising of a 1.5 mm quartz capillary connected to a syringe pump. The two-dimensional scattering patterns then azimuthally integrated to generate a scattering vector

magnitude q vs. intensity plot, where q is defined as $q=4\pi\sin(\theta)/\lambda$ for which θ denotes the half of total scattering angle and λ the X-ray wavelength, 0.7293 Å. 2D to 1D data reduction was performed by GSAS-II software.[181] We did not attempt to determine the absolute scattering intensity.

Confocal Microscopy: Gels were placed on a glass slide with an adhesive spacer that was then covered with cover glass. Imaging was performed on the Leica SP5 Confocal Microscope and the Nikon A1R Confocal Microscope. On the Leica SP5 Confocal Microscope, the 488 nm laser line was used to image the FITC-Chitosan and the 543 nm laser line to image the TAMRA-E3. On the Nikon A1R Confocal Microscope, the 488 nm laser line was used to image the FITC-Chitosan and the 561 nm laser line to image the TAMRA-E3, and the 640 nm laser line to image the Alexa Fluor 647-labeled BSA and Alexa Fluor 647-labeled lysozyme.

Negative stain TEM: E3OH samples were prepared at 2 wt% with one of the samples having 1.1x molar equivalents of NaOH to E3OH added to achieve pH 7, and the other sample having 3.3x molar equivalents of NaOH to E3OH added to achieve pH 10. Samples were diluted to ~1 mM concentration with water immediately prior to sample preparation. Carbon coated TEM grids (CF300-Cu-UL, Electron Microscopy Sciences) were glow discharged using a PELCO Easi-Glow instrument with 15 mA current for 30 s. 5 μL of diluted sample was applied on a grid and the excess solution wicked with a filter paper after 30s. 5 μL of 1 wt% uranyl acetate solution, filtered with a 200 nm PTFE syringe filter before use, was applied on the grid. After 10 s, the excess staining solution was wicked with a filter paper, and the sample was allowed to dry. TEM images were obtained using a JEOL ARM300F microscope operated at 300 kV acceleration voltage. The

images were recorded with a Gatan OneView IS detector in imaging mode, with real-time drift correction.

Formation of Gels Containing Protein for Confocal Microscopy: Gels were prepared by dissolving either Alexa Fluor 647-labeled BSA from Invitrogen or Alexa Fluor 647-labeled lysozyme in either the PA solution or the chitosan solution. For gels with protein in the PA solution, the protein was dissolved at 1 mg/mL in a pre-annealed TAMRA-E3 co-assembled with E3OH (1.5 wt% solution). The TAMRA-E3 was 0.1 mol% relative to the total amount of PA in solution. The protein loaded PA solution was injected at the same time as a 10:1 chitosan to FITC chitosan solution by weight in opposite sides of the vial, and solutions were immediately vortex mixed for 10 seconds. For gels with protein in the chitosan solution, the protein was dissolved at 1 mg/mL in a 10:1 chitosan to FITC chitosan solution. The protein loaded chitosan solution was injected at the same time as a pre-annealed TAMRA-E3 co-assembled with E3OH (1.5 wt% solution). The TAMRA-E3 was 0.1 mol% relative to the total amount of PA in solution. The gels were placed in Electron Microscopy Sciences microporous specimen capsules and solvent exchanged with deionized water.

Quantification of chitosan in excluded fluid: A 10:1 chitosan to FITC-chitosan solution by weight was prepared by mixing 1 wt% chitosan solution with 1 wt% FITC-chitosan solution. A calibration curve was obtained by diluting the 10:1 chitosan to FITC-chitosan solution with deionized water. The absorbance of three 100 μL solutions at each concentration were measured at 490 nm using a Cytation 3 plate reader, and the measured values were then averaged for each concentration. Gels were prepared by vortex mixing the 1 wt% 10:1 chitosan to FITC-chitosan solution with equal volumes of 1, 1.5, and 2 wt% E3OH solutions for 10 s. The excluded fluid was collected, and the

volumes were recorded. The solutions were then centrifuged, and the absorbance of 100 μL of the supernatant was measured at 490 nm using the Cytation 3 plate reader, and the calibration curve was used to calculate the concentration of the chitosan in solution.

Quantification of protein encapsulation: A stock solution of 0.45 wt% chitosan solution was prepared by diluting 1 wt% chitosan with deionized water, and FITC labeled BSA was dissolved in the 0.45 wt% solution at 1 mg/mL. A calibration curve was obtained by diluting the 1 mg/mL FITC-BSA solution with a 0.45 wt% chitosan solution. The fluorescence intensity of three 100 μL solutions at each concentration was measured with excitation at 490 nm and emission at 520 nm using a Cytation 3 plate reader. The absorbance of 100 μL solutions at 1, 0.75, 0.5, 0.25, 0.1, 0.075, and 0.05 mg/mL was measured at 490 nm using a Cytation 3 plate reader, and the measured values were then averaged over three samples for each concentration. Protein loaded gels were prepared by dissolving FITC-BSA at 1 mg/mL in either a pre-annealed 1.5 wt% E3OH solution or a 1 wt% chitosan solution. Gels with FITC-BSA in the PA solution were then prepared by vortex mixing a 1 wt% chitosan solution with equal volumes of the FITC-BSA E3OH solutions for ten seconds. Gels with FITC-BSA in the chitosan solution were prepared by vortex mixing the FITC-BSA chitosan solution with equal volumes of the 1.5wt% E3OH solutions for ten seconds. The excluded fluid was collected, and the volumes were recorded. The solutions were then centrifuged, and the fluorescence intensity of 100 μL of the supernatant was measured with an excitation at 490 nm and an emission at 520 nm using a Cytation 3 plate reader. The calibration curve was used to calculate the concentration of the FITC-BSA in solution. For gels prepared with the FITC-BSA in the chitosan solution, the fluorescence intensity of the excluded fluid was too high to reliably

quantify the concentration using fluorescence, so absorbance was used instead. The concentration of FITC-BSA in solution was used to calculate the remaining amount of FITC-BSA in the gel.

Quantification of protein release: FITC-labeled BSA was dissolved at 1 mg/mL in a phosphate buffered saline solution. A calibration curve was obtained by diluting the 1 mg/mL FITC-BSA solution with PBS. The absorbance of three 100 μL solutions at each concentration was measured at 490 nm using a Cytation 3 plate reader. Protein loaded gels were prepared by dissolving FITC-BSA at 1 mg/mL in either a pre-annealed 1.5 wt% E3OH solution or a 1 wt% chitosan solution. Gels with FITC-BSA in the PA solution were prepared by vortex mixing a 1 wt% chitosan solution with equal volumes of the FITC-BSA E3OH solutions for ten seconds. Gels with FITC-BSA in the chitosan solution were prepared by vortex mixing the FITC-BSA chitosan solution with equal volumes of the 1.5 wt% E3OH solutions for ten seconds. Gels were collected and washed for 24 hours in a PBS solution to remove excess chitosan and salt. Gels were placed in PBS and a portion of the supernatant was removed, centrifuged, and the absorbance spectra of 100 μL of the centrifuged supernatant was measured using a Cytation 3 plate reader (Rayleigh background scattering was subtracted so that remaining gel fragments did not affect release analysis). The calibration curve was used to calculate the concentration of the FITC-BSA in solution by comparing sample values at their absorbance values at 490 nm. After measuring absorbance, the supernatant that was removed was put back into the respective samples, and this measurement protocol was used at each time point (N=4 samples were used for each sample condition, samples were held at 37 °C).

CHAPTER 3: Extracellular Matrix Mimetic Scaffolds by Microfluidic Superstructuring of Nanofibers

3.1 Background

The extracellular matrix (ECM) is a masterwork of biology that provides mechanical support and biological signals according to each tissue's specific needs.[182–185] In addition to supporting and directing the growth of the cells that reside within, it adapts to external and internal forces by modulating its microstructure and chemistry.[186] Although many different biomaterials have been suggested as mimics for ECM,[186] supramolecular nanomaterials show exceptional promise due to their chemical flexibility and biodegradability.[187–192]

Peptide amphiphiles (PAs) are a well-established class of supramolecular biomaterials composed of self-assembling amphiphile monomers.[193,194] Each amphiphilic monomer is composed of a hydrophobic tail covalently bonded to a peptide head. The Stupp Laboratory has developed a class of PAs which utilize β-sheet forming peptide regions to promote aqueous assembly of 1-dimensional nanostructures with an inner aliphatic core and an outer peptide shell.[5,19] These nanofibers provide structural and chemical cues similar to natural ECM.[4,186,195,196] Arranging these nanoscopic structures into microscopic and macroscopic constructs that resemble ECM superstructure is an ongoing challenge, though significant strides towards macrostructural control have been made.[57,197] The most common approach to PA gelation is bulk gelation, in which a static solution of PA fibers is exposed to a gelator. This creates a hydrogel which has nanoscopic anisotropy yet is microscopically disordered.[198] Manually extruded PA was the first reported example of aligned monodomain PA materials.[58] Shear forces applied during extrusion through a

pipet tip, combined with manually applied tensile stress, yield hydrogels which are millimeters in diameter and centimeters in length. This method retains the nanoscopic structure of PA nanofibers while adding microscopic alignment from the applied shear and tensile forces.

Microfluidic flow focusing, a family of techniques in which multiple fluid streams are combined at a junction during laminar flow,[78,99,101,199] stands as an automated alternative to hand-extrusion of PAs[58] and addresses a smaller length scale than 3D printing.[197] In flow-focusing microfluidic devices, a stable, continuous interface can form depending on the junction geometry and the nature of the fluids' interactions.[115] These fluid interactions can include surface tension,[199,200] interfacial diffusion,[124] and chemical reactions.[101] We hypothesized that we could utilize the interaction of PAs with inorganic multivalent ions to form gels within a flow focusing microfluidic device. In this paper, we employed microfluidic flow focusing to extrude PAs into microscale superstructures we have termed superbundles (SBs). Specifically, we define superbundles as discrete, hyper-aligned, high aspect ratio superstructures with microscale widths consisting of many PA nanofibers. Herein, we formulate design rules for creating SBs and investigate their morphological resemblance to decellularized extracellular matrix (dECM) as well as their ability to encapsulate proteins.

3.2 Results and Discussion

In designing a microfluidic device to achieve our goal of aligned, micron-scale PA superbundles, we were guided by two key principles. First, PAs are carefully designed to form nanostructures, and previous work has demonstrated that forcing solutions of PA nanofibers through an aperture will order the constituent nanofibers into a monodomain with alignment parallel to the flow direction.[58] Second, PAs can be locked into a specific shape using gelators –

substances that interact with the chemistries of adjacent PA nanofibers to cause gelation. The device we designed to extrude PA superbundles consists of a single-layer, planar device containing a junction which encapsulates a central PA flow within a sheathing gelator flow (Figures 3.1). Briefly, a solution of ungelled PA nanofibers enters a four-way junction with three inlets and one outlet. The PA inlet is located opposite the outlet, and the two channels perpendicular to the PA inlet carry gelator into the junction, impinging on the central PA flow. The three entrances to the junction have identical rectangular cross sections. The exit channel has a reduced rectangular cross section which acts as a flow constrictor (Figures 3.1b and 3.1c). This promotes additional flow focusing within the junction by forcing a higher flow velocity within the constrictor. Following the constrictor, the outlet channel expands and leads to a collection bath. Within the device channels, laminar flows at low Reynolds numbers are used. The Reynolds number (Re) helps to determine flow patterns and the transition from laminar (low Reynolds number) to turbulent (high Reynolds number) flows. The relationship is broadly defined as the ratio of inertial to viscous forces in a fluid and while many forms of the relationship exist, a general form incorporates the flow speed, u, a characteristic linear dimension, L, and the kinematic viscosity, ν.

$$Re = \frac{uL}{\nu}$$

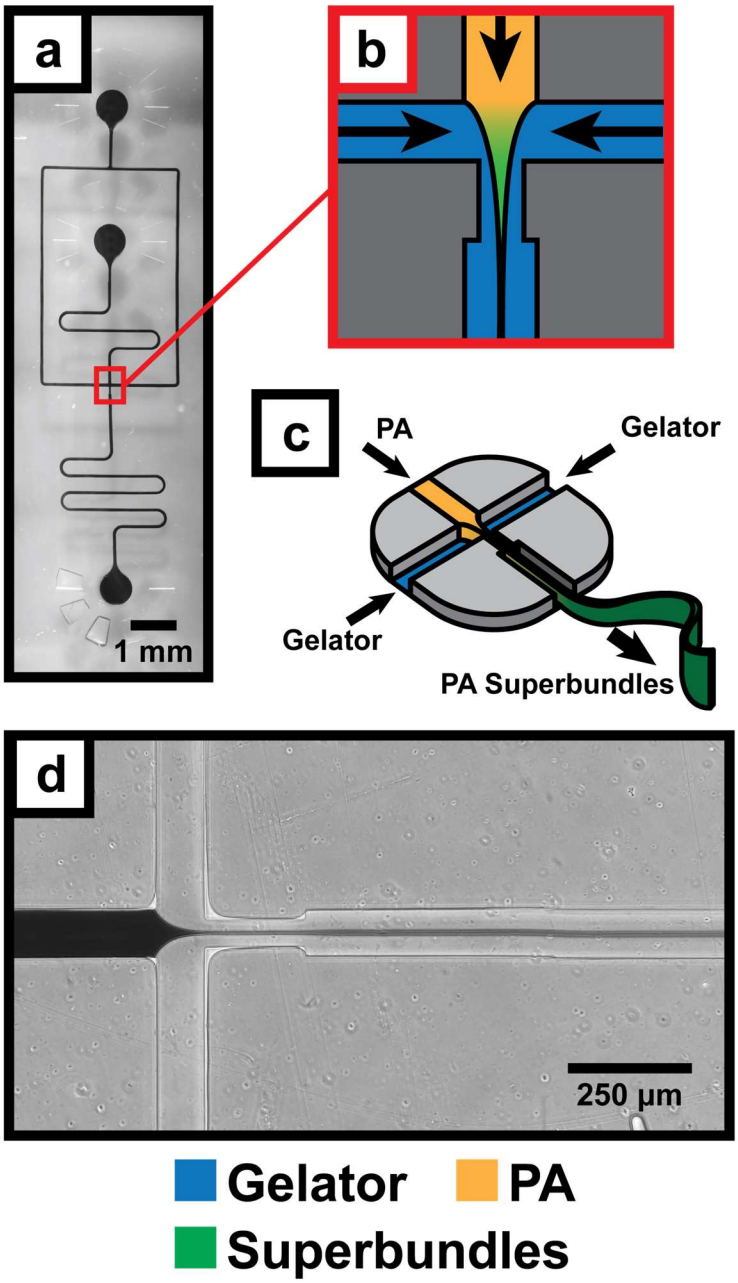

Figure 3.1: (a) Composite photograph of the microfluidic device used to produce superbundles, enhanced for clarity. (b) 2-dimensional projection of the 4-way junction where SBs (green) are formed from the interaction between a gelator (blue) and annealed PA (gold). (c) 3-dimensional schematic of the 4-way junction where the inner PA solution (gold) is impinged by gelator solution (blue), producing superbundles (green). (d) Photograph of the flow focusing effect at the microfluidic junction, dye used for visualization of flow profile.

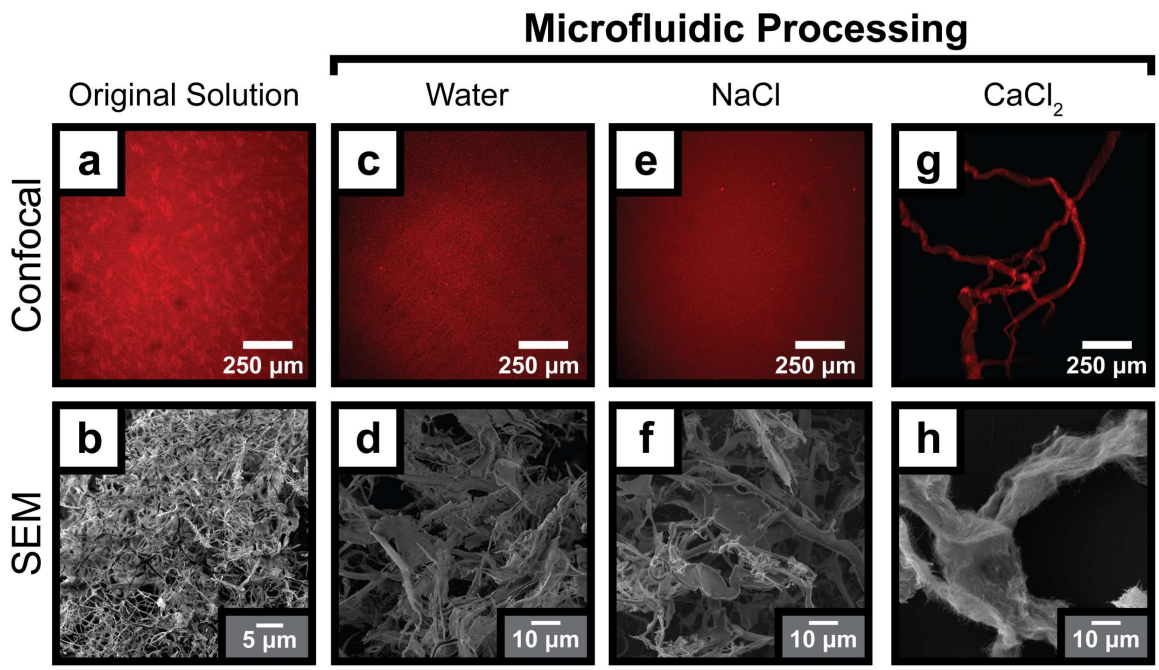

Figure 3.2: (a) Confocal laser scanning microscopy (confocal) of E3 solution as annealed. (b) Scanning electron microscopy (SEM) of E3 solution as annealed. (c) Confocal of E3 solution after being extruded from the microfluidic device using deionized water as the sheathing solution. (d) SEM of E3 solution after being extruded from the microfluidic device using deionized water as the sheathing solution. (e) Confocal of E3 solution after being extruded from the microfluidic device using aqueous 150 mM sodium chloride as the sheathing solution. (f) SEM of E3 solution after being extruded from the microfluidic device using aqueous 150 mM sodium chloride as the sheathing solution. (g) Confocal of E3 solution after being extruded from the microfluidic device using an aqueous solution that contains 25 mM calcium chloride, 3 mM potassium, and 150 mM sodium chloride. (h) SEM of E3 solution after being extruded from the microfluidic device using an aqueous solution that contains 25 mM calcium chloride, 3 mM potassium, and 150 mM sodium chloride. 0.5 wt% E3 and FRR 10 was used for all extrusions.

To investigate the importance of multivalent ions in the formation of superbundles, we evaluated the ability of different sheathing solutions to gel C16-VVVAAAEEE PA (E3) into superbundles. These experiments were carried out with a 10-fold higher flow rate of sheathing solution flow than E3 solution to ensure adequate flow-focusing of the central PA flow. The relative flow rates, sheath volumetric flow rate ($\dot{f}_{Shea}$) and core volumetric flow rate ($\dot{f}_{Core}$) are described using the flow rate ratio (FRR).

$$\text{FRR} = \dot{f}_{Sheat} \ / \dot{f}_{Core}$$

Confocal microscopy of an annealed solution of PA nanofibers reveals a textured flat field (Figure 3.2a) and scanning electron microscopy (SEM) displays fibrous morphology (Figure 3.2b). When E3 was extruded through a microfluidic device with water as the sheathing solution, the extrudate produced a flat field in confocal (Figure 3.2c) and fibrous morphology in SEM (Figure 3.2d), indicating that no superbundles were formed and that the PAs were not gelled in the microfluidic device. When E3 PA was extruded with a sheathing solution of 150 mM sodium chloride, we once again observed a flat field in confocal microscopy (Figure 3.2e), indicating even distribution of PA in the extrudate solution, and fibrous structure in SEM (Figure 3.2f), indicating that there were no superbundles formed. This is because the monovalent ions such as Na^+ do not gel solutions of PA nanofibers, so this extrudate is a viscous liquid. Multivalent ions can gel solutions of PA nanofibers through non-covalent interfiber ionic bridging, and these ion bridges behave as interfiber crosslinks. When E3 was extruded with a solution of the counter-charged multivalent ion Ca^{2+}, superbundles were observed in confocal microscopy (Figure 3.2g) as well as SEM (Figure 2h). These results demonstrate that the formation of SBs during flow focusing relies on the presence of a gelator, such as multivalent ions, while solutions lacking multivalent ions, such as deionized water or monovalent ions, cannot.

There are many process and material parameters that can be tuned when forming gels by laminating flows at the four-way junction described previously. After meeting at the junction, the outer gelator solution forms a sheath flow around the core PA solution, and we hypothesized that the relationship between the flow rates of the sheath and core solutions would control the degree of confinement of the inner PA solution during gelation. Therefore, this flow rate ratio would be

crucial to the formation of superbundle structures. We held the total flow rate of PA plus gelator constant at 55 μL/min for these experiments and varied the FRR from a value of 17 (52 μL/min gelator; 3 μL/min PA) to 0.5 (18.3 μL/min gelator; 36.7 μL/min PA). In addition to the FRR, we also hypothesized that the concentration of PA present in the inner flow would affect the morphology of resultant gels. Total flow rate, Q_T, is defined as the sum of the volumetric gelator flow rate, $Q_{gelator}$, and the volumetric PA flow rate, Q_{PA}.

$$Q_T = Q_{gelator} + Q_{PA}$$

We explored a 2D parameter space of varied FRR and inner PA concentrations while holding other values, such as the concentration of the gelator, constant. We identified the production of superbundles using a blinded multipoint scale ranging from filamentous aggregates to superbundles. These experiments produced processing parameter diagrams (Figures 3.3a-c) which we used to identify processing conditions where superbundles could be reliably produced. Physiological cations, such as Ca^{2+}, have been used to gel PA nanofibers into free-standing gels.[50,59] We expected that aqueous calcium chloride would effectively gel E3 nanofibers into SBs. We observed that at high FRRs and PA concentrations, superbundles were produced (Figures 3.3d and 3.3e). At low FRRs, regardless of PA weight percent, we found filamentous aggregates – gels with nanoscopic, but not microscopic order. This non-superbundle morphology was observed with confocal and scanning electron microscopy (Figures 3.3f and 3.3g). This relationship between FRR and superbundle formation is likely due to the flow focusing effect - high FRRs more strongly confine inner PA flows. That high FRR is necessary for SB formation shows that the gelator solution must pinch in on the PA solution, confining it within the microfluidic channel. The high FRR is also important because due to the device geometry, the gelator flow stream must delaminate

the PA flow from all channel walls in order to encase the PA stream conformally. Expectedly, at very low PA concentrations (< 0.25 wt%), we found that superbundles could not be produced, even at high FRRs, because there was an insufficient amount of PA fibers in solution to form a stable percolating network.

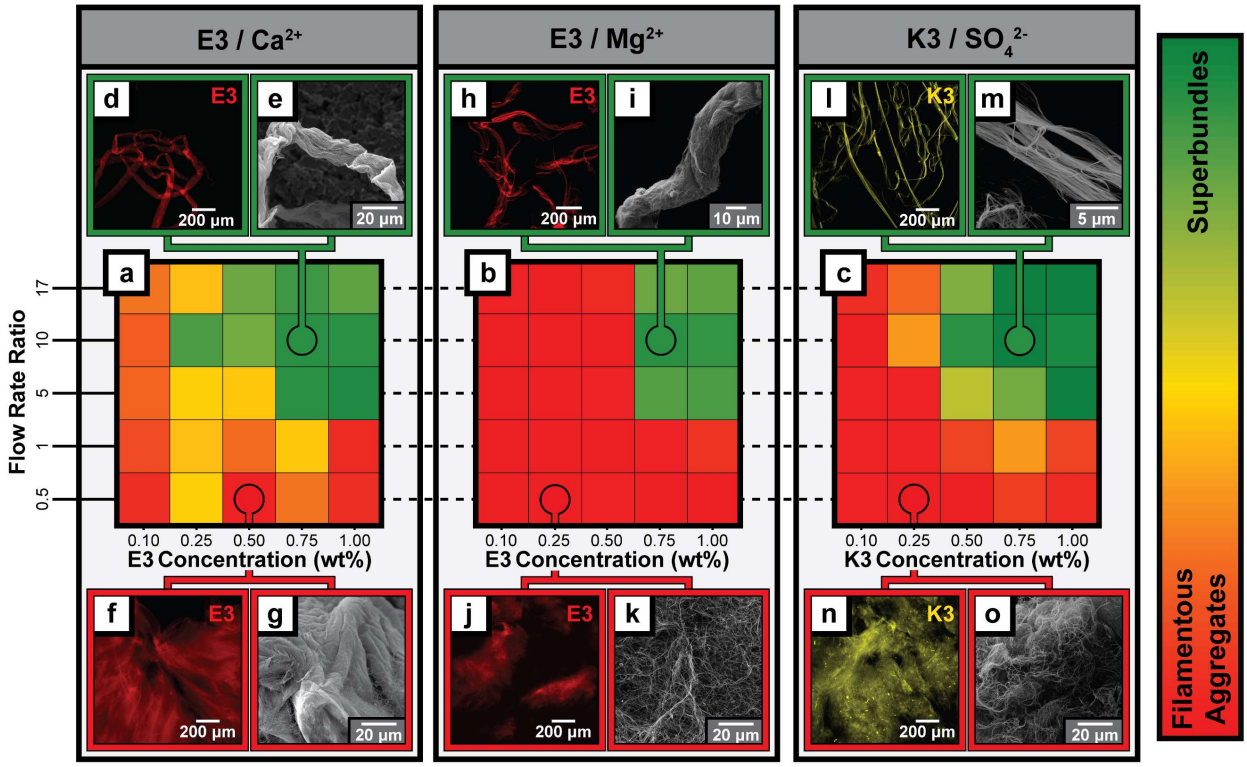

Figure 3.3: Processing parameter diagram (PPD) for (a) E3 solutions gelled with Ca^{2+} solutions at varied FRRs and E3 concentrations, (b) PPD for E3 solutions gelled with Mg^{2+} solutions at varied FRRs and E3 concentrations, and (c) PPD for K3 solutions gelled with SO_4^{2-} solutions at varied FRRs and K3 concentrations (green indicates SB formation, red indicates aggregate production).(d) Maximum intensity projection of confocal laser micrograph (MAX) of SBs produced with Ca^{2+} and 0.75 wt% E3 (red) at FRR 10. (e) SEM micrograph of an SB produced with Ca^{2+} and 0.75 wt% E3 at FRR 10. (f) MAX of a gel produced with Ca^{2+} and 0.5 wt% E3 (red) at FRR 0.5. (g) SEM micrograph of a gel produced with Ca^{2+} and 0.5 wt% E3 at FRR 0.5.(h) MAX of SBs produced with Mg^{2+} and 0.75 wt% E3 (red) at FRR 10. (i) SEM micrograph of an SB produced with Mg^{2+} and 0.75 wt% E3 at FRR 10. (j) MAX of a gel produced with Mg^{2+} and 0.25 wt% E3 (red) at FRR 0.5. (k) SEM micrograph of a gel produced with Mg^{2+} and 0.25 wt% E3 at FRR 0.5.(l) MAX of SBs produced with SO_4^{2-} and 0.75 wt% K3 (yellow) at FRR 10. (m) SEM micrograph of an SB produced with SO_4^{2-} and 0.75 wt% K3 at FRR 10. (n) MAX of a gel produced with SO_4^{2-} and 0.25 wt% K3 (yellow) at FRR 0.5. (o) SEM micrograph of a gel produced with SO_4^{2-} and 0.25 wt% K3 at FRR 0.5.

After successfully producing SBs with Ca^{2+} gelation, we sought to expand our library of gelator-PA pairs. We believed that the divalent gelation observed with Ca^{2+} would extend to other divalent cations, specifically Mg^{2+}. As shown in figure 3.3b, the processing conditions that produced superbundles in an E3/Mg^{2+} system resembled those identified in the E3/Ca^{2+} case (Figure 3.3a), specifically, high PA concentrations and FRRs led to SB formation as seen in confocal and SEM (Figures 3h and 3i), while low PA concentrations and FRRs did not produce SBs (Figures 3.3j and 3.3k). Interestingly, when using Mg^{2+} as the gelator, higher concentrations of PA nanofibers were required to form superbundles. This is because Mg^{2+} gelation of PAs generally makes weaker gels,[59] likely due to its significantly smaller ionic radius compared to Ca^{2+}, so higher concentrations of PA are needed to compensate. To demonstrate that microfluidic extrusion can create superbundles under more diverse conditions, we continued our investigations by using an oppositely charged system, where the PA material was positively charged and the gelling ion was negatively charged. To accomplish this, we utilized C16-VVVAAAKKK (K3) PA, and SO_4^{2-}. As shown in figure 3c, the same pattern of high-flow rate ratios and high PA concentrations produced SBs as seen in confocal and SEM (Figures 3.3l and 3.3m), while low PA concentrations and FRRs did not produce SBs (Figures 3.3n and 3.3o). We believe these findings demonstrate that microfluidic PA gelation can be extended to many use cases with different PA/gelator formulations. All the gelators produced micron-scale superbundles, and polarized optical microscopy confirmed that the SBs created with each gelator type were anisotropic, with each individual SB's network aligned in the extrusion direction because PAs align during flow (Figure 3.4). Using the processing parameter diagrams, we developed general processing and material design rules for producing superbundles using any gelator system. Specifically, SB

production was most reliable at FRRs above 5 and PA concentrations 0.1 wt% or greater (0.75 wt% in the case of Mg^{2+} gelator). We believe that these findings demonstrate the importance of both flow focusing and PA fiber concentration in the production of superbundles. In this process, there needs to be a sufficient PA concentration to make a robust network, and a high enough FRR must be used to impinge and shape the PA flow so that the gelator stream can surround and gel it into the shape that the PA stream is confined in.

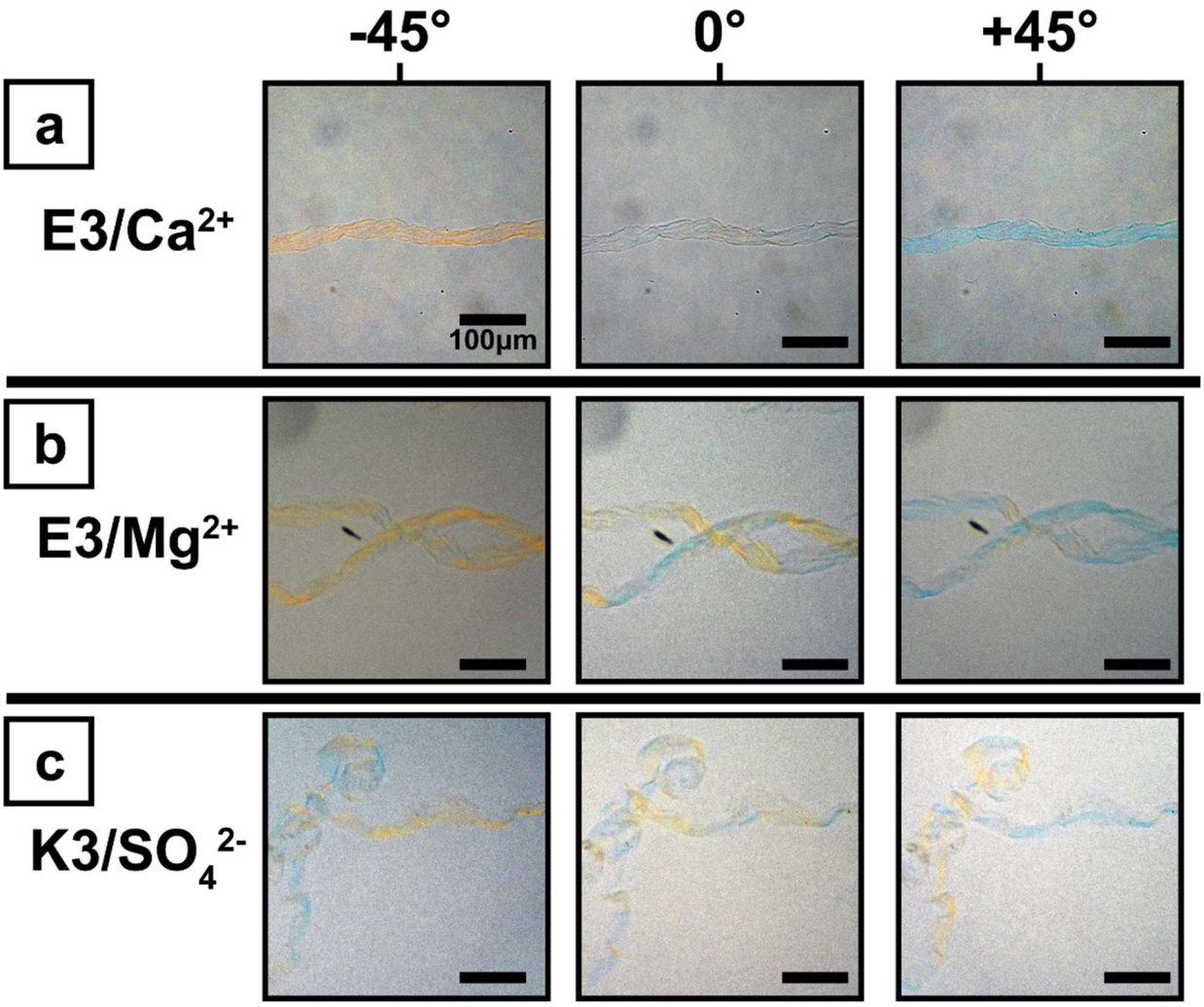

Figure 3.4: Polarized optical microscopy with images rotated to register relative to each other, a retardation plate was used with background auto-white balanced, and contrast enhanced for visibility, of 0.5 wt% E3 gelled with Ca^{2+} and extruded at FRR 10.

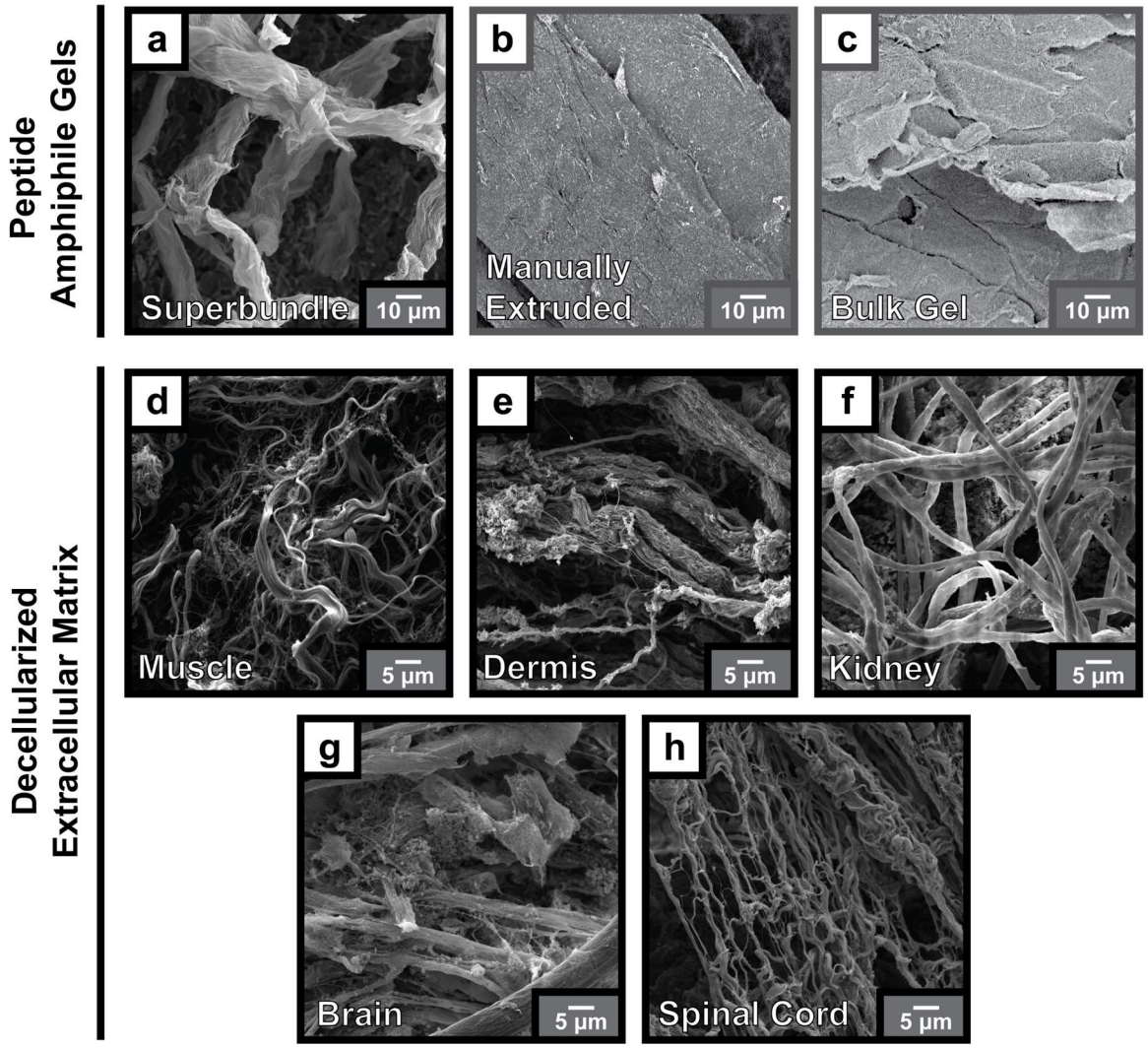

Figure 3.5: Scanning electron micrographs of: (a) SBs formed using Ca^{2+} and E3, (b) manually extruded gel formed using Ca^{2+} and E3, (c) a bulk gel formed using Ca^{2+} and E3, (d) decellularized murine muscle, (e) decellularized murine dermis, (f) decellularized murine kidney (g) decellularized murine brain, and (h) decellularized murine spinal cord.

When evaluating the size and morphology of SBs (Figure 3.5a), we found that they do not resemble previously reported PA gels. Monodomain, manually extruded, PA gels (Figures 3.5b and 3.6), which are formed by injecting PA from a pipet into a bath of gelator while applying tensile stress to the growing gel, exhibit monodomain gel characteristics[58] but have millimeter scale diameters. Bulk gels (Figures 3.5c and 3.6), which are formed by the gelation of a static PA

solution, exhibit minimal micron-scale alignment. SBs exhibit both strong micron-scale alignment and micron scale diameters. These two SB characteristics mimic the morphology of decellularized extracellular matrix (dECM). dECMs are a well-established class of tissue engineering scaffolds created by harvesting allograft[201] or xenograft[202] tissue and removing the cellular material with detergents. After washing, the remaining structure consists of extracellular matrix proteins, such as collagen and elastin, as well as non-protein components such as glycosaminoglycans.[195] dECM attempts to preserve the chemical and non-chemical cues presented on the extracellular matrix that cells respond to while removing other immunogenic material. Following removal of the cellular components from murine muscle, skin, kidney, brain, and spinal cord tissue, the resulting dECMs are microfibrous, entangled networks (Figures 3.5d-h, respectively). When comparing the top and bottom sections of Figure 4, it is evident that the dECM samples in the bottom row do not resemble the manually extruded (Figure 3.5b) or bulk gels (Figure 3.5c) but are markedly similar to the SB samples (Figure 3.5a). The ability to append different protein mimetic epitopes to PA molecules[203–206] means that SBs could serve as a morphologic and chemical mimic of dECM.

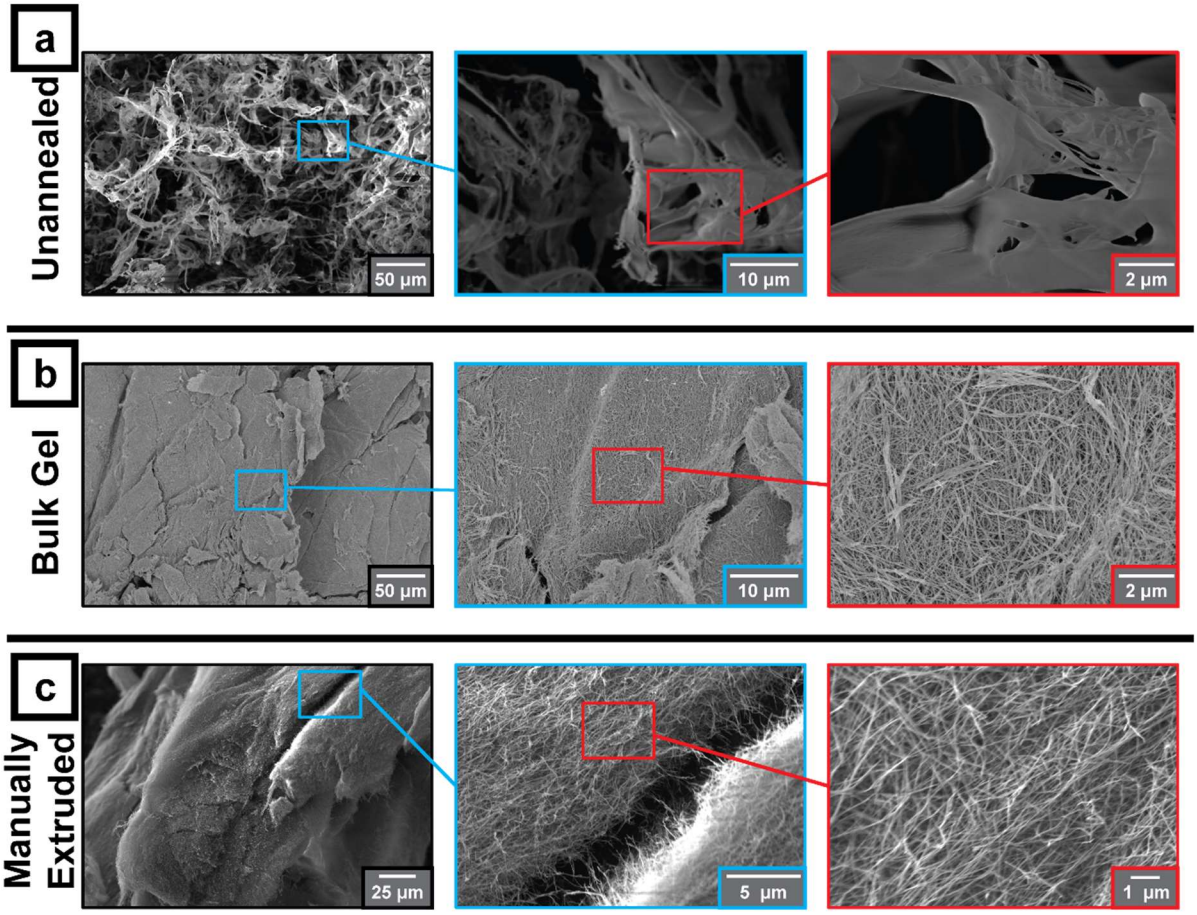

Figure 3.6: Scanning electron micrographs of (a) unannealed PA, (b) bulk PA gel and (c) manually extruded PA gel at various magnifications.

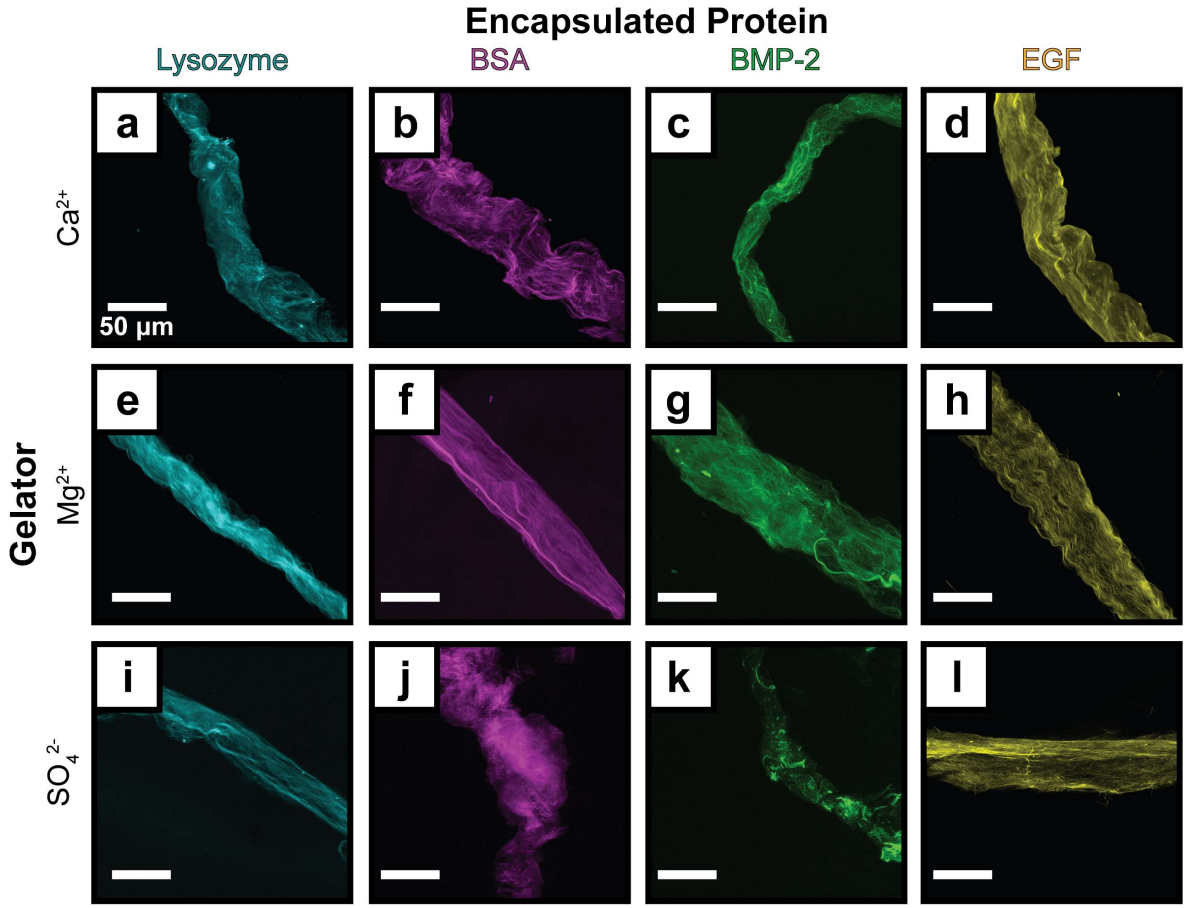

Figure 3.7: Maximum intensity projections of confocal microscopy z-stacks of (a) SBs produced using Ca^{2+} and E3 with encapsulated lysozyme (cyan), (b) SBs produced using Ca^{2+} and E3 with encapsulated BSA (magenta), (c) SBs produced using Ca^{2+} and E3 with encapsulated BMP-2 (green), (d) SBs produced using Ca^{2+} and E3 with encapsulated EGF (yellow), (e) SBs produced using Mg^{2+} and E3 with encapsulated lysozyme (cyan), (f) SBs produced using Mg^{2+} and E3 with encapsulated BSA (magenta), (g) SBs produced using Mg^{2+} and E3 with encapsulated BMP-2 (green), (h) SBs produced using Mg^{2+} and E3 with encapsulated EGF (yellow), (i) SBs produced using SO_4^{2-} and K3 with encapsulated lysozyme (cyan), (j) SBs produced using SO_4^{2-} and K3 with encapsulated BSA (magenta), (k) SBs produced using SO_4^{2-} and K3 with encapsulated BMP-2 (green), and (l) SBs produced using SO_4^{2-} and K3 with encapsulated EGF (yellow).

The delivery of therapeutic proteins is of high interest in tissue engineering. Previous work has shown that PA gels can deliver protein,[47,71,207,208] and we hypothesized that proteins could be readily incorporated into SBs. To explore this hypothesis, we used lysozyme, which has a net positive charge in physiologic conditions (isoelectric point ~11), bovine serum albumin (BSA),

which has a net negative charge in physiologic conditions (isoelectric point ~5), bone morphogenetic protein 2 (BMP-2) which has a net positive charge in physiologic conditions (isoelectric point 8.5), and epidermal growth factor (EGF) which has a net negative charge in physiologic conditions (isoelectric point ~4.6). We chose these proteins because they have a range of different isoelectric points, BSA and lysozyme are common model proteins, BMP-2 is a commonly used protein in osteo-regenerative medicine,[209] and EGF has promoted dermal wound healing.[210] To incorporate the protein into the superbundles, Alexa Fluor 647-labeled lysozyme, Alexa Fluor 647-labeled BSA, or Alexa Fluor 488-labeled BMP-2 was incorporated into a pre-annealed PA solution before injection into the microfluidic device, where the PA-protein solution was then extruded at an FRR of 10. These SBs were then imaged using confocal laser scanning microscopy. Interestingly, we found that both the positively and negatively charged proteins were readily encapsulated regardless of whether negatively (Figures 3.7a-h) or positively charged (Figures 3.7i-l) PAs were used. These SBs were formed used inorganic ionic gelation, and no oppositely charged polymers were used to form these SBs, so there was an even distribution of protein and no localization of protein was observed because no diffusion barriers or oppositely charged motifs are present in the scaffolds. PA superbundles present a platform to incorporate protein into a scaffold that mimics the morphology of the extracellular matrix, providing the ability for researchers to present tailored physical and biochemical cues for biomedical applications.

3.3 Conclusion

In this work, we constructed hierarchical, biomimetic superbundles out of supramolecular nanofibers using a flow-focusing microfluidic device. We developed design rules for creating these superbundles with multivalent salts and noted SB's striking morphological resemblance to

decellularized extracellular matrix, a well-established class of tissue engineering scaffolds. To demonstrate this platform's versatility, we expanded our library of SB producing gelators to include a variety of multivalent ions and showed that SBs are capable of encapsulating proteins as cargo. Superbundles' biomimetic microstructure, tunable network chemistry, and ability to encapsulate proteins demonstrate their promise as a biomaterial platform for regenerative medicine and tissue engineering.

3.4 Materials and Methods

Silicon Master Mold Fabrication: Silicon wafers were prepared for patterning by spin-coating AZ P4620 at 2000rpm. Photoresist was pre-baked at 110 °C for 60 seconds.

Microfluidic devices were designed in Autodesk AutoCAD and exposed on the photoresist coated wafers using a maskless aligner (Heidelberg MLA150) with an exposure value of 600 mJ/cm^2. Wafers were developed in AZ 400K 1:4 for 90 seconds. The patterned wafers were thoroughly washed with DI water, dried with N_2 and transferred to a deep reactive ion etching chamber (STS LpX Pegasus) where they were etched to a depth of 85µm. The remaining photoresist was stripped from the wafers, and device fidelity was confirmed using optical profilometry (Zygo nexview). These etched wafers were treated with trichloro(1H,1H,2H,2H-perfluorooctyl)silane (Sigma-Aldrich) under vacuum for 30 minutes to form a non-adhesive monolayer. A device design schematic can be found in Figure 3.8.

Soft Lithography: Sylgard 184 elastomer base (Dow Chemical) and sylgard 184 curing agent were thoroughly mixed in a 10:1 weight ratio before being degassed for 1 hour in a vacuum chamber. A prepared, patterned wafer was placed into an aluminum foil boat and placed on a cool hotplate.

The degassed Sylgard mixture was poured into the boat, and the hotplate was heated to (70 °C) for 1 hour. After cooling to room temperature, the cured polydimethylsiloxane (PDMS) polymer cast was removed from the silicon wafer and divided into individual devices as needed. Access ports were created using a 0.5 mm Rapid-Core sampling tool (Electron Microscopy Sciences). The exit port was punched using an 8.00 mm biopsy punch (Harris Uni-Core) at a variable distance from the microfluidic junction, based on the gelation system in use. The final microfluidic devices were assembled by adhering the access port punched PDMS cast to a sheet of flexible PCR tape (ThermalSeal RTS Sealing Film).

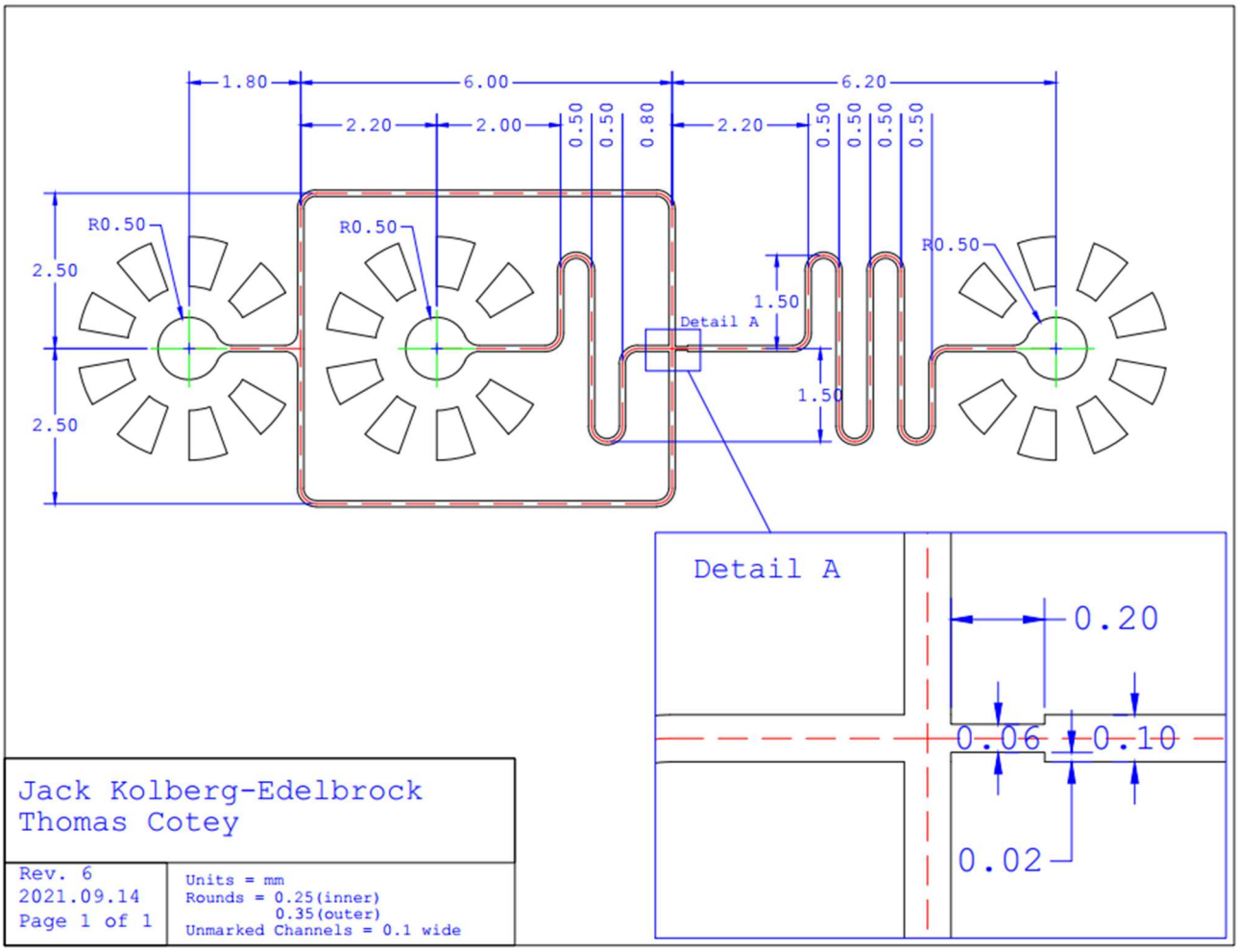

Figure 3.8: Annotated drawing with junction detail of the microfluidic device used in this project. All channels in the finished device have a depth of 85 µm.

Extrusion protocol: Extrusion experiments were performed using a pressure controller with flow-rate sensor (Elveflow OB3+ and Elveflow MFS3, respectively). A gelator solution was placed in series with a mass flow sensor (MFS), and an annealed PA solution was placed in series with a separate MFS. After flowing through the MFS, each respective solution was directed into the appropriate microfluidic entry port using tygon tubing (inner diameter 0.020 inches, outer diameter 0.060 inches; Cole Parmer catalog #SK-06419-01) and metal nipples (inner diameter 0.017 inches,

outer diameter 0.025 inches, and length 0.500 inches; New England Small Tube catalog #NE-1300-01). After assembly, extrusion FRR was controlled using the Elveflow Smart Interface Software (Figure S5). Experiments using Ca^{2+} or K3 as gelators were performed using a serpentine pathway in the microfluidic devices. Gelation with chitosan was performed in microfluidic devices without a serpentine pathway. A schematic of the microfluidic set-up can be found in Figure 3.9.

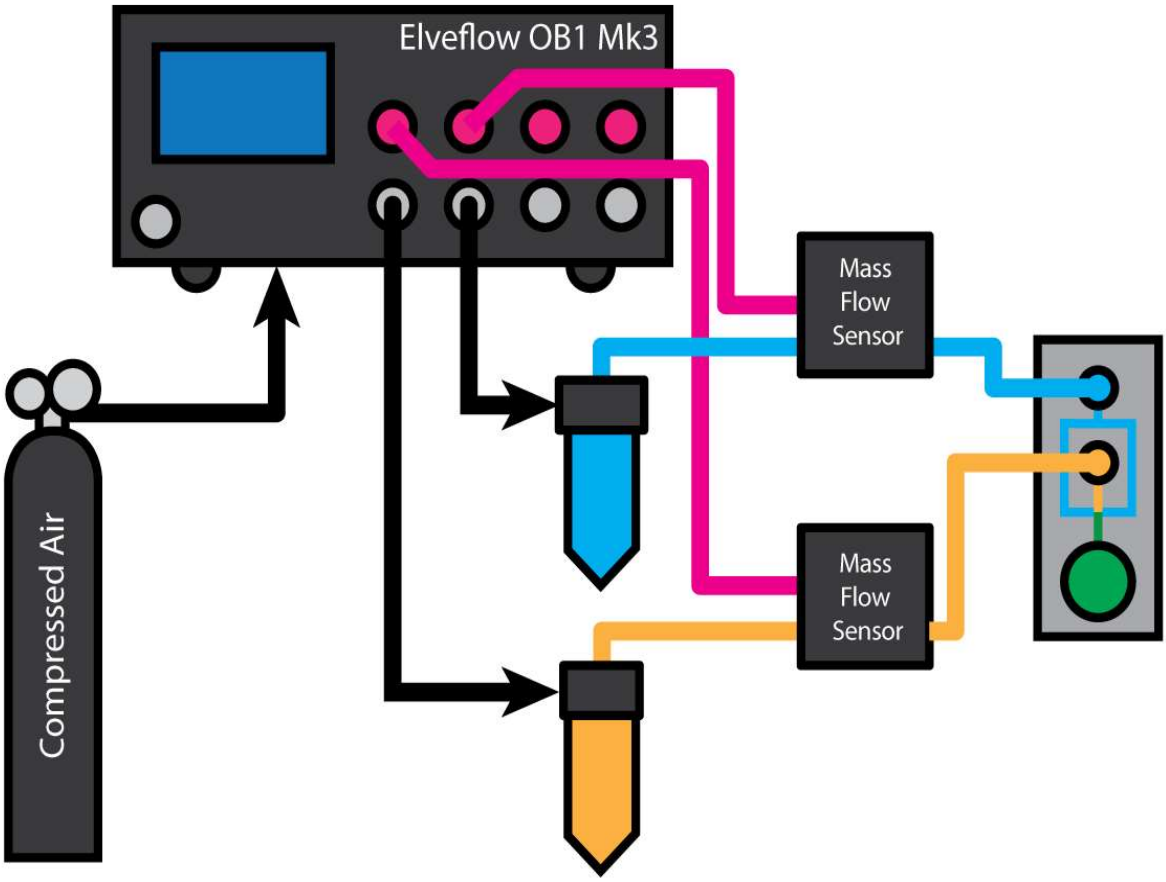

Figure 3.9: Diagram of microfluidic control system (not to scale). An Elveflow OB1 Mk3 pressure controller with two mass flow sensors were used to maintain constant flow rates throughout each experiment. Fluids were stored in reservoirs which were placed under positive pressure to drive them through tubing and into the microfluidic device.

Confocal microscopy: Solutions containing microfluidic extrudate were pipetted onto a glass slide, covered with cover glass, and imaged on a Nikon A1R Confocal Microscope. The 488 nm laser

was used for imaging Alexa Fluor 488-labeled BMP-2. The 561 nm laser was used for imaging TAMRA-E3. The 640 nm laser was used for imaging Alexa Fluor 647-labeled BSA (Invitrogen), Alexa Fluor 647-labeled lysozyme, and Cy5-K3.

Scanning electron microscopy: Samples suspended in water were lightly sedimented using a benchtop centrifuge. This sediment was transferred to a microporous specimen capsule (Electron Microscopy Sciences). Samples inside the specimen capsule underwent a solvent exchange from water to ethanol by incubation in a series of solutions of increasing ethanol concentration (30%, 40%, 50%, 60%, 70%, 80%, 85%, 90%, 95%, 100%) for 30 minutes per solution. After the ethanol exchange, samples were transferred to a critical point drier (Tousimis Samdri) and processed according to the manufacturer's instructions. The critical point dried samples were mounted on aluminum sample stubs coated with conductive carbon tape. Before imaging, samples were coated with 16nm of Osmium (Filgen Osmium Plasma Coater OPC60A). Samples were then imaged in the SEM (JEOL 7900 FLV) using an accelerating voltage of 5kV.

Morphology Scoring: Morphological analysis of superbundle samples was performed by double-blinded review by a panel of independent reviewers. Briefly, three representative images of each extrusion condition were collected using confocal microscopy and standardized for brightness and contrast in imageJ. Panelists were asked to score the images on a scale of 1-5 using the following scale:

1 - no evidence of ribbons – only filamentous aggregates

2 - mostly aggregates, some ribbons

3 - equal amounts of ribbons and filamentous aggregates

4 - mostly ribbons, some aggregates

5 - only ribbons – no filamentous aggregates

The results from each scorer were averaged to give n=3 for each extrusion condition. These scorer averages were then averaged with, at minimum, two additional scorers to provide $n \geq 9$ for the scoring of each extrusion condition. Statistical data for each scoring condition may be found in Figure 3.10.

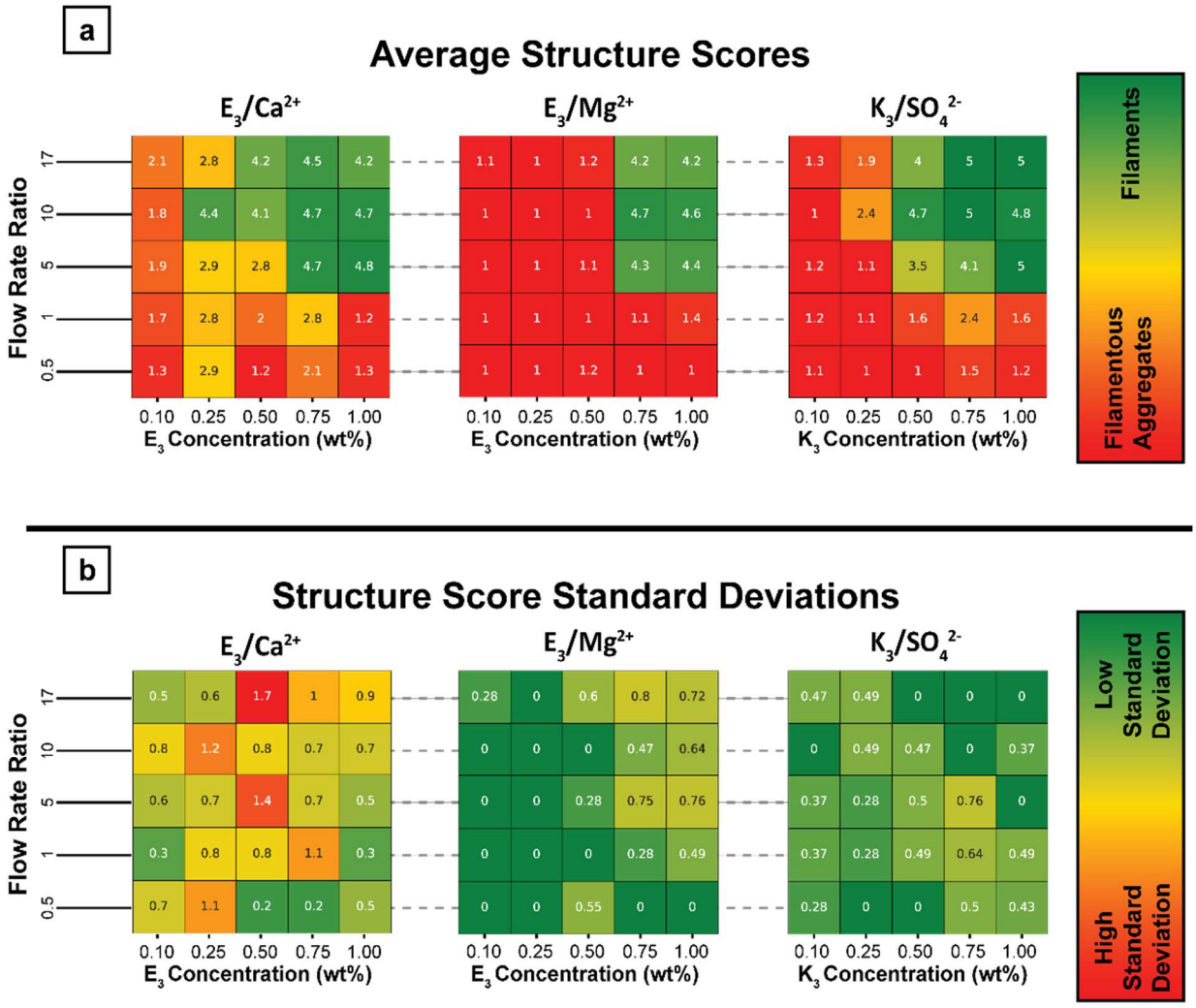

Figure 3.10: (a) Averaged morphology scores for processing parameter diagrams shown in Figure 3. (b) Population standard deviations for the morphology scores of each condition in the processing parameter diagrams.

Peptide Synthesis: the peptide amphiphiles (PAs) C16-VVVAAAEEE, C16VVVAAAEEE-TAMRA, C16-VVVAAAKKK, and C16-VVVAAAKKK-K(Cyanine5) were synthesized via standard 9-fluorenyl methoxycarbonyl (Fmoc) solid-phase peptide chemistry on Rink amide MBHA resin using a CEM Liberty Blue automated microwave peptide synthesizer. Automated coupling reactions were performed using 4 eq. Fmoc-protected amino acid or palmitic acid (C16),

4 eq. of *N*,*N'*-diisopropylcarbodiimide (DIC), and 8 eq. ethyl(hydroxyimino)cyanoacetate (Oxyma pure). Removal of the Fmoc groups was achieved with 20% 4-methylpiperidine in DMF. Peptides were cleaved from the resin using standard solutions of 95% TFA, 2.5% water, 2.5% triisopropylsilane (TIS) for 3 h, precipitated with cold ether, and then purified by reverse-phase HPLC on a Waters Prep150 or Shimadzu Prominence HPLC using a water/acetonitrile (each containing 0.1% TFA v/v) gradient. Eluting fractions containing the desired peptide were confirmed by mass spectrometry using an Agilent 6520 QTOF LCMS. Confirmed fractions were pooled and the acetonitrile was removed by rotary evaporation before freezing and lyophilization. Purity of lyophilized products was tested by LCMS.

For the TAMRA (5-carboxytetramethylrhodamine) labeled PA, N-α-Fmoc-N-ε-4-methyltrityl-L-lysine (lysine(Mtt)) was used as the C-terminal residue. After automated synthesis of the full sequence, the methytrityl (Mtt) protecting group was removed from the lysine while still on resin using 3% TFA in DCM with 5% TIS (2 x 10 min additions). After washing with DCM and DMF, TAMRA was then coupled to the now free ε-amine of lysine using 1.2 eq. of TAMRA, 1.2 equivalents of PyBOP, and 8 eq. of DIEA for approximately 18 h.

For the Cyanine5 (3H- Indolium, 2- [5- [1- (5- carboxypentyl) - 1, 3- dihydro- 3, 3- dimethyl- 2H-indol- 2- ylidene] - 1, 3- pentadien- 1- yl] - 1, 3, 3- trimethyl- , chloride) labeled PA, N-α-Fmoc-N-ε-1-(4,4-dimethyl-2,6-dioxocyclohex-1-ylidene)-3-methylbutyl-L-lysine (lysine(ivDde)) was used as the C-terminal residue (others lysines Boc protected on the ε-amine). After automated synthesis of the full sequence, the ivDde protecting group was selectively removed from this C-terminal lysine while still on resin using 5% v/v hydrazine in DMF (2 x 20 min additions). The resin was then washed with DCM and DMF, and Cyanine5 carboxylic acid was coupled to the

now free ε-amine of the C-terminal lysine using 1.2 eq. of the dye, 1.2 eq. of PyBOP (benzotriazol-1-yl-oxytripyrrolidinophosphonium hexafluorophosphate), and 8 eq. of *N*,*N*-diisopropylethylamine (DIEA) for approximately 18 h.

PA structures used in Chapter 3 may be found in Table 3.1.

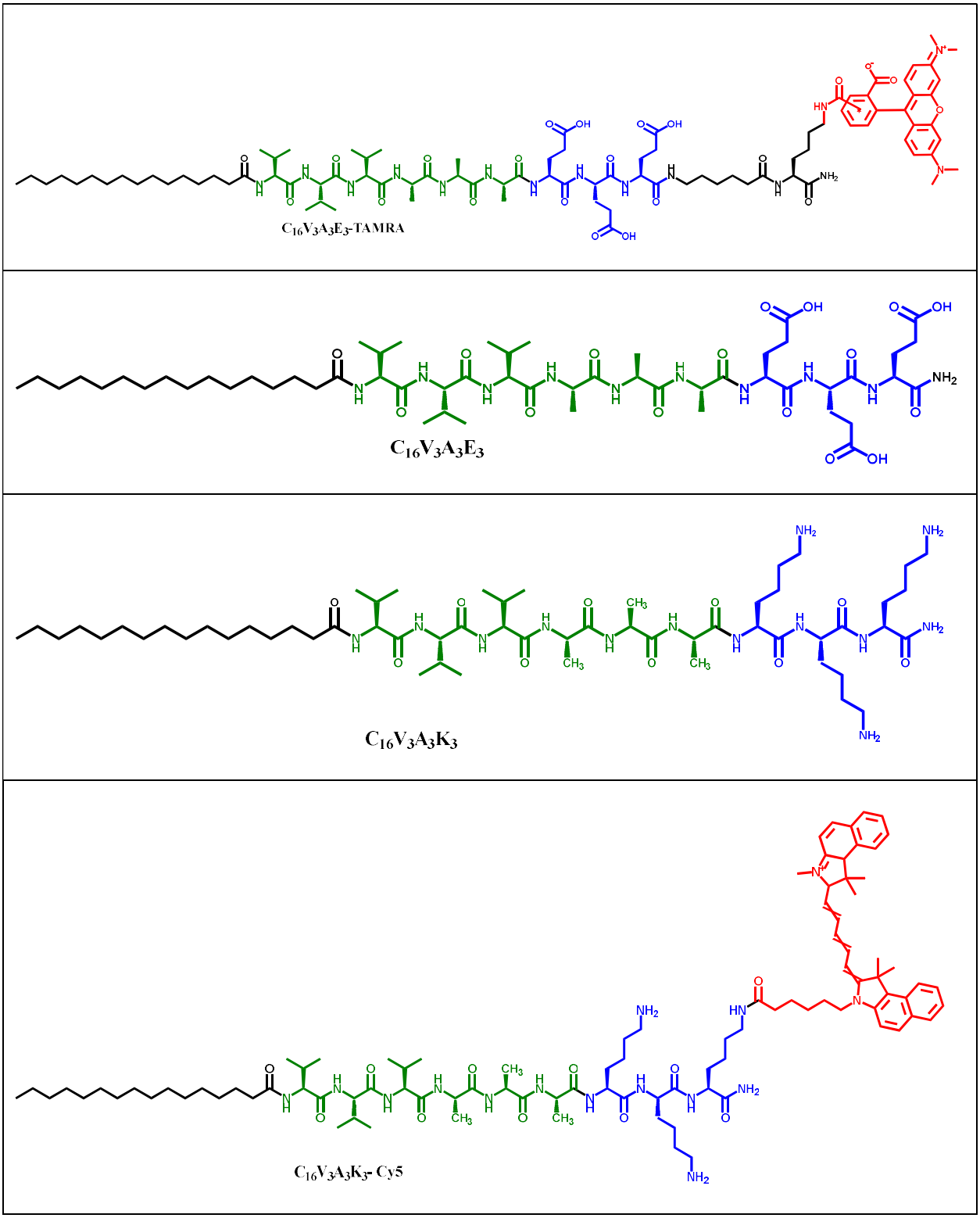

Table 3.1: PA Structures

E3 Solutions: lyophilized E3 PA powder was added to 150 mM NaCl, 3 mM KCl solution. Three equivalents of sodium hydroxide were added and the mixture was vortexed until dissolved. pH was adjusted to 7 using 1 M sodium hydroxide. Solutions were heated in a thermocycler at 80 °C for 30 minutes and then cooled to room temperature at a rate of 1 °C per minute.

TAMRA-E3/E3 co-assemblies: a 0.1 wt% solution of TAMRA-E3 PA in a 150 mM NaCl, 3mM KCl solution was added by displacement pipet to an unannealed E3 PA solution to give a final concentration of 0.1mol% TAMRA-E3 PA. The mixture was horn sonicated at 10% power for 10 seconds to disperse the dye PA. Solutions were placed in a thermocycler at 80 °C for 30 minutes and then cooled to room temperature at a rate of 1 °C per minute.

K3 solutions: to prepare solutions, 150 mM NaCl with 3 mM KCl was added to freeze dried PA powder. Solutions were then placed in an 80 °C water bath for 30 minutes and then cooled slowly down to room temperature.

Cy5-K3/K3 co-assemblies: to prepare co-assemblies of K3 with Cy5-K3, a 0.1 wt% solution Cy5-K3 dissolved in deionized water was mixed with a solution of K3 dissolved in a to 150 mM NaCl, 3 mM KCl solution. Cy5-K3 was 0.1 mol% of the total amount of PA in solution. The mixtures were then sonicated. Solutions were then placed in an 80 °C water bath for 30 minutes and cooled slowly down to room temperature.

Ca^{2+} gelator solution: a solution of 150 mM NaCl, 3 mM KCl, and 25 mM $CaCl_2$ was used as the gelator in all Ca^{2+} gelation studies.

BMP-2 labeling: Human recombinant Bone Morphogenetic Protein 2 (BMP-2, Biomatik Corporation) was dialyzed in a TUBE-O-DIALYZER mini dialysis system (micro, 4 kDa molecular weight cutoff, G-Biosciences) and labeled with Alexa Fluor 488 Microscale Protein Labeling Kit (Molecular Probes). 50 µg of BMP-2 (MW 43 kDa) was dissolved in 50 µL of MilliQ water. 5 µL of 1 M sodium bicarbonate and 7 µL of Alexa Fluor 488 tetrafluorophenyl (TFP) ester reactive dye stock solution were added to the protein solution and incubated at room temperature for 15 minutes. The dye-labeled protein conjugate was purified with a prepared spin filter with 800 µL of gel resin provided in the kit at 16,000 x g for 1 min. The final concentration of the purified dye-labeled BMP-2 was measured with Thermo Scientific NanoDrop ND-1000 spectrophotometer.

Additional multivalent salt gelators: a solution of 150 mM NaCl, 3 mM KCl, and 25 mM $MgCl_2$ was used as the gelator in all Mg^{2+} gelation studies. a solution of 150 mM NaCl, 3 mM KCl, and 25 mM Na_2SO_4 was used as the gelator in all SO_4^{2-} gelation studies.

Alexa Fluor 647-labeled lysozyme: lysozyme from chicken egg white (Sigma Aldrich) was dissolved in a 0.1 M sodium bicarbonate solution to a concentration of 10 mg/mL. Alexa Fluor 647 carboxylic acid succinimidyl ester (1 mg, Thermo-Fisher) was dissolved in 100 µL of dimethylformamide and added to the room temperature lysozyme solution that was stirring using a magnetic stir bar. The solution was continuously stirred for one hour, and then the reaction was terminated by adding 200 µL of a 1 M hydroxylamine aqueous solution (pH 8). The solution was then stirred for 1 more hour. The lysozyme labeled with Alexa Fluor 647 was then purified by dialysis in deionized water for 48 hours using Spectra/Por 3.5 kDa Mw cutoff dialysis tubing and then lyophilized and stored at -20 °C.

EGF Labeling: Lyophilized recombinant human epidermal growth factor (EGF, R&D Systems) was reconstituted to 10 mg/mL with sterile PBS. 1 M NaHCO3 was added to the protein solution to bring the pH to 8.3. 10 μL of Alexa Fluor 647 NHS ester (Thermo Fisher Scientific) dissolved in DMSO at 10 mg/mL was added to the reaction mixture and incubated for 2 hours at room temperature. 10 μL of 1.5 M hydroxylamine hydrochloride was added, and the mixture was incubated for 1 hour to quench the reaction. The mixture was transferred to TUBE-O-DIALYZER mini dialysis system, micro, 4kDa molecular weight cutoff (G-Biosciences) and dialyzed for 5 days in PBS. A Thermo Scientific NanoDrop ND-1000 spectrophotometer was used to measure the concentration of the purified dye labeled EGF.

Encapsulation of Protein in Superbundles: Alexa Fluor 647-labeled lysozyme or Alexa Fluor 647-labeled BSA (Invitrogen) was dissolved to 0.25 mg/mL in a pre-annealed PA solution at room temperature. Alexa Fluor 488-labeled BMP2 was dissolved in PBS at 0.28 mg/mL, then mixed with a pre-annealed PA solution at room temperature to achieve a final concentration of 0.046 mg/mL. These solutions were gelled the microfluidic device with various gelators using FRR 10 to form SBs. PA concentration 0.5 wt% for encapsulation experiments.

Decellularized Extracellular Matrix: All animal housing and procedures were performed in accordance with the Public Health Service Policy on Humane Care and Use of Laboratory Animals. All procedures were approved by the Northwestern University Institutional Animal Care and Use Committee. Tissue samples were harvested from a CD1 adult, female mouse (Charles River Laboratories). The collected tissues were cut into 2-3mm pieces and placed in deionized water at 4 °C overnight. All remaining steps were performed at 25 °C with agitation.

- Rinse 2 x 1 hour in phosphate buffered saline (PBS, gibco).
- Wash 1 x 3 hours in a 1% Triton X-100 (Sigma Aldrich) solution in PBS.
- Rinse 3 x 1 hour in PBS.
- Wash 1 x 3 hours in a 1% sodium deoxycholate (Sigma-Aldrich) solution in PBS.
- Rinse 3 x 1 hour in PBS..
- Wash 1 x 3 hours in a 1% Triton X-100 solution in PBS.
- Rinse 1 x 1 hour in PBS.
- Wash 1 x 3 hours in a 1% sodium deoxycholate solution in PBS.
- Rinse 3 x 1 hour in PBS.

Samples were stored in PBS at 4 °C until they were prepared for SEM imaging.

Polarized Optical Microscopy: solutions containing extrudate were placed onto a glass slide, and then the solutions were covered with cover glass. A Nikon Eclipse LV100N Polarized Optical Light Microscope was used. For images taken with the first order, full wavelength retardation plate, the field of view was auto white balanced against background using Nikon NIS Elements software to improve the ease of alignment visualization. Images were contrast enhanced to make yellow and blue visible in print media.

CHAPTER 4: Microfluidic Superstructuring of Biomaterials Based on Covalent and Supramolecular Polymers

4.1 Background

The structural and chemical tunability of supramolecular materials have led to numerous applications in regenerative medicine[5,211–213] and drug delivery.[163,214–216] Peptide amphiphiles (PAs) are a class of molecules that contain a peptide sequence synthetically modified with a hydrophobic moiety to induce self-assembly in aqueous solution.[19,41] The Stupp Laboratory has pioneered the research of PA nanostructures that utilize the competitive intermolecular interactions of hydrogen bonding within β-sheet forming peptide sequences and charged peptide sequences that promote solubility.[4,42,43] In aqueous solution, the formation of β-sheets coupled with hydrophobic collapse due to the aliphatic tail results in the formation of one-dimensional nanostructures[19,35,44] that can be used to bind growth factors[46,47,52,217] as well as display bioactive epitopes.[45,51,211,218,219]

A previous study from the Stupp Laboratory found that bringing a solution of the positively charged PA C16V3A3K3 (K3) into contact with a solution of the negatively charged polymer hyaluronic acid resulted in the formation of hierarchical membranes.[61] Immediately after the solution of positively charged PA met the solution of negatively charged polymer, an interfacial contact layer formed due to electrostatic interactions. Following formation of the contact layer, the hyaluronic acid diffused, driven by an osmotic pressure difference between the PA and polymer solution, into the PA compartment and nucleated self-assembly of PA fibers perpendicular to the initial contact layer.[61] Further studies investigated these hierarchical membranes' application in biomedicine[68,71,220] as well as their physical properties.[62–64,179] Subsequent works using oppositely

charged PA and polymer solutions reported systems that display morphogenesis,[66] structures made by droplet printing,[67] layer-by-layer films,[65] and bulk gels through complexation during rapid chaotic flow.[221]

Microfluidic devices that utilize flow focusing, a method of hydrodynamic shaping via the impingement of multiple fluids at a junction during laminar flow, allow for the formation of a stable interface during a continuous process.[222,223] This provides the ability to carefully control interactions such as chemical reactions and diffusion.[99,101,224] A recent study from the Stupp Laboratory shown in Chapter 3 demonstrated that a solution of peptide amphiphiles nanofibers could be gelled using a solution of multivalent inorganic ions in a flow focusing microfluidic device, yielding a superstructure with remarkable resemblance to extracellular matrix, the biological framework that chemically and mechanically supports tissue. We termed these structures "superbundles" and defined them as high aspect ratio, aligned superstructures with microscale widths containing many PA nanofibers. Here, we investigate superbundles formed via the complexation of PAs with covalent as well as supramolecular polymers in a flow-focusing microfluidic device.

4.2 Results and Discussion

In order to produce superbundles (SBs) in a continuous process, we used soft lithography to produce polydimethylsiloxane microfluidic devices (Figures 4.1a and 4.1b) that incorporated a four-way junction where a solution of PA was impinged on both sides by a gelling solution (Figure 4.1c). The impinging gelator solution shapes the PA flow in the junction in a process known as flow focusing, confining the PA flow within a sheathing flow, where the use of shear and elongational flows within the device allows for the alignment of the PA nanofibers during gelation.

After the fluids meet at the junction, they flow through the rest of the device before being extruded into a collection bath. Depending on the gelator, a serpentine can be included (Figure 4.1b) that provides extra residence time within the device. The complexation of supramolecular polymers with oppositely charged covalent polymers has been the topic of great, recent interest. To explore whether SB formation could be achieved with polyelectrolyte complexation, we used an outer gelator flow containing the positively charged polymer chitosan. Chitosan is a biocompatible, biodegradable, naturally-derived copolymer of glucosamine and N-acetyl-glucosamine that has a wide range of uses as a biomaterial.[172] Complexation of PAs and oppositely charged covalent polymers occurs incredibly quickly at the interface of the solutions, resulting in the formation of a contact layer that acts as a diffusion barrier.[61,221] Because this complexation is so rapid, we performed microfluidic gelation of the negatively charged PA C16V3A3E3-OH (E3OH), which has a terminal carboxylic acid instead of an amide, with positively charged chitosan solutions in microfluidic devices that did not contain a terminal serpentine, as the additional residence time provided by a serpentine was unnecessary. Within the microfluidic device, laminar flows at low Reynolds numbers were used. Reynolds numbers are used to describe fluids during flow and the transition from turbulent (at high Reynolds numbers) to laminar (at low Reynolds numbers) flow. The Reynolds number can be described as the ratio of inertial and viscous forces in a fluid and can be defined with a general form that includes a characteristic linear dimension, L, the kinematic viscosity, ν, and the flow speed, u.

$$Re = \frac{uL}{\nu}$$

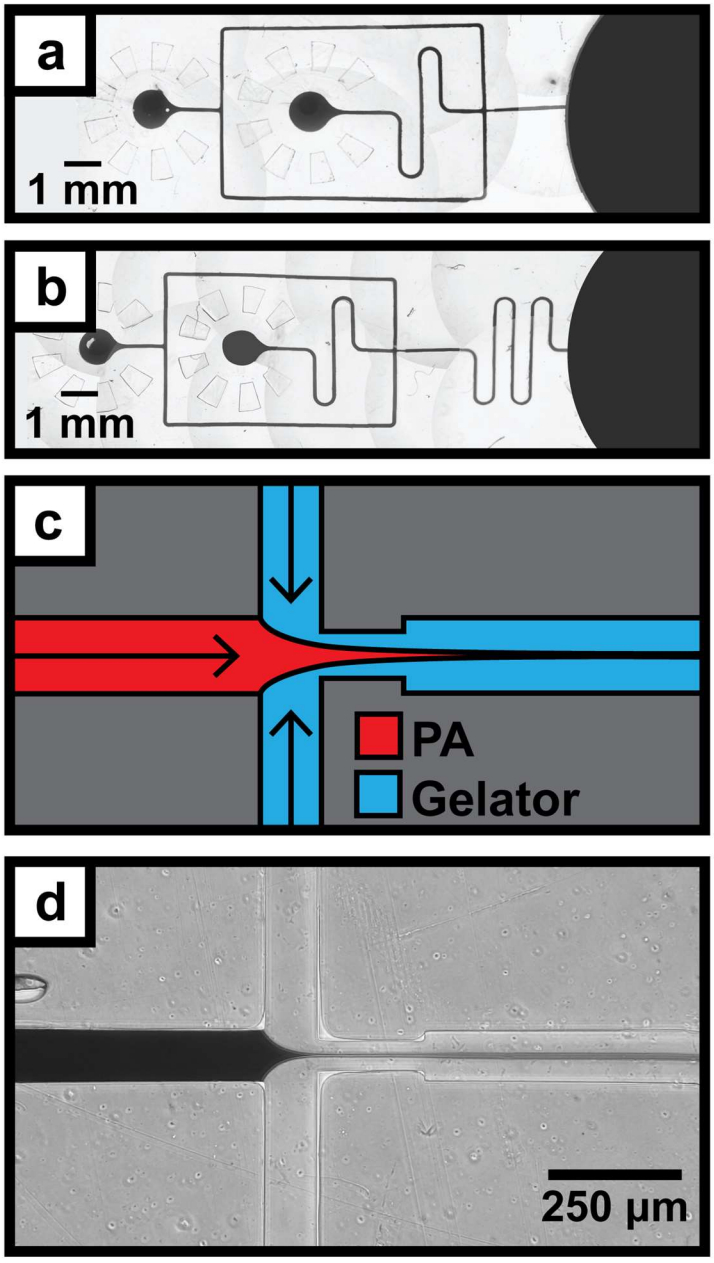

Figure 4.1: (a) Composite photograph of microfluidic device with no serpentine used to produce PA-covalent polymer superbundles, stitched from multiple images and enhanced for clarity. (b) Composite microfluidic device with serpentine used to produce PA-PA superbundles, stitched from multiple images and enhanced for clarity. (c) Schematic of the four-way junction where SBs are formed by gelation of the PA during flow focusing. (d) *In-situ* photograph of the flow focusing effect in the microfluidic device.

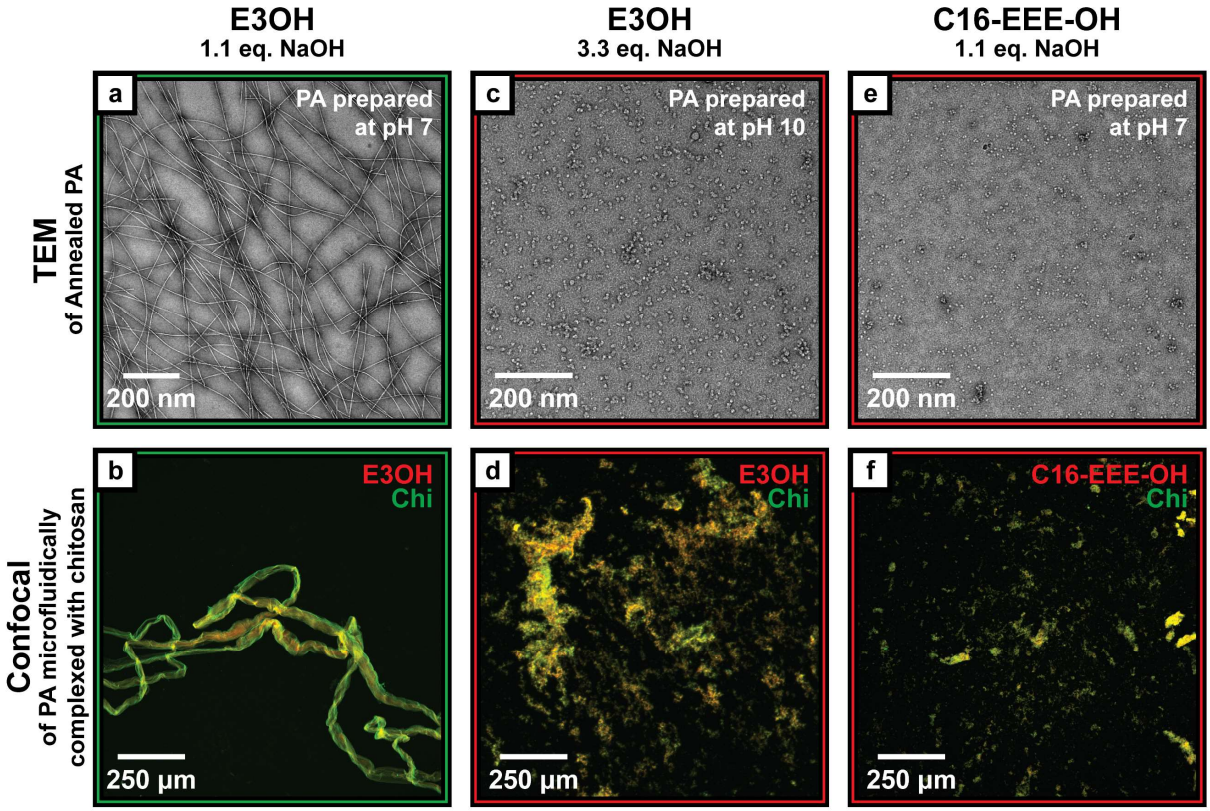

Figure 4.2: (a) Transmission electron microscopy (TEM) of E3OH fibers prepared in pH 7 solution. (b) Maximum intensity projection of a confocal micrograph z-stack (MAX) of SBs produced using FRR 10 from chitosan (green) and 1.0 wt% E3OH (red) nanofibers prepared in pH 7 solution. (c) TEM of E3OH micelles prepared in pH 10 solution. (d) MAX of aggregates produced using FRR 10 from chitosan (green) and 1.0 wt% E3OH (red) micelles prepared in pH 10. (e) TEM of C16-EEE-OH micelles prepared in pH 7 solution. (f) MAX of aggregates produced using FRR 10 from chitosan (green) and 1.0 wt% C16-EEE-OH (red) micelles prepared in pH 7 solution.

We were interested in investigating the effect of the supramolecular polymer's nanostructure on the ability to form superbundles, so we complexed PAs of varied morphology with chitosan in the microfluidic device shown in Figure 1a. C16V3A3E3-OH PA was formed into nanofibers by dissolving at 1 wt% in water at pH 7, annealing at 80 ºC, and slowly cooling to room temperature (Figure 4.2a). The solution of nanofibers was then complexed with chitosan in the flow focusing microfluidic device using a ten-fold greater flow rate of chitosan solution than the

PA solution. Complexation between the PA nanofibers and the covalent polymer requires strong electrostatic interactions, but thermodynamically, there is also an entropic drive to complexation. The complexation of the negative charges on the PAs and the positive charges on the covalent frees both counterions and associated water, resulting in an increase in entropy. This interfacial complexation is rapid, allowing for the structure to be locked in before leaving the microfluidic device. Using confocal microscopy, we identified successful production of superbundles when the PAs have a nanofiber structure (Figure 4.2b). The supramolecular structure of PAs is dependent on the pH of solution due to intermolecular electrostatic interactions,[176–178] and by increasing the pH to 10 with sodium hydroxide, micelles are formed rather than nanofibers (Figure 4.2c). A 1 wt% C16V3A3E3-OH annealed micelle solution at pH 10 was complexed with chitosan in the microfluidic device using a ten-fold greater flow rate of chitosan solution than the PA solution, and we observed the formation of precipitated aggregates (Figure 4.2d) rather than superbundles. To ensure that the formation of precipitates was due to supramolecular structure rather than charge effects, we synthesized the peptide amphiphile C16E3-OH, which forms micelles at neutral pH due to the lack of a β-sheet region (Figure 4.2e). A 1 wt% annealed micelle solution of C16E3-OH at pH 7 was complexed with chitosan at using a ten-fold greater flow rate of chitosan solution than the PA solution in the microfluidic device, yielding aggregates (Figure 4.2f). These results demonstrate the importance of supramolecular structure when forming PA-polymer superbundles, and this finding agrees with previous reports that showed nanofiber structure was crucial for the formation of bulk gels[221] and planar hierarchical membranes.[179] These findings demonstrate the importance of a robust contact layer for the production of superbundles During flow focusing within a microfluidic device. This contact layer that forms at the interface of the fluids traps the

PA stream into the shape formed during the impingement with the chitosan flow, preserving this structure in the final gelled superbundles that are extruded into the collection bath.

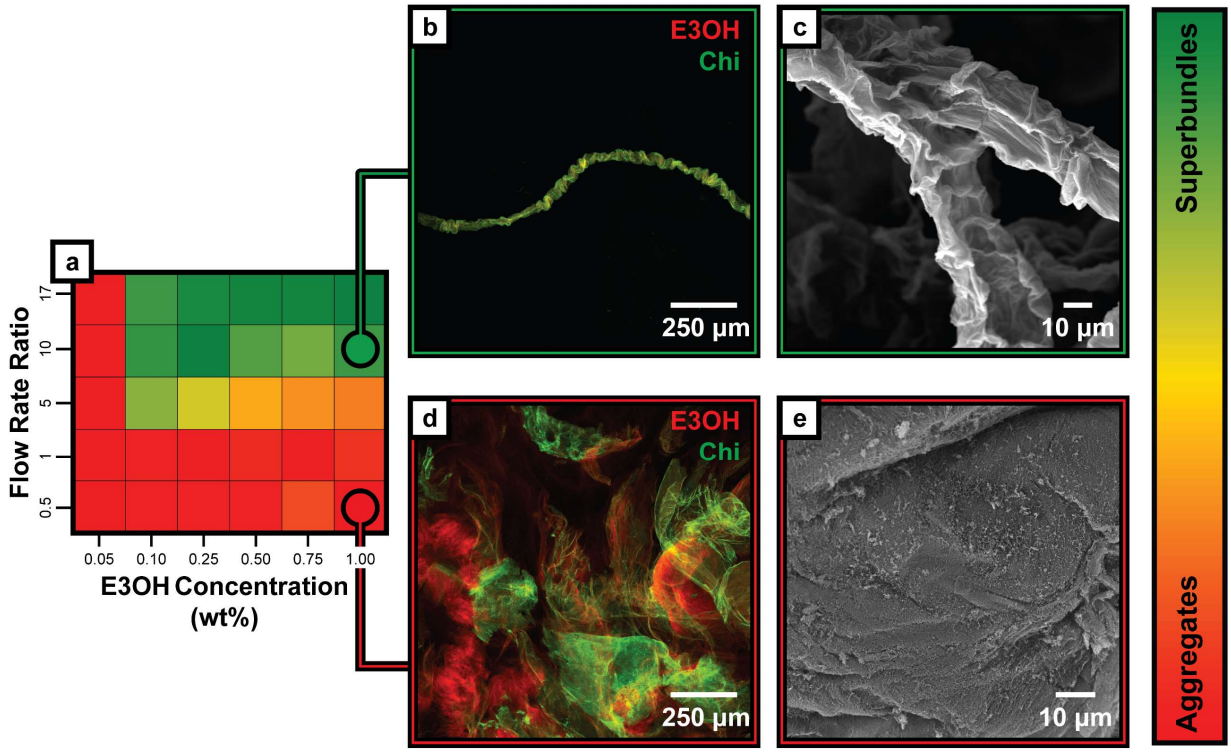

Figure 4.3: (a) Processing parameter diagram for E3OH solutions gelled with chitosan at varied FRRs and E3OH concentrations (green indicates SB formation, red indicates disordered gel production). (b) Maximum intensity projection of a confocal micrograph z-stack of SBs produced with chitosan (green) and 1.0 wt% E3OH (red) at FRR 10. (c) SEM of an SB produced with chitosan and 1.0 wt% E3OH at FRR 10. (d) Maximum intensity projection of a confocal micrograph z-stack of a gel produced with chitosan (green) and 1.0 wt% E3OH (red) at FRR 0.5. (e) SEM of a gel produced with chitosan and 1.0 wt% E3OH at FRR 0.5.

We hypothesized that the concentration of PA solution and the relative flow rates of the sheath and core solutions, as defined by the flow rate ratio (FRR), would be crucial parameters to

$$\text{FRR} = \dot{f}_{sheat} \ / \dot{f}_{core}$$

investigate when producing superbundles (SBs), so we performed experiments while varying both and evaluated the extrudate with a blinded multipoint scale that ranged from superbundles to

filamentous aggregates (Figures 4.3a). When using chitosan as the gelator, we observed the formation of long, continuous SBs (Figures 4.3b and 4.3c) for a wide range of PA concentrations when FRRs greater than 5 were used. We observed that at low flow rate ratios (FRRs) superbundles

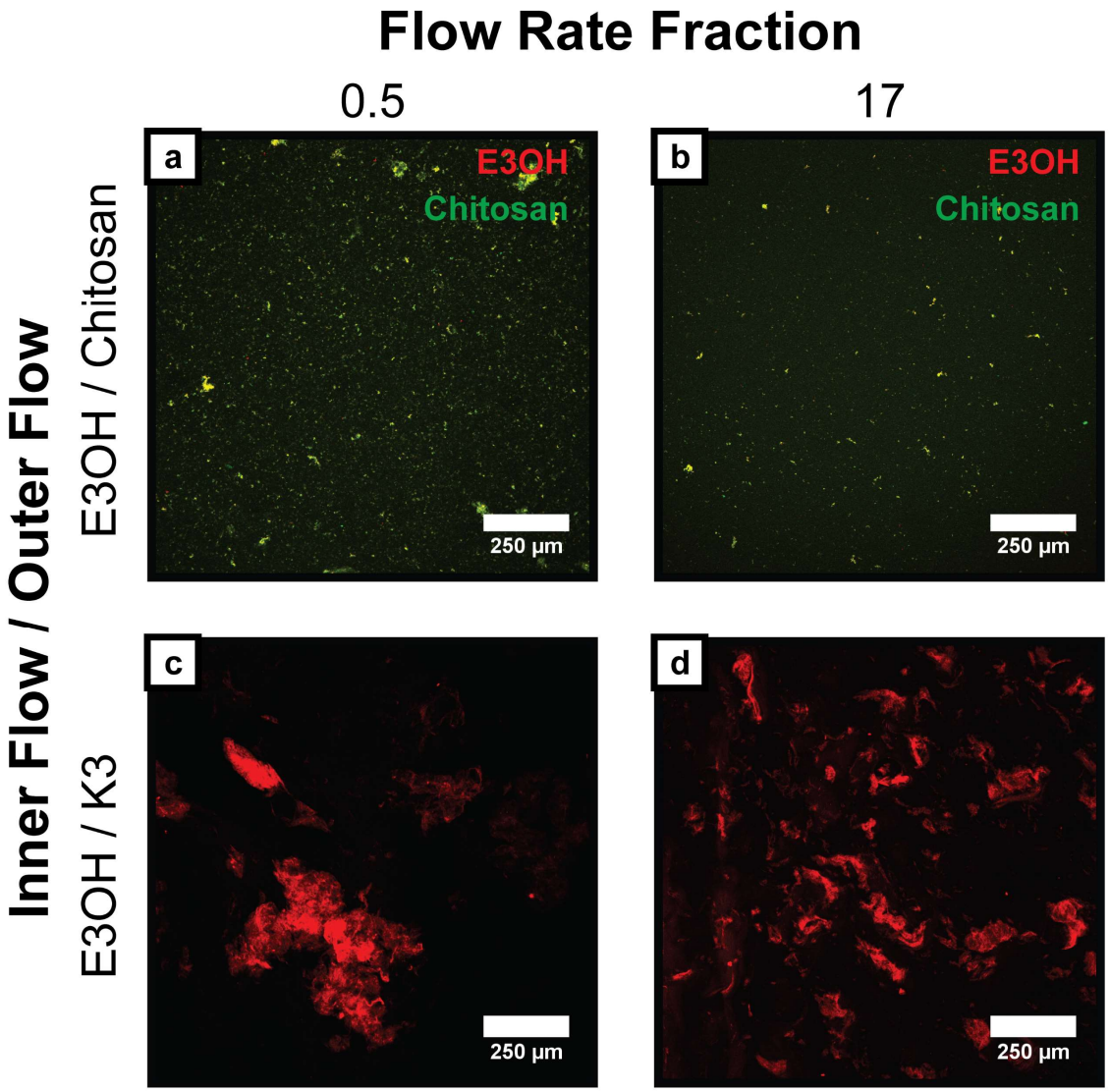

Figure 4.4: Maximum intensity projections of confocal micrograph z-stacks of (a-b) E3OH / Chitosan and (c-d) E3OH / K3 gels created with a 0.05 wt% inner solution, K3 undyed. E3OH concentration is 0.05 wt% for all conditions. Findings demonstrate that low core flow concentrations result in the formation of aggregates rather than superbundles.

were not formed. Instead, confocal and scanning electron microscopy revealed large aggregates (Figures 4.3d and 4.3e). Interestingly, the gels formed at low FRRs looked remarkably similar to gels formed using chaotic mixing between oppositely charged PA and polymer solutions.[221] At high FRRs, we observed the formation of long, continuous SBs for a wide range of PA concentrations. That high flow rate ratios are required to form superbundles demonstrates the importance of the shaping of the inner PA flow stream during impingement by the chitosan flow. This chitosan solution confines the PA stream, delaminating the PA stream from the device channel walls and encompassing the central PA stream so that complexation can occur conformally around the PA while it is being flow focused. At low E3OH concentrations, we found that superbundles were not produced, and instead, all FRRs yielded the formation of small particulates because there was not enough PA to form a cohesive network (Figure 4.4). Additionally, we found that varying total flow rate while keeping the FRR constant did not significantly alter the ability to form SBs. When the flow rate ratio was high, and total flow rate (Q_T),

$$Q_T = Q_{gelator} + Q_{PA}$$

was varied, superbundles were always produced, but when the FRR was low, aggregates were always produced instead (Figure 4.5), showing that controlling flow focusing is more important than total flow rates when forming superbundles and the total flow rate is responsible for how fast superbundles will be produced. Polarized optical microscopy of high FRR superbundles confirmed that the nanofibers were aligned in the extrusion direction (Figure 4.6) because PAs align during flow, and this anisotropy was locked by gelation. Previous studies have shown a variety of polymers can gel oppositely charged PAs.[61,63,66,67,221] To demonstrate these findings are applicable for formation of superbundles, we successfully used the polycation poly-D-lysine to gel E3OH

and the polyanion sodium hyaluronate to gel C16V3A3K3 PA (K3) into SBs (Figure 4.7). The ability to choose from a library of gelators broadens the scope of this material platform by allowing researchers to tailor the material chemistry of these tissue scaffolds for specific biomedical targets.

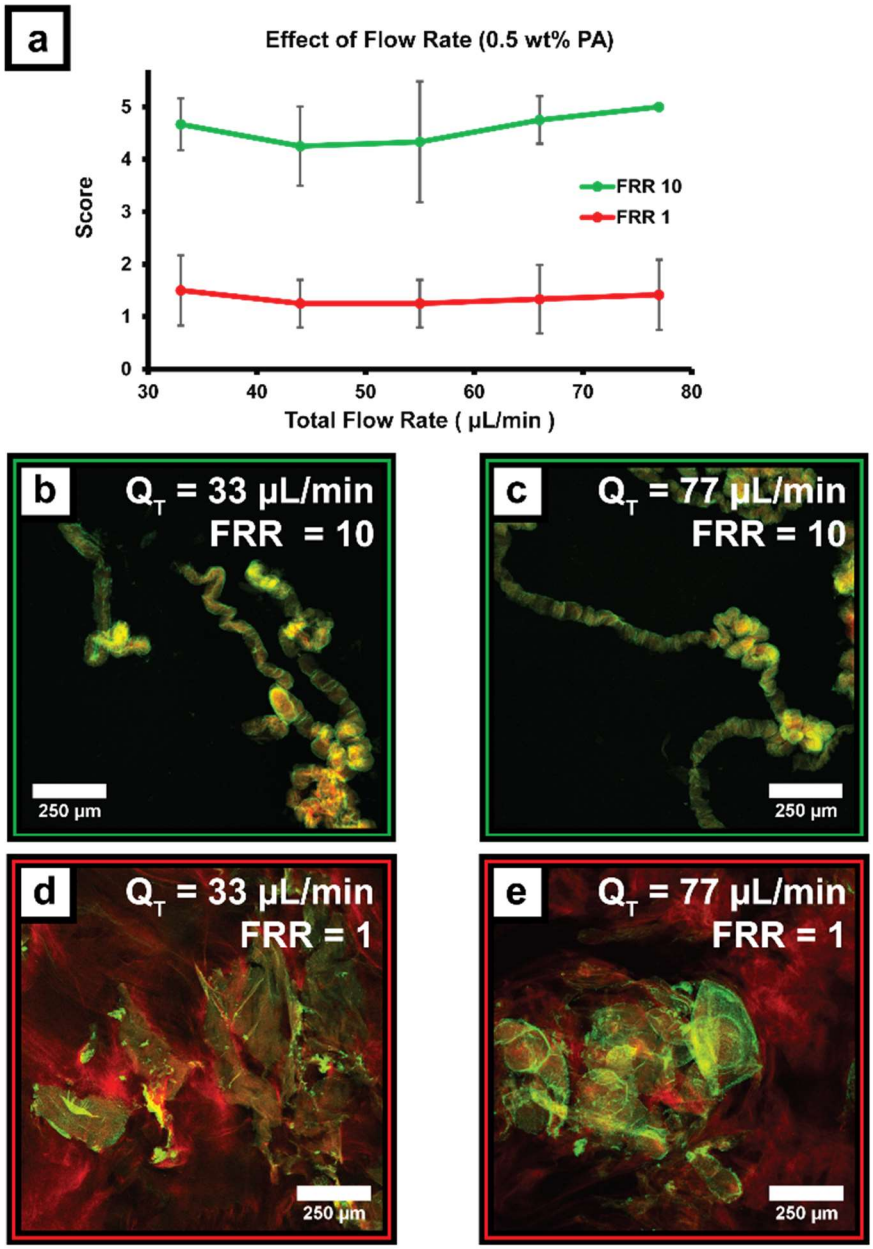

Figure 4.5: (a) plot of the score of gel samples prepared using E3OH gelled with chitosan with various total flow rates at FRRs of 10 and 1 with representative confocal maximum intensity projections (b-e) from select conditions with E3OH (red) and chitosan (green).

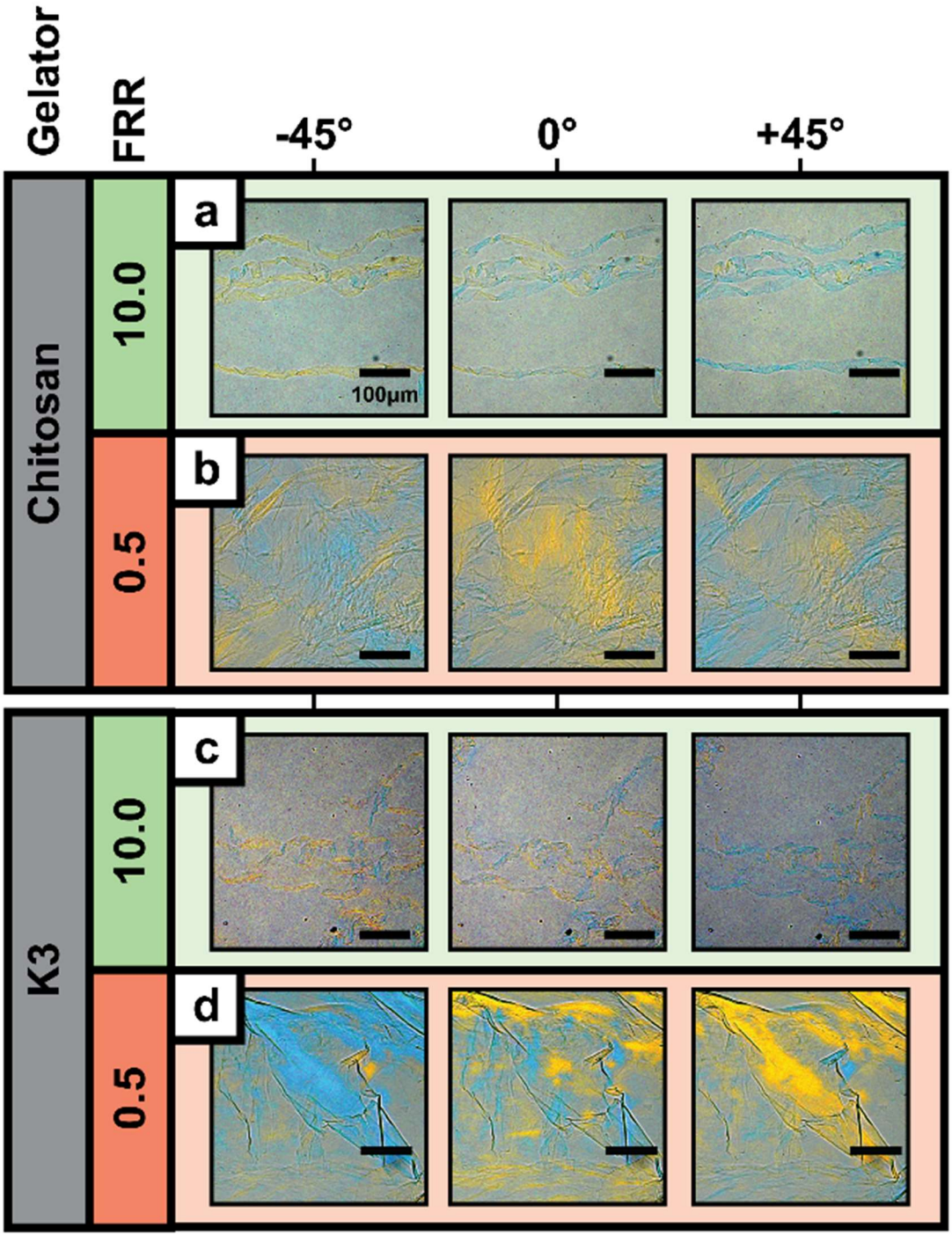

Figure 4.6: Polarized optical microscopy, images rotated to register relative to each other, retardation plate used with background white balanced, and contrast enhanced for visibility, of: (a) 0.5 wt% E3OH gelled with 0.05 wt% chitosan and extruded at FRR 10, (b) 0.5 wt% E3OH gelled with 0.05 wt% chitosan and extruded at FRR 0.5, (c) 0.5 wt% E3OH gelled with 0.5 wt% K3 and extruded at FRR 10, and (d) 0.5 wt% E3OH gelled with 0.5 wt% K3 and extruded at FRR 0.5.

We hypothesized that in addition to covalent polyelectrolytes, oppositely charged PA fibers could also be used as gelators. To investigate this hypothesis, we used an outer flow containing the positively charged PA K3, which forms nanofibers in aqueous solution at pH 5, and an inner flow of the negatively charged PA E3OH at pH 7. This fiber-fiber gelation is not as fast as the polyelectrolyte complexation achieved using chitosan, so similar to previous studies that demonstrated SB production with inorganic ions, we performed microfluidic gelation using a terminal serpentine to increase the residence time in the microfluidic device. We found, using this device, which is the same device design as used in Chapter 3, superbundles could be produced, provided that the proper processing conditions were used.

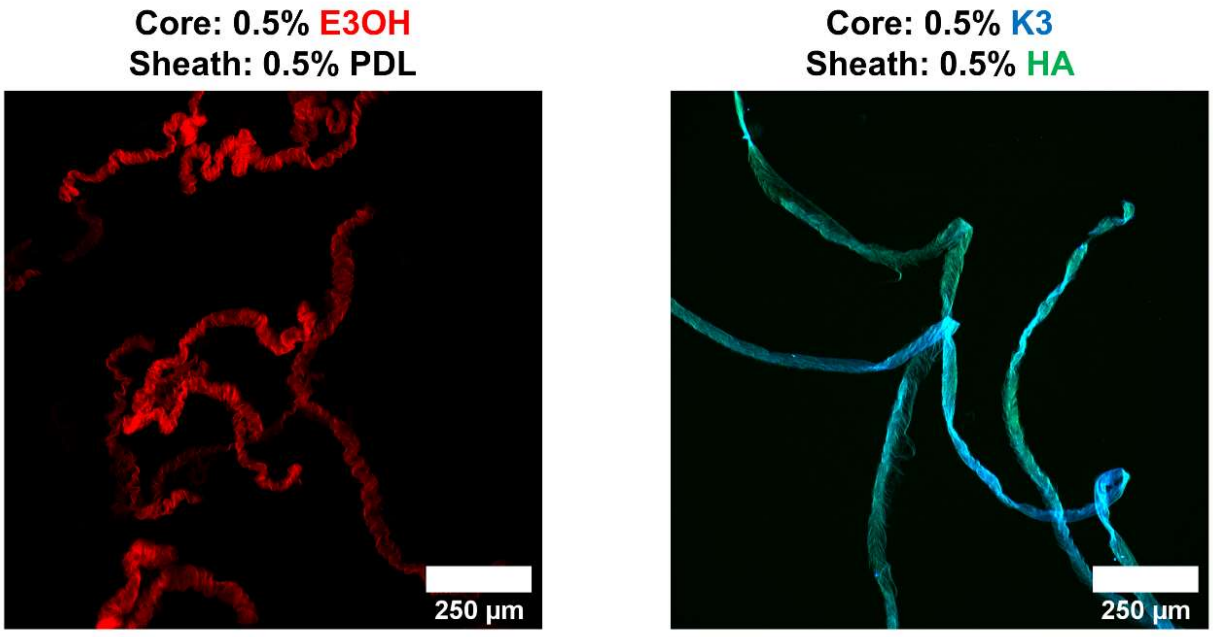

Figure 4.7: (left) Maximum intensity projection of a z-stack confocal micrograph of SBs produced using PDL as a gelator, E3OH PA channel in red. (right) Maximum intensity projection of a z-stack confocal micrograph of SBs produced using HA as a gelator, K3 PA channel in blue and HA channel in green.

To determine what concentration of K3 should be used in the outer flow, we performed experiments in which the concentration of K3 was varied, while the concentration of E3OH in the inner solution was held constant at 0.5 wt% and FRR 10 was used for gelation (Figure 4.8). We found that at 0.25 wt% K3 and above, superbundles could be reliably produced, so we used a concentration of 0.5 wt% K3 for all experiments used to produce the processing parameter diagram in Figure 4a. We once again varied the FRR of the solutions as well as the concentrations of the inner E3OH PA solution to determine which conditions would reliably produce SBs. At high FRRs, we found aligned SBs (Figure 4.9b, 4.9c, and 4.6); at low FRRs, we observed large aggregates (Figures 4.9d and 4.9e). This once again confirms the importance of flow focusing and the confinement of the inner PA flow by pinching with a gelator solution that conformally encompasses the inner PA stream within the microfluidic device. At low E3OH concentration, we observed disordered aggregates as well (Figure 4.4) because there is simply not enough PA nanofibers to form a cohesive network. In addition, we also found that the PA solutions could be switched such that K3 was the core solution and E3OH was the sheathing solution, while still forming superbundles (Figures 4.8 and 4.10), demonstrating the versatility of this approach.

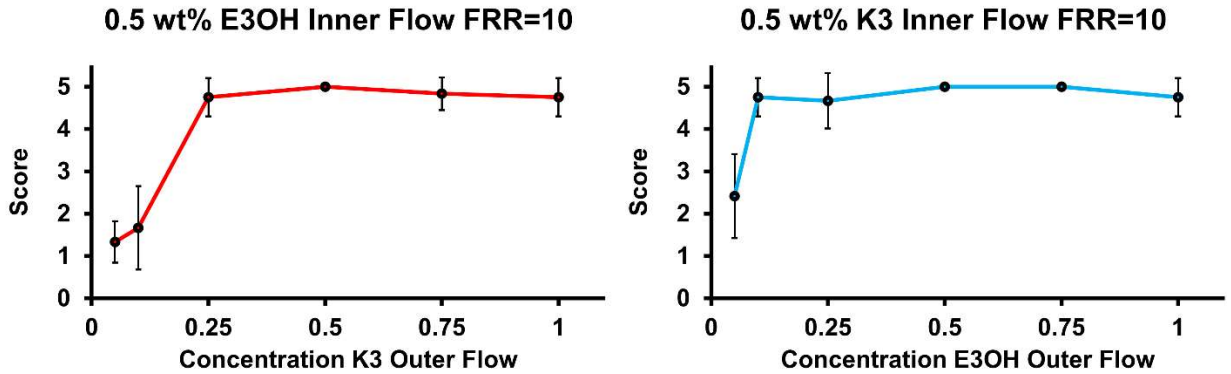

Figure 4.8: (left) Plot of superbundle scoring of gels prepared with a constant inner E3OH concentration of 0.5 wt% and a sheathing solution with varied K3 PA concentration. (right) Plot of superbundle scoring of gels prepared with a constant inner K3 concentration of 0.5 wt% and a sheathing solution with varied E3OH PA concentration.

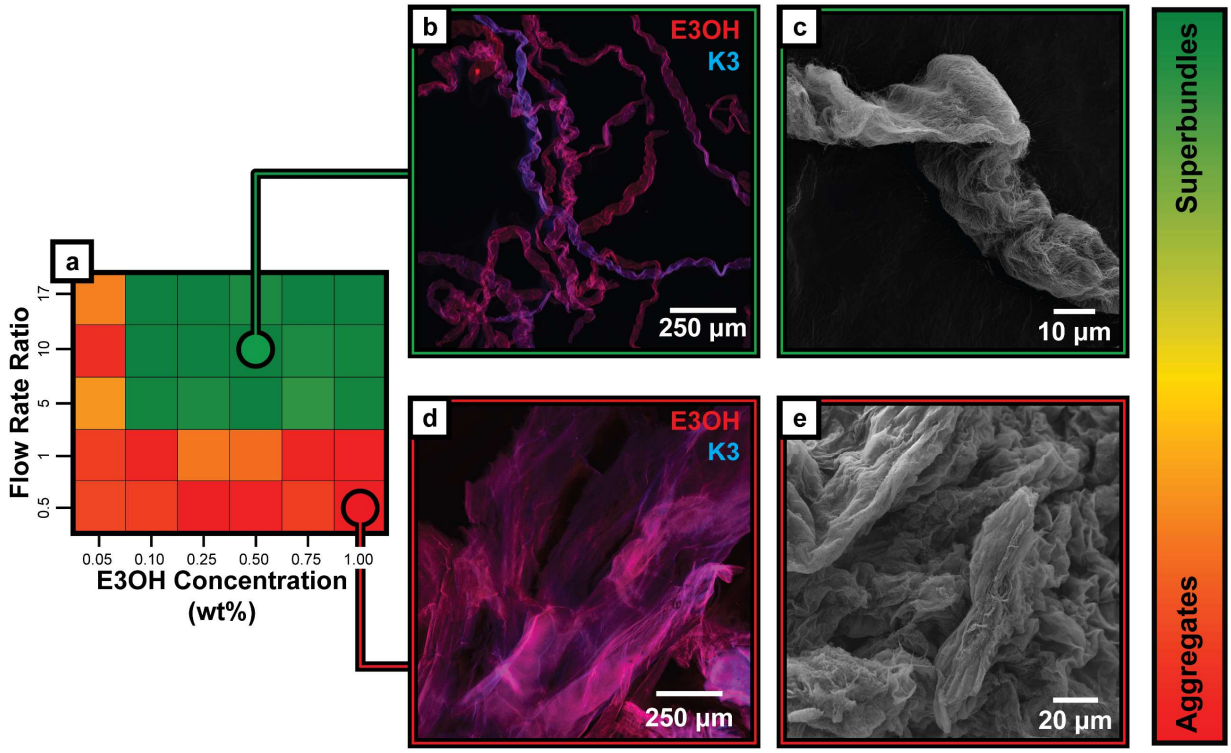

Figure 4.9: (a) Processing parameter diagram for E3OH solutions gelled with a 0.5 wt% solution of K3 nanofibers at varied FRRs and varied E3OH concentrations (green indicates SB formation, red indicates production of aggregate). (b) Maximum intensity projection of a confocal micrograph z-stack of SBs produced with K3 (blue) as a gelator and 0.5 wt% E3OH (red) at FRR 10. (c) SEM of an SB produced with K3 as a gelator and 0.5 wt% E3 at FRR 10. (d) Maximum intensity projection of a confocal micrograph z-stack of a gel produced with K3 (blue) as a gelator and 1.0 wt% E3OH (red) at FRR 0.5. (e) SEM of a gel produced with K3 as a gelator and 1.0 wt% E3OH at FRR 0.5.

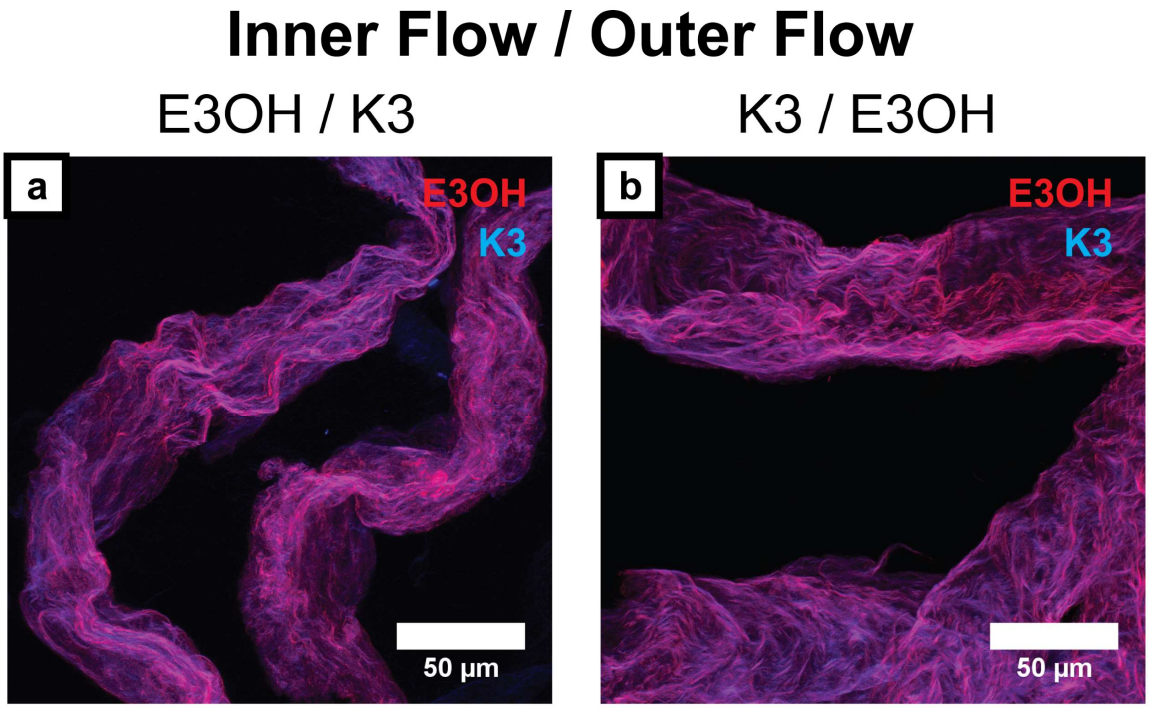

Figure 4.10: Maximum intensity projections of confocal microscopy z-stacks of: (a) 0.5 wt% E3OH (red) gelled with 0.5 wt% K3 (blue) extruded at FRR 10 and (b) 0.5 wt% K3 (blue) gelled with 0.5 wt% E3 (red) extruded at FRR 10.

Polyelectrolyte complexes formed with PAs are relevant for a wide variety of biomedical applications, and ability to formed peptide amphiphile polyelectrolyte complexes using PA-polymer complexation as well as PA-PA complexation widens their functional scope as well as material complexity. To conduct a careful examination of the morphological similarities and differences between E3OH-chitosan superbundles and E3OH-K3 superbundles, high magnification confocal laser scanning microscopy was performed. Each component was synthetically labelled with a different dye so that morphogical separation and interdiffusion could be identified. E3OH was coassembled with TAMRA-E3, chitosan was labelled with FITC, and K3 was coassembled with Cy5-K3.

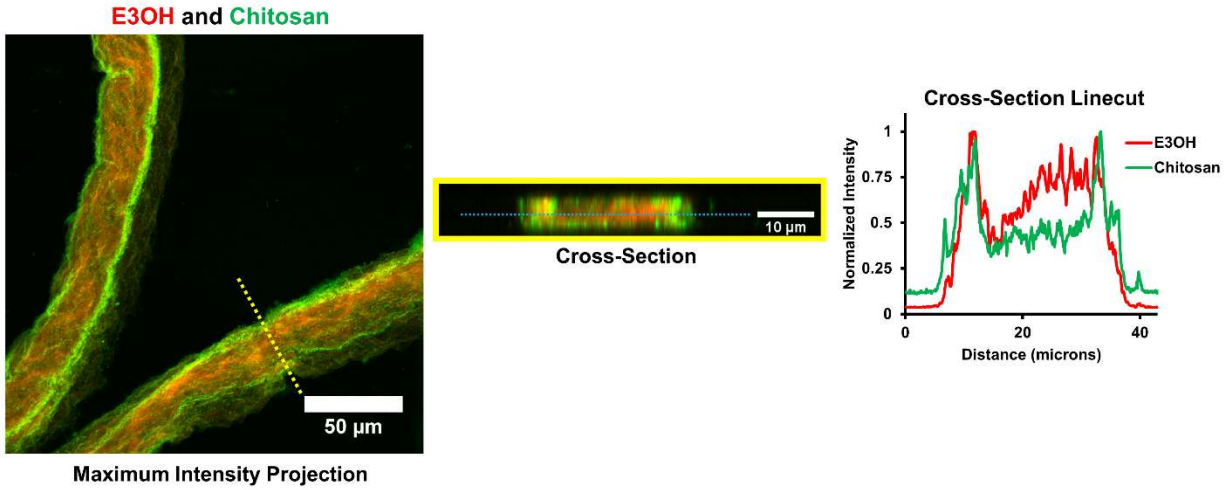

Figure 4.11: (a) confocal maximum intensity projection of E3OH (red) and chitosan (green) superbundle, yellow dashed line indicates area used for cross section image, (b) cross section image of superbundle from confocal microscopy z-stack, blue line indicates area where normalized intensity distribution was taken, and (c) normalized intensity distribution from confocal cross section of E3OH-chitosan superbundle.

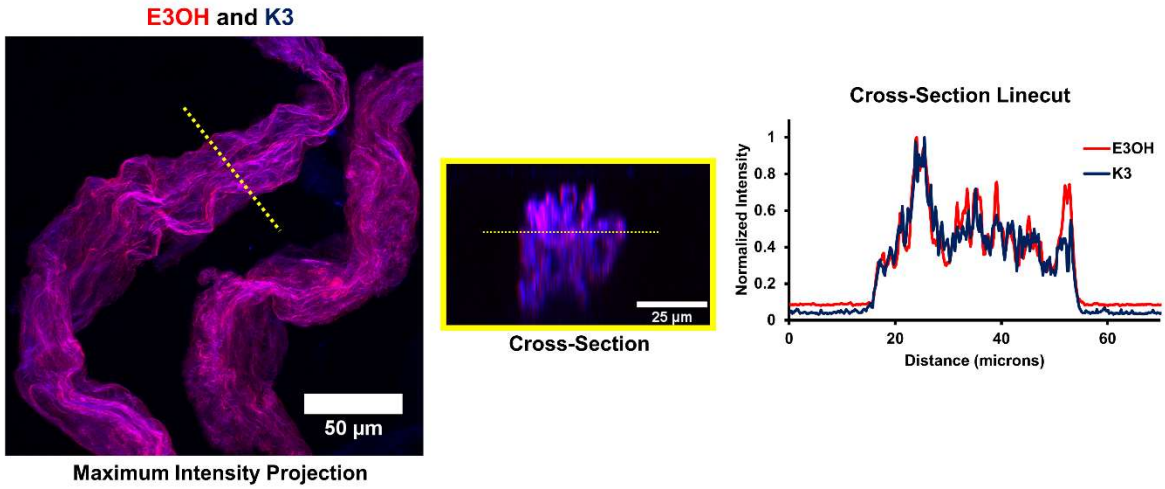

Figure 4.12: (a) confocal maximum intensity projection of E3OH (red) and K3 (blue) superbundle, yellow dashed line indicates area used for cross section image, (b) cross section image of superbundle from confocal microscopy z-stack, blue line indicates area where normalized intensity distribution was taken, and (c) normalized intensity distribution from confocal cross section of E3OH-K3 superbundle.

As can be seen in Figure 4.11, the PA (shown in red) is encased within the superbundle. The structure quite clearly has an inhomogeneous distribution of PA and chitosan due to the rapid formation of a contact layer between the PA and the chitosan. The outer layer of the superbundle is formed of a relatively high concentration of polymer and PA that have complexed together. This is the contact layer that has been shown previously in works made by gelling static solutions[61,179] of polymer and PA as well as work that involved rapidly mixing solutions together.[221] Evidently, there was diffusion of chitosan into the interior of the superbundle after the initial contact was formed, leading to a moderate internal concentration. Conversely, in Figure 4.12, we see that there is a homogeneous distribution of K3 and E3OH within the superbundle. Additionally, there is no evidence for the presence of a contact layer because the outerlayers do not have the characteristic high local relative concentration of the PAs.

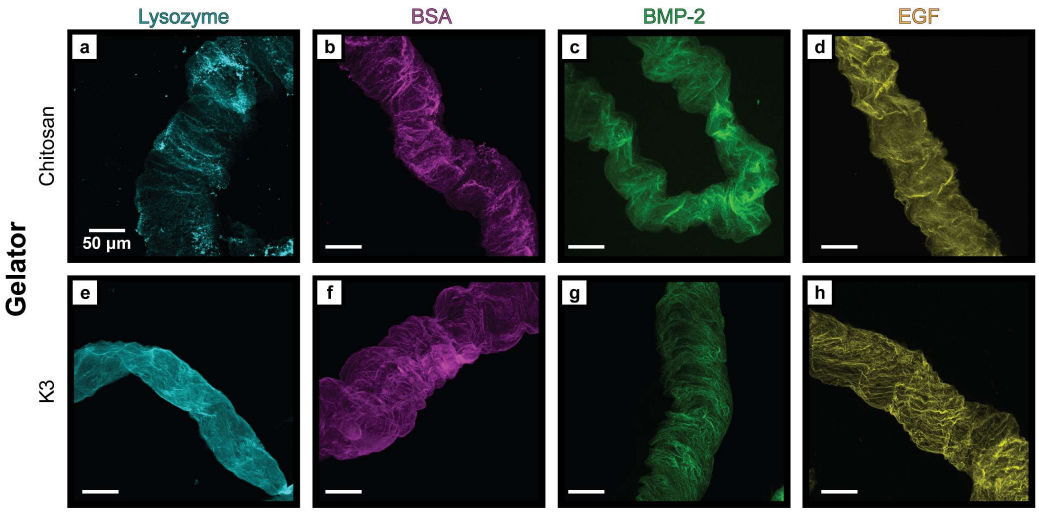

Figure 4.13: Maximum intensity projections of confocal microscopy z-stacks of (a) SBs produced using chitosan and E3OH with encapsulated lysozyme (cyan), (b) SBs produced using chitosan and E3 with encapsulated BSA (magenta), (c) SBs produced using chitosan and E3 with encapsulated BMP2 (green), (d) SBs produced using chitosan and E3 with encapsulated EGF (yellow), (e) SBs produced using K3 and E3OH with encapsulated lysozyme (cyan), (f) SBs produced using K3 and E3 with encapsulated BSA (magenta), (g) SBs produced using K3 and E3OH with encapsulated BMP2 (green), and (h) SBs produced using K3 and E3OH with encapsulated EGF (yellow).

Protein delivery has shown great promise in regenerative medicine and tissue engineering applications. The Stupp Laboratory has previously shown that PA-polymer complexes could encapsulate and deliver proteins in bulk gels[221] as well as planar membranes,[71] so we hypothesized that SBs formed from E3OH and chitosan would be able to encapsulate a variety of proteins. To demonstrate this, we encapsulated the model proteins lysozyme (isoelectric point ~11) and bovine serum albumin (BSA, isoelectric point ~5) as well as bone morphogenetic protein 2 (BMP-2, isoelectric point 8.5), a growth factor commonly used in osteo-regenerative medicine,[209] and epidermal growth factor (EGF, isoelectric point ~4.6), a growth factor proven in wound healing applications,[210] in E3OH-chitosan SBs. To perform this experiment, we dissolved fluorescently labeled proteins in preannealed solutions of E3 nanofibers, gelled the protein-PA solutions in a microfluidic device using chitosan and a FRR of 10, and performed imaging with confocal laser scanning microscopy. We observed that lysozyme (Figure 4.13a), BSA (Figure 4.13b), BMP-2 (Figure 4.13c), and EGF (Figure 4.13d) were all successfully encapsulated within E3OH-chitosan superbundles. We were also interested in whether proteins could be encapsulated when using a supramolecular polymer as a gelator, so we performed the same encapsulation experiments, with a solution of K3 nanofibers in devices that contained a serpentine. We found that these E3OH-K3 SBs were able to encapsulate the model proteins lysozyme (Figure 4.13e), BSA (Figure 4.13f), the growth factor BMP-2 (Figure 4.13g), as well as the growth factor EGF (Figure 4.13h). For both gelators, these systems contain both positively and negatively charged polymers. These positive and negatively charged motifs can form electrostatic interactions with oppositely charged regions that exist in each protein. In addition to electrostatic interactions, other noncovalent interactions such as hydrogen bonding can take place between the proteins and the superbundle scaffolds. For

chitosan-E3OH superbundles, contact layer formation can lead to the localization of proteins in the dense outer region of the gel unless other PA-protein or polymer-protein interactions dominate. The ability to encapsulate proteins using both the covalent polymer chitosan and supramolecular polymer K3 demonstrate their potential for use in tissue engineering and regenerative medicine.

4.3 Conclusion

Here, we have shown that complexation of supramolecular nanofibers in a flow focusing microfluidic device can yield biomimetic superstructures. We demonstrated the importance of the supramolecular polymer's morphology, the concentration of the supramolecular polymer, as well as the relative flow rates of the core and sheathing solution. Additionally, we exhibited the breadth of materials that could be produced by using both covalent and supramolecular polymer gelators. We also found that both positively and negatively charged proteins could be encapsulated within superbundles. Due to their versatile network chemistry and ability to encapsulate a variety of proteins, superbundles formed via complexation of peptide amphiphile nanofibers with oppositely charged polymers are promising materials for tissue scaffolding and protein delivery.

4.4 Materials and Methods

Silicon Master Mold Fabrication: AZ P4620 (coated at 2000 rpm) was spun onto silicon wafers (University Wafers) before baking the wafers at 110 °C for 60 seconds. The microfluidic device was designed in Autodesk AutoCAD, and the design used in this work is identical to that reported in previous work from our laboratory as seen in Chapter 3.

Using a maskless aligner (Heidelberg MLA150), the microfludic design was patterned onto the AZ P4620 coated silicon wafers with a total exposure value of 600 mJ/cm^2. Wafers were developed

in AZ 400K 1:4 for 90 seconds before being washed with deionized water and dried with nitrogen gas. Using a deep reactive ion etcher (STS LpX Pegasus), the patterned silicon wafers were etched to a depth of 85µm. Photoresist was stripped from the wafers, and optical profilometry (Zygo nexview) was used to confirm proper design transfer. A non-adhesive monolayer was formed on these etched wafers by placing them in a vacuum chamber with trichloro(1H,1H,2H,2H-perfluorooctyl)silane (Sigma-Aldrich) for 30 minutes.

Soft Lithography: Sylgard 184 elastomer base (Dow Chemical) and Sylgard 184 curing agent were thoroughly mixed in a 10:1 weight ratio and degassed for 1 hour in a vacuum chamber. A wafer etched with a microfluidic device design was placed into an aluminum foil boat on a cool hotplate. The Sylgard mixture was added to the boat and heated to (70 °C) for 1 hour. The silicon wafer and Sylgard were allowed to cool to room temperature ambiently. Once cool, the cured polydimethylsiloxane (PDMS) polymer cast was demolded and divided into individual devices as needed. Fluidic access ports were punched using a 0.5 mm Rapid-Core sampling tool (Electron Microscopy Sciences). The exit port was punched using an 8.00 mm biopsy punch (Harris Uni-Core). For K3 based gelations, the exit port was punched after the terminal serpentine; for chitosan based gelations, the exit port was punched before the terminal serpentine. The bottom layer of the finished microfluidic devices consisted of a sheet of flexible PCR tape (ThermalSeal RTS Sealing Film).

Extrusion protocol: Extrusion experiments were performed using an Elveflow pressure control system (Elveflow OB3+ pressure regulator and Elveflow MFS3 flow sensor). Annealed PA and gelator solutions were directed through mass flow sensors (MFSs) and into the appropriate microfluidic entry port using tygon tubing (inner diameter 0.020 inches, outer diameter 0.060

inches; Cole Parmer catalog #SK-06419-01) and metal nipples (inner diameter 0.017 inches, outer diameter 0.025 inches, and length 0.500 inches; New England Small Tube catalog #NE-1300-01). The flow rate ratio was controlled using the Elveflow Smart Interface Software.

Confocal microscopy: Samples of microfluidic extrudate were mounted on a glass slide and imaged using a Nikon A1R Confocal Microscope. The 488 nm laser was used for imaging FITC-chitosan and Alexa Fluor 488-BMP2. The 561 nm laser was used for imaging TAMRA-E3. The 640 nm laser was used for imaging Alexa Fluor 647-labeled BSA (Invitrogen), Alexa Fluor 647-labeled lysozyme, and Cy5-K3.

Scanning electron microscopy: Microporous specimen capsules (70 μm, Electron Microscopy Sciences) were perforated with a needle and wetted with water under vacuum for 30 minutes. Microfluidic extrudate was lightly sedimented using a benchtop centrifuge. The supernatant was removed, and the sedimented sample was placed into the perforated, pre-wetted microporous specimen capsules. These sample-containing capsules were solvent exchanged into 100% ethanol by serial incubation in increasing ethanol concentrations (30%, 40%, 50%, 60%, 70%, 80%, 85%, 90%, 95%, 100%) for 30 minutes per solution. Ethanol exchanged samples were critical point dried (Tousimis Samdri). The dried samples were mounted on aluminum sample stubs coated with conductive carbon tape (EMS Microscopy Sciences). Mounted samples were coated with 16nm of Osmium (Filgen Osmium Plasma Coater OPC60A) before imaging on a JEOL 7900 FLV SEM with an accelerating voltage of 5kV.

Morphology Scoring: Confocal images of microfluidic effluent were assigned morphology scores by blinded review by a panel of independent reviewers. Three representative images of each

extrudate were standardized for brightness and contrast in imageJ before distribution to panelists for scoring using the following scale:

1 - no evidence of ribbons – only aggregates

2 - mostly aggregates, some ribbons

3 - equal amounts of ribbons and aggregates

4 - mostly ribbons, some aggregates

5 - only ribbons – no aggregates

Each scorer rated three images of each extrusion condition to provide n=3. The average scores of each individual panelist were then averaged with, at minimum, two additional scorers to provide $n \geq 9$ for the scoring of each extrusion condition. Statistical data for each scoring condition may be found in Figure 4.14.

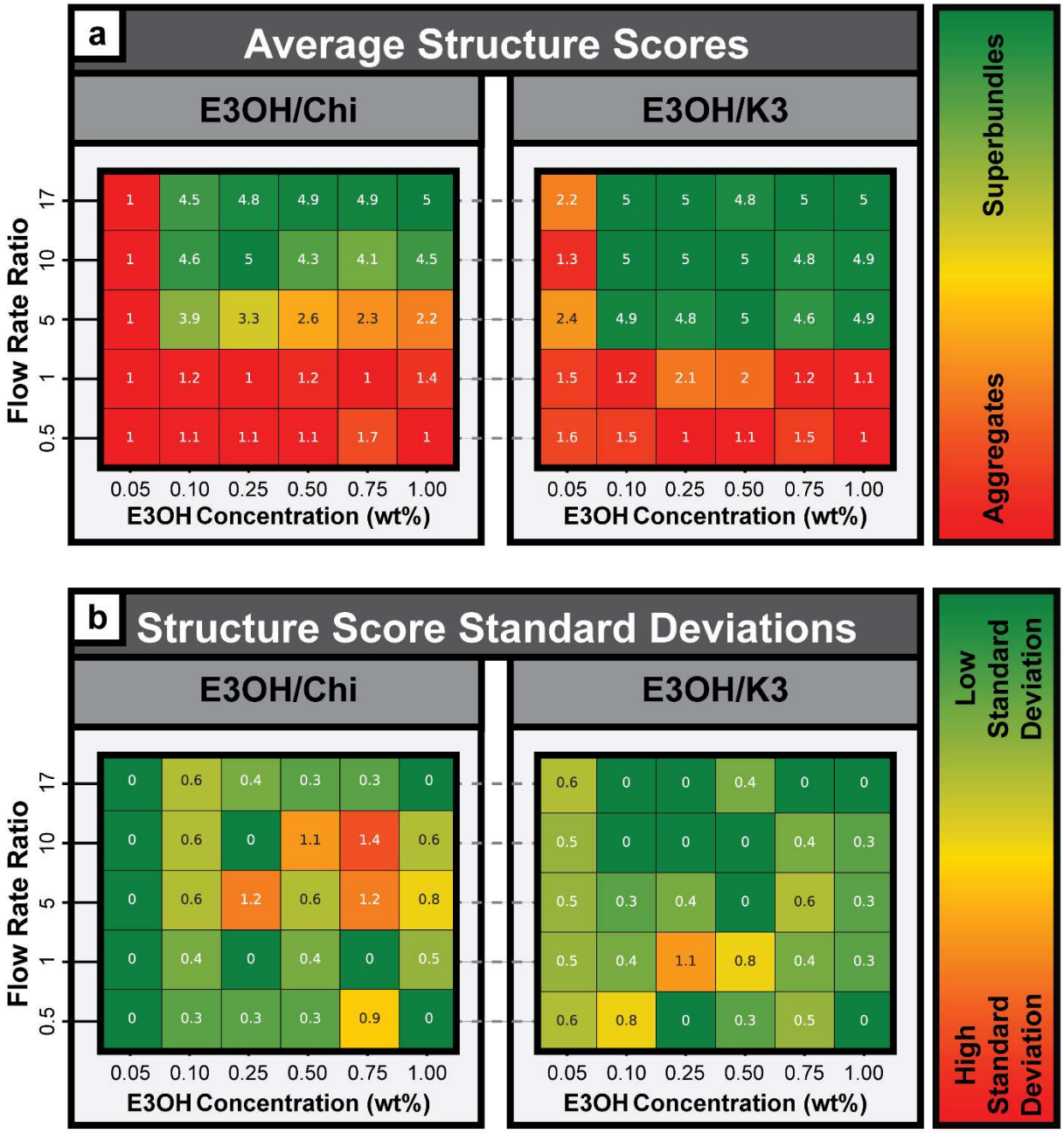

Figure 4.14: (a) Averaged morphology scores for each condition shown in the processing parameter diagrams of Figure 3. (b) Population standard deviations for morphology scores for each condition.

Peptide Synthesis: All peptide amphiphiles (PAs) were synthesized using 9-fluorenyl methoxycarbonyl (Fmoc) solid-phase peptide chemistry in a CEM L.iberty Blue automated microwave peptide synthesizer. C16VVVAAAEEE-TAMRA (TAMRA-E3), C16-VVVAAAKKK (K3), and C16-VVVAAAKKK-K(Cyanine5) (Cy5-K3) were synthesized on Rink amide MBHA resin . C16-VVVAAAEEE-OH (E3) and C16-EEE-OH were synthesized using pre-loaded Fmoc-Glu(OtBu) Wang resin. Automated coupling reactions were performed using 4 eq. Fmoc-protected amino acid or palmitic acid (C16), 4 eq. of *N*,*N'*-diisopropylcarbodiimide (DIC), and 8 eq. ethyl(hydroxyimino)cyanoacetate (Oxyma pure). Removal of the Fmoc groups was achieved with 20% 4-methylpiperidine in DMF. Peptides were cleaved from the resin using standard solutions of 95% TFA, 2.5% water, 2.5% triisopropylsilane (TIS) for 3 h, precipitated with cold ether, and then purified by reverse-phase HPLC on a Waters Prep150 or Shimadzu Prominence HPLC using a water/acetonitrile (each containing 0.1% TFA v/v) gradient. Eluting fractions containing the desired peptide were confirmed by mass spectrometry using an Agilent 6520 QTOF LCMS. Confirmed fractions were pooled and the acetonitrile was removed by rotary evaporation before freezing and lyophilization. Purity of lyophilized products was tested by LCMS.

For the 5-carboxytetramethylrhodamine (TAMRA) labeled PA, N-α-Fmoc-N-ε-4-methyltrityl-L-lysine (lysine(Mtt)) was used as the C-terminal residue. After automated synthesis of the full sequence, the methytrityl (Mtt) protecting group was removed from the lysine while still on resin using 3% TFA in DCM with 5% TIS (2 x 10 min additions). After washing with DCM and DMF, TAMRA was then coupled to the now free ε-amine of lysine using 1.2 eq. of TAMRA, 1.2 equivalents of PyBOP, and 8 eq. of DIEA for approximately 18 h.

For the Cyanine5 (3H- Indolium, 2- [5- [1- (5- carboxypentyl) - 1, 3- dihydro- 3, 3- dimethyl- 2H- indol- 2- ylidene] - 1, 3- pentadien- 1- yl] - 1, 3, 3- trimethyl- , chloride) labeled PA, N-α-Fmoc-N-ε-1-(4,4-dimethyl-2,6-dioxocyclohex-1-ylidene)-3-methylbutyl-L-lysine (lysine(ivDde)) was used as the C-terminal residue (others lysines Boc protected on the ε-amine). After automated synthesis of the full sequence, the ivDde protecting group was selectively removed from this C-terminal lysine while still on resin using 5% v/v hydrazine in DMF (2 x 20 min additions). The resin was then washed with DCM and DMF, and Cyanine5 carboxylic acid was coupled to the now free ε-amine of the C-terminal lysine using 1.2 eq. of the dye, 1.2 eq. of PyBOP (benzotriazol-1-yl-oxytripyrrolidinophosphonium hexafluorophosphate), and 8 eq. of *N*,*N*-diisopropylethylamine (DIEA) for approximately 18 h.

PA structures may used in Chapter 4 may be found in Table 4.1.

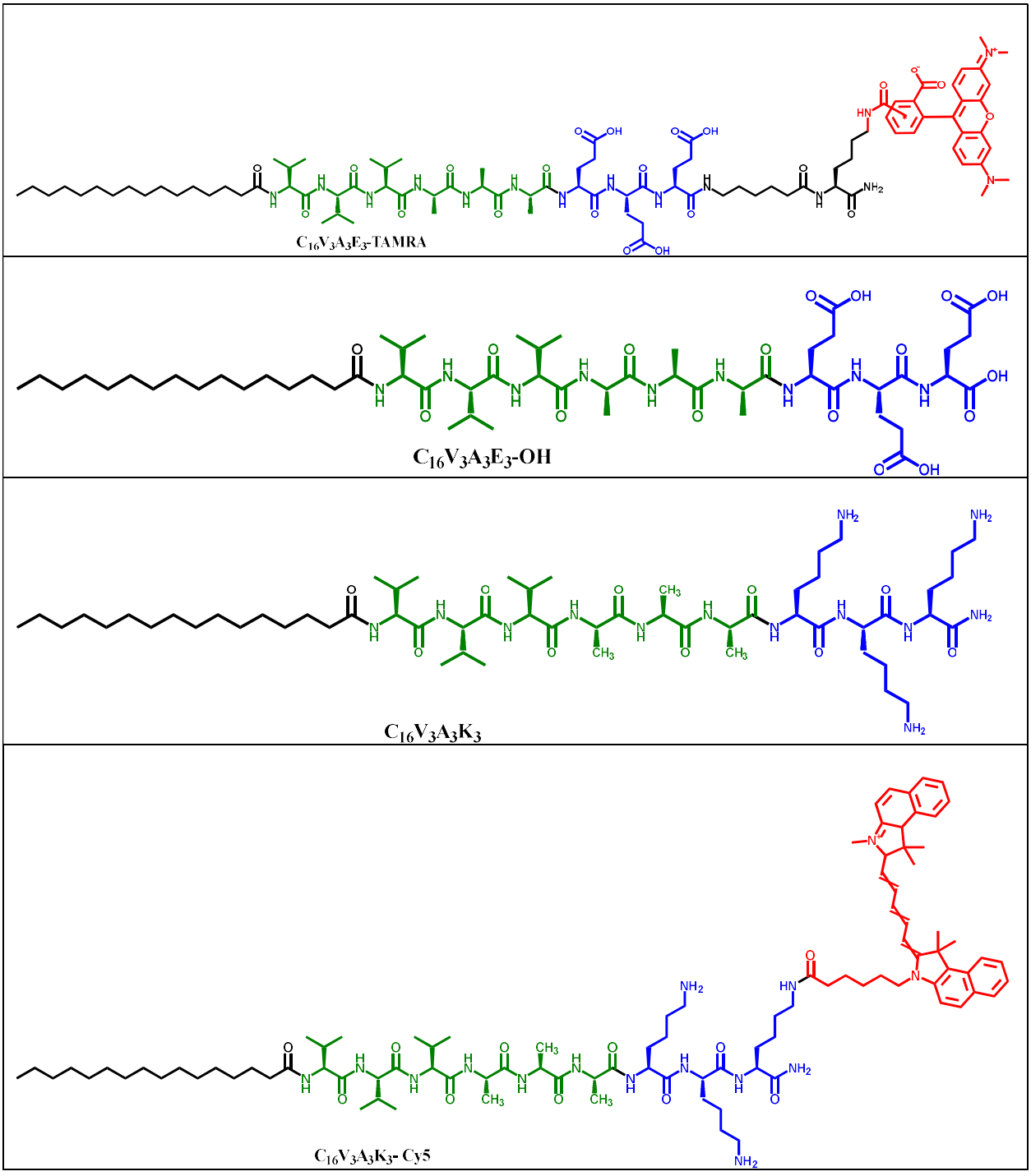

Table 4.1: PA structures

E3OH solutions: deionized water was added to freeze dried PA powder. The resulting solution was adjusted to pH 7 using 1 M NaOH and then sonicated. Solutions were then placed in an 80 °C water bath for 30 minutes and then cooled slowly down to room temperature.

K3 solutions: deionized water was added to freeze dried PA powder. The resulting solutions were placed in an 80 °C water bath for 30 minutes and cooled slowly down to room temperature.

Cy5-K3/K3 co-assemblies: a 0.1 wt% solution of Cy5-K3 dissolved in deionized water was mixed with an unannealed solution of K3 dissolved in deionized water. The produced a co-assembly with 0.1 mol% Cy5-K3 in 99.9 mol% K3. These mixtures were sonicated. Solutions were placed in an 80 °C water bath for 30 minutes and cooled slowly down to room temperature.

TAMRA-E3/E3 co-assemblies: TAMRA-E3 was dissolved in deionized water to a concentration of 0.1 wt% and mixed with an unannealed solution of E3. The ratio of TAMRA-E3 solution to E3 solution was calculated so that TAMRA-E3 was 0.1 mol% of the total amount of PA in solution. The mixtures were sonicated and placed in an 80 °C water bath for 30 minutes before slowly cooling to room temperature.

Chitosan: chitosan (medium molecular weight, 190,000-310,000 Da; Sigma-Aldrich catalog #448877) was dissolved in 2 vol% acetic acid. All remaining solids were filtered out, and the solution was dialyzed against deionized water in 12-14 kDa Mw cutoff Spectra/Por tubing and then lyophilized.

Chitosan solutions: 2 wt% aqueous chitosan solutions were prepared by dissolving the previously filtered and freeze-dried chitosan in 2 vol% acetic acid. Solutions were then diluted to 1 wt%

chitosan with a 500 mmol sodium acetate solution. This 1 wt% solution was then diluted to 0.05% using a 1 vol% acetic acid – 250 mM sodium acetate buffer solution.

FITC-labeled chitosan: chitosan (filtered and lyophilized) was dissolved in 2 vol% acetic acid to reach 2 wt% chitosan, and then methanol was added until to dilute the solution to 1 wt%. The chitosan solution was stirred, and a 2 mg/mL fluorescein isothiocyanate (FITC) solution in methanol was added to achieve a final volume ratio of chitosan solution to FITC solution of 2:1. The solution was then stirred for 4 hours. Afterwards, a 1 M NaOH solution was added to precipitate the chitosan. The precipitate was then washed with a 30% methanol in water solution and collected using vacuum filtration. After redissolution in 1 vol% acetic acid, the solution was dialyzed against deionized water in Spectra/Por 12-14 kD Mw cutoff tubing and then lyophilized.

FITC-chitosan solutions: 2 wt% aqueous FITC-chitosan solutions were prepared by dissolving filtered and freeze dried FITC-chitosan in 2 vol% acetic acid. Solutions were then diluted to 1 wt% FITC-chitosan with a 500 mmol sodium acetate solution. The 1 wt% FITC-chitosan was mixed with a 1 wt% chitosan solution at a ratio of 1:10 to reduce the concentration of FITC dye. This 1 wt% solution was then diluted to 0.05% using a 1 vol% acetic acid – 250 mM sodium acetate buffer solution.

Fluoresceinamine-labeled sodium hyaluronate: sodium hyaluronate (100,000 Da, Lifecore Biomedical) was dissolved at 1 wt% in phosphate buffered saline solution. While the sodium hyaluronate solution was stirring, 3-(3-Dimethylaminopropyl)-1-ethyl-carbodiimide hydrochloride (Chem Impex) was added such that the final concentration is 5 mM. Fluoresceinamine isomer 1 (Sigma-Aldrich) was then added such that the final concentration was

1.5 mM. The mixture was briefly sonicated to ensure adequate dissolution and mixing. Afterwards, the solution was stirred at room temperature and allowed to react for 24 hours. The solution was then dialyzed in deionized water for 72 hours in Spectra/Por 3.5 kDa Mw cutoff dialysis tubing and then lyophilized and stored at -20 °C.

Fluoresceinamine-labeled sodium hyaluronate solutions: 0.5 wt% aqueous solutions of fluoresceinamine-labeled sodium hyaluronate were prepared by dissolving the freeze-dried solid in deionized water. Microfludic devices with serpentines were used when gelling K3 with HA.

Polymer structures used in Chapter 4 may be found in Chapter 4.2

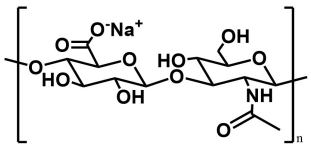

Sodium Hyaluronate

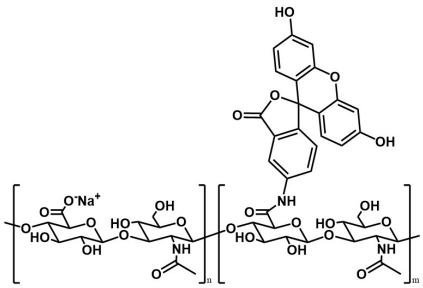

Fluoreceinamine-Sodium Hyaluronate

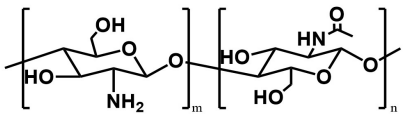

Chitosan

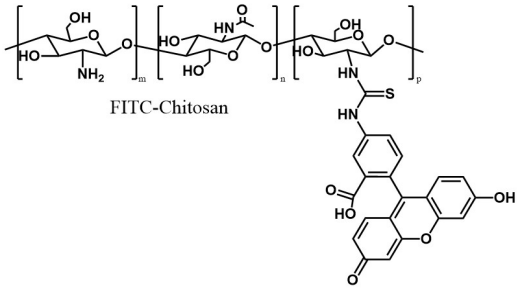

FITC-Chitosan

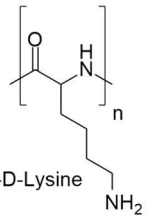

Poly-D-Lysine

Table 4.2: Polymer Structures

Alexa Fluor 647-labeled lysozyme: Chicken egg white lysozyme (Sigma Aldrich) was dissolved in 0.1 M aqueous sodium bicarbonate to achieve a concentration of 10 mg/mL. Alexa Fluor 647 carboxylic acid succinimidyl ester (1 mg, Thermo-Fisher) was dissolved in 100 µL of dimethylformamide and added to a stirring solution of lysozyme at room temperature. The reaction was terminated after one hour by adding 200 µL of a 1 M hydroxylamine aqueous solution (pH 8). After termination, the solution was stirred for an additional hour. The resulting Alexa Fluor 647-Lysozyme was purified by dialysis against deionized water for 48 hours using Spectra/Por 3.5 kDa Mw cutoff dialysis tubing before lyophilization and storage at -20 °C.

BMP-2 labeling: Human recombinant Bone Morphogenetic Protein 2 (BMP-2, Biomatik Corporation) and labeled with Alexa Fluor 488 Microscale Protein Labeling Kit (Molecular Probes). Prior to labeling, BMP2 was dialyzed in cold MilliQ water using TUBE-O-DIALYZER mini dialysis system, micro, 4 kDa molecular weight cutoff (G-Biosciences) for 8 hr to remove sodium azide. 50 µg of BMP-2 (MW 43 kDa) was dissolved in 50 µL of MilliQ water. 5 µL of 1 M sodium bicarbonate and 7 µL of Alexa Fluor 488 tetrafluorophenyl (TFP) ester reactive dye stock solution were added to the protein solution and incubated at room temperature for 15 minutes. The dye-labeled protein conjugate was purified with a prepared spin filter with 800 µL of gel resin provided in the kit at 16,000 x g for 1 min. The final concentration of the purified dye-labeled BMP-2 was measured with Thermo Scientific NanoDrop ND-1000 spectrophotometer.

EGF Labeling: Recombinant human epidermal growth factor (EGF) protein was purchased from R&D Systems as a lyophilized powder and reconstituted at 10 mg/mL in sterile PBS. EGF was then fluorescently labelled with Alexa Fluor 647 NHS ester (Thermo Fisher Scientific). Briefly, 1 M $NaHCO_3$ solution was added to such that the solution was pH 8.3. Then, 10 µL of NHS ester

dye dissolved in DMSO at 10 mg/mL was added to the reaction mixture and incubated for 2 hours at room temperature. To quench the reaction, 10 μL of 1.5 M hydroxylamine hydrochloride was added, and the mixture was incubated for 1 hour. The reaction mixture was transferred to TUBE-O-DIALYZER mini dialysis system (micro, 4 kDa molecular weight cutoff, G-Biosciences), and dialyzed for 120 hours in PBS to remove excess dye. The concentration of the purified dye-labeled EGF was measured with Thermo Scientific NanoDrop ND-1000 spectrophotometer.

Encapsulation of Protein in Superbundles: Alexa Fluor 647-labeled lysozyme or Alexa Fluor 647-labeled BSA (Invitrogen) was dissolved to 0.25 mg/mL in a 0.5 wt% pre-annealed PA solution at room temperature. Alexa Fluor 488-labeled BMP2 was dissolved in PBS at 0.28 mg/mL, then mixed with a pre-annealed PA solution at room temperature to achieve a final concentration of 0.07 mg/mL. The solutions were gelled the microfluidic device with various gelators using FRR 10 to form SBs. PA concentrations for all encapsulation experiments were 0.5 wt%.

Polarized Optical Microscopy: solutions containing microfluidic extrudate were pipetted onto a glass slide, and then covered with cover glass. A Nikon Eclipse LV100N Polarized Optical Light Microscope was used for imaging. When images were taken with the first order, full wavelength retardation plate, the fields of view were auto white balanced against background using Nikon NIS Elements software to improve the ease of the visualization of alignment. Images were for visibility in print media.

CHAPTER 5: Summary and Future Outlook

The work presented in this thesis describes the development of hierarchical materials using supramolecular and covalent polymers. Using biological systems as inspiration, novel biomimetic materials were produced through the gelation of peptide amphiphiles during flow, yielding new morphologies. The chemical versatility of the materials synthesis demonstrated in these studies allude to the potential breadth of application. The findings presented in this thesis provide a foundation for future development of rationally designed soft materials for biomedical applications.

5.1 Bulk Interfacial Complexation of Oppositely Charged Supramolecular Polymers and Polyelectrolytes

The studies on PA-polymer gels shown in Chapter 2 demonstrated the ability to make bulk materials through the interfacial complexation of oppositely charged peptide amphiphiles and covalent polymers. This interfacial complexation locked in the structure formed during mixing, leading to a sheet-like gel morphology composed of nonequilibrium structures with distinct domains. These bulk gels had rheological properties that could be easily tuned by changing the PA concentration as well as the volumetric ratio of the PA and polymer solutions. We found that we could easily encapsulate both positively and negatively charged proteins and localize them in the outermost layer of the gel. Because these gels were made with biocompatible materials, have tunable mechanical properties, as well as the ability to encapsulate proteins, these gels have potential in numerous biomedical applications.

From a processing perspective, the rapid and chaotic mixing that is used to create the bulk gels during interfacial complexation is crucial to create the interconnected sheet-like structure, but it also leads to significant challenges in controlling material properties and structure. By its very nature, the turbulent mixing employed in chapter 2 is unpredictable, and theoretically, no two gels' microstructure is perfectly identical. The mixing methodology also results in a heterogenous orientation of the sheets relative to each other as well heterogenous dimensions of the sheets, even within a single gel and even within a single sheet. This presents challenges for drug delivery as well as controlling structure property relationships. Additionally, all of the gels that were produced had PA predominantly in the middle of the sheets encapsulated by an outer polymer rich layer. While this helped encapsulate and retain protein, it means that if future researchers want to include a PA that presents an epitope, the epitope will likely not be exposed (at least in large part) until degradation of much of the gel occurs.

Despite the aforementioned challenges, there are a myriad of future directions for this class of materials. There are nearly infinite combinations of PA polymer pairs that could be employed. This means that for each desired application, a PA could be designed synthesized, and a polymer could be chosen for complexation. While there have been numerous biological studies on PA-polymer complexes in other systems, cell studies using hybrid bulk interfacial PA-polymer complexes remain unexplored. Most PA-polymer complexation has been done with bioderived polymers such as hyaluronic acid or chitosan, but new complexes and gels could be produced using a wide range of polymer chemistries that would allow for increased functionality. In addition to bioactive epitopes being included on PAs, bioactive functional groups could be synthetically liked to the polymer chains themselves. Additionally future work could investigate the ability to

encapsulate small molecule drugs in these gels in addition to proteins. In addition to including new chemistries and bioactive functionality, further studies could also seek to improve on the level of control over mixing between the PA and polymer components; this challenge in particular was the inspiration for the work performed in Chapter 4.

5.2 Extracellular Matrix Mimetic Scaffolds by Microfluidic Superstructuring of Nanofibers

In Chapter 3, we developed a microfluidic system to continuously extrude extracellular matrix mimetic supramolecular hydrogels. We demonstrated the ability to use both positively and negatively charged PAs to make these "superbundles" and also showed that a variety of inorganic multivalent salts could be used for gelation. Despite the wide variety of potential salts that can be used, biomedical applications would require the use of biofriendly ions such as Ca^{2+}. By exploring a processing parameter space with varying flow rates and PA concentration, we developed general design rules to create superbundles; high flow rate ratios and high PA concentrations are necessary to form cohesive gels. Additionally, we demonstrated that model proteins and growth factors could be encapsulated within these superbundles.

While the device design used in Chapter 3 was laudable for its simplicity, it could be improved. Efforts to streamline device fabrication enormously increased productivity, but experimentally, device clogging presented a challenge to reliably produce these structures. A device design that addresses this concern would greatly improve the ease of use and reproducibility of superbundle experiments. Additionally, as stated this device is among the simplest that can be designed; it has only two inlet streams that meet at a cross-junction. Other device designs that include multiple PA inlet streams could be used to make morphologies with increasing complexity

including multi-core structures or Janus microbundles. These new structures would lend themselves greatly to biological studies that seed to expose cells to multiple bioactive signals concurrently or at different times. The generality of the microfluidic gelation approach also means that numerous peptide amphiphiles with a diverse array of epitopes could be used to form structures that mimic the extracellular matrix. Indeed, presumably nearly any tissue could be the target of this biomaterials approach.

5.3 Microfluidic Superstructuring of Biomaterials Based on Covalent and Supramolecular Polymers

The work shown in Chapter 4 builds off of the findings made in Chapters 2 and 3 by using controlled laminar flow within a microfluidic device during the complexation of peptide amphiphiles with covalent polymers as well as another peptide amphiphile in order to produce extracellular matrix mimetic superbundles. We demonstrated that this approach works for both positively and negatively charged peptide amphiphile nanofibers and showed that nanofiber morphology is crucial to the production of superbundles, as aggregates are produced when using micellular structures instead of microfiber gels. Additionally, we found that multiple different PA-polymer pairs could be used for this approach, and indeed, positively and negatively charged peptide amphiphiles could be complexed together to form superbundles as well. By exploring a processing parameter space with varying flow rates and PA concentration, we found that the design rules developed Chapter 3 were applicable to systems with different gelator systems including multivalent inorganic salts, covalent polymer gelators, and supramolecular polymer gelators. The ability to encapsulate several model proteins and growth factors in these superbundles, paired with

their remarkably biomimetic structure, we demonstrated the potential usefulness of these materials in biomedical applications.

The device designs used in Chapter 4 were very similar, or in cases the same, to those used in Chapter 3, with only minor alterations made such as the removal of a serpentine depending on the gelator. More complex devices that include multiple PA streams could be used to make more advanced material morphologies ranging from multi-core structures to janus structures, and of course many other potential designs are possible. Additionally, the superbundles presented in this thesis are ribbon like in their dimensions because they were made using a planar device with a cross-junction. If desired, these findings could be extended to concentric flow geometries resulting in cylindrical superbundles. Further advances in the production of functional materials could be made through the use of more advanced polymer synthesis. The linear covalent polymers used in these studies were bioderived and not synthesized in house. There are nearly infinite potential polymers that could be made with a variety of chemistries and topologies that could be tailored to the specific desired application. These polymers could be functionalized with numerous functional groups such as bioactive moieties. Similarly, there is a plethora of peptide amphiphile sequences, as well as other supramolecular nanofibers, that could be used as the core flow. These peptide amphiphile sequences could be specifically chosen, along with relevant bioactive epitopes, for each particular bioapplication. Additionally, other proteins could be encapsulated in these scaffolds, further enhancing their relevance for biomedical applications and regenerative medicine.

References

(1) Staudinger, H. Über Polymerisation. *Berichte der deutschen chemischen Gesellschaft (A and B Series)* **1920**, *53* (6), 1073–1085. https://doi.org/10.1002/cber.19200530627.

(2) Lau, G. C.; Sather, N. A.; Sai, H.; Waring, E. M.; Deiss-Yehiely, E.; Barreda, L.; Beeman, E. A.; Palmer, L. C.; Stupp, S. I. Oriented Multiwalled Organic–Co(OH)2 Nanotubes for Energy Storage. *Advanced Functional Materials* **2018**, *28* (3), 1–10. https://doi.org/10.1002/adfm.201702320.

(3) Dumele, O.; Chen, J.; Passarelli, J. V.; Stupp, S. I. Supramolecular Energy Materials. *Advanced Materials* **2020**, *1907247*, 1–32. https://doi.org/10.1002/adma.201907247.

(4) Matson, J. B.; Stupp, S. I. Self-Assembling Peptide Scaffolds for Regenerative Medicine. *Chem. Commun.* **2012**, *48*, 26–33. https://doi.org/10.1039/c1cc15551b.

(5) Sato, K.; Hendricks, M. P.; Palmer, L. C.; Stupp, S. I. Peptide Supramolecular Materials for Therapeutics. *Chemical Society Reviews* **2018**, *47*, 7539–7551. https://doi.org/10.1039/c7cs00735c.

(6) Stupp, S. I.; Palmer, L. C. Supramolecular Chemistry and Self-Assembly in Organic Materials Design. *Chemistry of Materials* **2014**, *26* (1), 507–518. https://doi.org/10.1021/cm403028b.

(7) Dong, H.; Paramonov, S. E.; Aulisa, L.; Bakota, E. L.; Hartgerink, J. D. Self-Assembly of Multidomain Peptides: Balancing Molecular Frustration Controls Conformation and Nanostructure. *Journal of the American Chemical Society* **2007**, *129* (41), 12468–12472. https://doi.org/10.1021/ja072536r.

(8) Aida, T.; Meijer, E. W.; Stupp, S. I. Functional Supramolecular Polymers. *Science* **2012**, *335* (6070), 813–817. https://doi.org/10.1126/science.1205962.

(9) Weingarten, A. S.; Kazantsev, R. V.; Palmer, L. C.; McClendon, M.; Koltonow, A. R.; Samuel, A. P. S.; Kiebala, D. J.; Wasielewski, M. R.; Stupp, S. I. Self-Assembling Hydrogel Scaffolds for Photocatalytic Hydrogen Production. *Nature Chem* **2014**, *6* (11), 964–970. https://doi.org/10.1038/nchem.2075.

(10) Antonietti, M.; Förster, S. Vesicles and Liposomes: A Self-Assembly Principle Beyond Lipids. *Advanced Materials* **2003**, *15* (16), 1323–1333. https://doi.org/10.1002/adma.200300010.

(11) Yang, Y.; Wang, J.; Shigematsu, H.; Xu, W.; Shih, W. M.; Rothman, J. E.; Lin, C. Self-Assembly of Size-Controlled Liposomes on DNA Nanotemplates. *Nature Chemistry* **2016**, *8* (5), 476–483. https://doi.org/10.1038/nchem.2472.

(12) Dreher, M. R.; Simnick, A. J.; Fischer, K.; Smith, R. J.; Patel, A.; Schmidt, M.; Chilkoti, A. Temperature Triggered Self-Assembly of Polypeptides into Multivalent Spherical Micelles. *Journal of the American Chemical Society* **2008**, *130* (2), 687–694. https://doi.org/10.1021/ja0764862.

(13) Israelachvili, J. N.; Mitchell, D. J.; Ninham, B. W. Theory of Self-Assembly of Hydrocarbon Amphiphiles into Micelles and Bilayers. *Journal of the Chemical Society, Faraday Transactions 2: Molecular and Chemical Physics* **1976**, *72* (June 2015), 1525–1568. https://doi.org/10.1039/F29767201525.

(14) Gröschel, A. H.; Schacher, F. H.; Schmalz, H.; Borisov, O. V.; Zhulina, E. B.; Walther, A.; Müller, A. H. E. Precise Hierarchical Self-Assembly of Multicompartment Micelles. *Nature Communications* **2012**, *3*. https://doi.org/10.1038/ncomms1707.

(15) Stupp, S. I.; LeBonheur, V.; Walker, K.; Li, L. S.; Huggins, K. E.; Keser, M.; Amstutz, A. Supramolecular Materials: Self-Organized Nanostructures. *Science* **1997**, *276* (5311), 384–389. https://doi.org/10.1126/science.276.5311.384.

(16) Lee, H. K.; Soukasene, S.; Jiang, H.; Zhang, S.; Feng, W.; Stupp, S. I. Light-Induced Self-Assembly of Nanofibers inside Liposomes. *Soft Matter* **2008**, *4* (5), 962–964. https://doi.org/10.1039/b719486b.

(17) Berns, E. J.; Sur, S.; Pan, L.; Goldberger, J. E.; Suresh, S.; Zhang, S.; Kessler, J. A.; Stupp, S. I. Aligned Neurite Outgrowth and Directed Cell Migration in Self-Assembled Monodomain Gels. *Biomaterials* **2014**, *35* (1), 185–195. https://doi.org/10.1016/j.biomaterials.2013.09.077.

(18) Muraoka, T.; Koh, C. Y.; Cui, H.; Stupp, S. I. Light-Triggered Bioactivity in Three Dimensions. *Angewandte Chemie - International Edition* **2009**, *48* (32), 5946–5949. https://doi.org/10.1002/anie.200901524.

(19) Hartgerink, J. D.; Beniash, E.; Stupp, S. I. Self-Assembly and Mineralization of Peptide-Amphiphile Nanofibers. *Science* **2001**, *294* (5547), 1684–1688. https://doi.org/10.1126/science.1063187.

(20) Jang, W. D.; Aida, T. Supramolecular Nanofiber Formation of Macrocyclic Dendrimer. *Macromolecules* **2004**, *37* (19), 7325–7330. https://doi.org/10.1021/ma0492364.

(21) Wang, X.; Guerin, G.; Wang, H.; Wang, Y.; Manners, I.; Winnik, M. a. Cylindrical Block Copolymer Micelles and Co-Micelles of Controlled Length and Architecture. *Science* **2007**, *317* (5838), 644–647. https://doi.org/10.1126/science.1141382.

(22) Gilroy, J. B.; Gädt, T.; Whittell, G. R.; Chabanne, L.; Mitchels, J. M.; Richardson, R. M.; Winnik, M. A.; Manners, I. Monodisperse Cylindrical Micelles by Crystallization-Driven Living Self-Assembly. *Nature Chemistry* **2010**, *2* (7), 566–570. https://doi.org/10.1038/nchem.664.

(23) Rupar, P. A.; Chabanne, L.; Winnik, M. A.; Manners, I. Non-Centrosymmetric Cylindrical Micelles by Unidirectional Growth. *Science* **2012**, *337* (6094), 559–562. https://doi.org/10.1126/science.1221206.

(24) Lehrman, J. A.; Cui, H.; Tsai, W. W.; Moyer, T. J.; Stupp, S. I. Supramolecular Control of Self-Assembling Terthiophene–Peptide Conjugates through the Amino Acid Side Chain. *Chemical Communications* **2012**, *48* (78), 9711–9713. https://doi.org/10.1039/c2cc34375d.

(25) Hill, J. P.; Jin, W.; Kosaka, A.; Fukushima, T.; Ichihara, H.; Shimomura, T.; Ito, K.; Hashizume, T.; Ishii, N.; Aida, T. Self-Assembled Hexa-Peri-Hexabenzocoronene Graphitic Nanotube. *Science* **2004**, *304* (5676), 1481–1483. https://doi.org/10.1126/science.1097789.

(26) Yan, C.; Liu, J.; Liu, F.; Wu, J.; Gao, K.; Xue, D. Tube Formation in Nanoscale Materials. *Nanoscale Research Letters* **2008**, *3* (12), 473–480. https://doi.org/10.1007/s11671-008-9193-6.

(27) Zubarev, E. R.; Pralle, M. U.; Sone, E. D.; Stupp, S. I. Self-Assembly of Dendron Rodcoil Molecules into Nanoribbons. *Journal of the American Chemical Society* **2001**, *123* (17), 4105–4106. https://doi.org/10.1021/ja015653+.

(28) Vyborna, Y.; Vybornyi, M.; Rudnev, A. V.; Häner, R. DNA-Grafted Supramolecular Polymers: Helical Ribbon Structures Formed by Self-Assembly of Pyrene-DNA Chimeric Oligomers. *Angewandte Chemie - International Edition* **2015**, *54* (27), 7934–7938. https://doi.org/10.1002/anie.201502066.

(29) Messmore, B. W.; Hulvat, J. F.; Sone, E. D.; Stupp, S. I. Synthesis, Self-Assembly, and Characterization of Supramolecular Polymers from Electroactive Dendron Rodcoil Molecules. *Journal of the American Chemical Society* **2004**, *126* (44), 14452–14458. https://doi.org/10.1021/ja049325w.

(30) Mak, T. C. W.; Xue, F. Supramolecular Rosette Ribbon Constructed from Guanidinium and Hydrogen Carbonate Ions in the Crystal Engineering of Hydrogen-Bonded Networks. *Journal of the American Chemical Society* **2000**, *122* (40), 9860–9861. https://doi.org/10.1021/ja001851+.

(31) Stupp, S. I.; Son, S.; Lin, H. C.; Li, L. S. Synthesis of Two-Dimensional Polymers. *Science* **1993**, *259* (5091), 59–63. https://doi.org/10.1126/science.259.5091.59.

(32) Stupp, S. I.; Son, S.; Li, L. S.; Lin, H. C.; Keser, M. Bulk Synthesis of Two-Dimensional Polymers: The Molecular Recognition Approach. *Journal of the American Chemical Society* **1995**, *117* (19), 5212–5227. https://doi.org/10.1021/ja00124a005.

(33) De Feyter, S.; Miura, A.; Yao, S.; Chen, Z.; Würthner, F.; Jonkheijm, P.; Schenning, A. P. H. J.; Meijer, E. W.; De Schryver, F. C. Two-Dimensional Self-Assembly into Multicomponent Hydrogen-Bonded Nanostructures. *Nano Letters* **2005**, *5* (1), 77–81. https://doi.org/10.1021/nl048360y.

(34) Suzuki, Y.; Endo, M.; Sugiyama, H. Lipid-Bilayer-Assisted Two-Dimensional Self-Assembly of DNA Origami Nanostructures. *Nature Communications* **2015**, *6*. https://doi.org/10.1038/ncomms9052.

(35) Hendricks, M. P.; Sato, K.; Palmer, L. C.; Stupp, S. I. Supramolecular Assembly of Peptide Amphiphiles. *Accounts of Chemical Research* **2017**, *50*, 2440–2448. https://doi.org/10.1021/acs.accounts.7b00297.

(36) *Fennema's Food Chemistry*, 4th ed.; Damodaran, S., Parkin, K. L., Fennema, O. R., Eds.; CRC Press: Boca Raton, 2008.

(37) Bae, K. H.; Kurisawa, M. Emerging Hydrogel Designs for Controlled Protein Delivery. *Biomater. Sci.* **2016**, *4*, 1184–1192. https://doi.org/10.1039/C6BM00330C.

(38) Vermonden, T.; Censi, R.; Hennink, W. E. Hydrogels for Protein Delivery. *Chemical Reviews* **2012**, *112* (5), 2853–2888. https://doi.org/10.1021/cr200157d.

(39) Fosgerau, K.; Hoffmann, T. Peptide Therapeutics: Current Status and Future Directions. *Drug Discovery Today* **2015**, *20* (1), 122–128. https://doi.org/10.1016/j.drudis.2014.10.003.

(40) Wang, J.; Liu, K.; Xing, R.; Yan, X. Peptide Self-Assembly: Thermodynamics and Kinetics. *Chemical Society Reviews* **2016**, *45* (20), 5589–5604. https://doi.org/10.1039/c6cs00176a.

(41) Berndt, P.; Fields, G. B.; Tirrell, M. Synthetic Lipidation of Peptides and Amino Acids: Monolayer Structure and Properties. *Journal of the American Chemical Society* **1995**, *117* (37), 9515–9522. https://doi.org/10.1021/ja00142a019.

(42) Ortony, J. H.; Newcomb, C. J.; Matson, J. B.; Palmer, L. C.; Doan, P. E.; Hoffman, B. M.; Stupp, S. I. Internal Dynamics of a Supramolecular Nanofibre. *Nature Mater* **2014**, *13* (8), 812–816. https://doi.org/10.1038/nmat3979.

(43) Tantakitti, F.; Boekhoven, J.; Wang, X.; Kazantsev, R. V.; Yu, T.; Li, J.; Zhuang, E.; Zandi, R.; Ortony, J. H.; Newcomb, C. J.; Palmer, L. C.; Shekhawat, G. S.; de la Cruz, M. O.; Schatz, G. C.; Stupp, S. I. Energy Landscapes and Functions of Supramolecular Systems. *Nature Mater* **2016**, *15* (4), 469–476. https://doi.org/10.1038/nmat4538.

(44) Hartgerink, J. D.; Beniash, E.; Stupp, S. I. Peptide-Amphiphile Nanofibers: A Versatile Scaffold for the Preparation of Self-Assembling Materials. *Proceedings of the National Academy of Sciences* **2002**, *99* (8), 5133–5138. https://doi.org/10.1073/pnas.072699999.

(45) Silva, G. A.; Czeisler, C.; Niece, K. L.; Beniash, E.; Harrington, D. A.; Kessler, J. A.; Stupp, S. I. Selective Differentiation of Neural Progenitor Cells by High-Epitope Density Nanofibers. *Science (New York, N.Y.)* **2004**, *303* (5662), 1352–1355. https://doi.org/10.1126/science.1093783.

(46) Bakshi, R.; Hokugo, A.; Khalil, D.; Wang, L.; Shibuya, Y.; Zhou, S.; Zhang, Z.; Rezzadeh, K.; McClendon, M.; Stupp, S. I.; Jarrahy, R. A Chemotactic Functional Scaffold with VEGF-Releasing Peptide Amphiphiles Facilitates Bone Regeneration by

BMP-2 in a Large-Scale Rodent Cranial Defect Model. *Plastic & Reconstructive Surgery* **2021**, *147* (2), 386–397. https://doi.org/10.1097/PRS.0000000000007551.

(47) Lee, S. S.; Hsu, E. L.; Mendoza, M.; Ghodasra, J.; Nickoli, M. S.; Ashtekar, A.; Polavarapu, M.; Babu, J.; Riaz, R. M.; Nicolas, J. D.; Nelson, D.; Hashmi, S. Z.; Kaltz, S. R.; Earhart, J. S.; Merk, B. R.; McKee, J. S.; Bairstow, S. F.; Shah, R. N.; Hsu, W. K.; Stupp, S. I. Gel Scaffolds of BMP-2-Binding Peptide Amphiphile Nanofibers for Spinal Arthrodesis. *Adv. Healthcare Mater.* **2015**, *4* (1), 131–141. https://doi.org/10.1002/adhm.201400129.

(48) Tansik, G.; Kilic, E.; Beter, M.; Demiralp, B.; Kiziltas Sendur, G.; Can, N.; Ozkan, H.; Ergul, E.; Guler, M. O.; Tekinay, A. B. A Glycosaminoglycan Mimetic Peptide Nanofiber Gel as an Osteoinductive Scaffold. *Biomater. Sci.* **2016**, *4* (9), 1328–1339. https://doi.org/10.1039/C6BM00179C.

(49) Tysseling-Mattiace, V. M.; Sahni, V.; Niece, K. L.; Birch, D.; Czeisler, C.; Fehlings, M. G.; Stupp, S. I.; Kessler, J. A. Self-Assembling Nanofibers Inhibit Glial Scar Formation and Promote Axon Elongation after Spinal Cord Injury. *Journal of Neuroscience* **2008**, *28* (14), 3814–3823. https://doi.org/10.1523/JNEUROSCI.0143-08.2008.

(50) Edelbrock, A. N.; Àlvarez, Z.; Simkin, D.; Fyrner, T.; Chin, S. M.; Sato, K.; Kiskinis, E.; Stupp, S. I. Supramolecular Nanostructure Activates TrkB Receptor Signaling of Neuronal Cells by Mimicking Brain-Derived Neurotrophic Factor. *Nano Lett.* **2018**, *18* (10), 6237–6247. https://doi.org/10.1021/acs.nanolett.8b02317.

(51) Tongers, J.; Webber, M. J.; Vaughan, E. E.; Sleep, E.; Renault, M.-A.; Roncalli, J. G.; Klyachko, E.; Thorne, T.; Yu, Y.; Marquardt, K.-T.; Kamide, C. E.; Ito, A.; Misener, S.; Millay, M.; Liu, T.; Jujo, K.; Qin, G.; Losordo, D. W.; Stupp, S. I.; Kishore, R. Enhanced Potency of Cell-Based Therapy for Ischemic Tissue Repair Using an Injectable Bioactive Epitope Presenting Nanofiber Support Matrix. *Journal of Molecular and Cellular Cardiology* **2014**, *74*, 231–239. https://doi.org/10.1016/j.yjmcc.2014.05.017.

(52) Rajangam, K.; Behanna, H. A.; Hui, M. J.; Han, X.; Hulvat, J. F.; Lomasney, J. W.; Stupp, S. I. Heparin Binding Nanostructures to Promote Growth of Blood Vessels. *Nano Lett.* **2006**, *6* (9), 2086–2090. https://doi.org/10.1021/nl0613555.

(53) Wegst, U. G. K.; Bai, H.; Saiz, E.; Tomsia, A. P.; Ritchie, R. O. Bioinspired Structural Materials. *Nature Mater* **2015**, *14* (1), 23–36. https://doi.org/10.1038/nmat4089.

(54) Lakes, R. Materials with Structural Hierarchy. *Nature* **1993**, *361* (6412), 511–515. https://doi.org/10.1038/361511a0.

(55) Tskhovrebova, L.; Trinick, J. Titin: Properties and Family Relationships. *Nature Reviews Molecular Cell Biology* **2003**, *4* (9), 679–689. https://doi.org/10.1038/nrm1198.

(56) Fratzl, P.; Weinkamer, R. Nature's Hierarchical Materials. *Progress in Materials Science* **2007**, *52* (8), 1263–1334. https://doi.org/10.1016/j.pmatsci.2007.06.001.

(57) Chin, S. M.; Synatschke, C. V.; Liu, S.; Nap, R. J.; Sather, N. A.; Wang, Q.; Álvarez, Z.; Edelbrock, A. N.; Fyrner, T.; Palmer, L. C.; Szleifer, I.; Olvera De La Cruz, M.; Stupp, S. I. Covalent-Supramolecular Hybrid Polymers as Muscle-Inspired Anisotropic Actuators. *Nature Communications* **2018**, *9* (1), 1–11. https://doi.org/10.1038/s41467-018-04800-w.

(58) Zhang, S.; Greenfield, M. A.; Mata, A.; Palmer, L. C.; Bitton, R.; Mantei, J. R.; Aparicio, C.; de la Cruz, M. O.; Stupp, S. I. A Self-Assembly Pathway to Aligned Monodomain Gels. *Nature Mater* **2010**, *9* (7), 594–601. https://doi.org/10.1038/nmat2778.

(59) Stendahl, J. C.; Rao, M. S.; Guler, M. O.; Stupp, S. I. Intermolecular Forces in the Self-Assembly of Peptide Amphiphile Nanofibers. *Adv. Funct. Mater.* **2006**, *16* (4), 499–508. https://doi.org/10.1002/adfm.200500161.

(60) Greenfield, M. A.; Hoffman, J. R.; Olvera de la Cruz, M.; Stupp, S. I. Tunable Mechanics of Peptide Nanofiber Gels. *Langmuir* **2010**, *26* (5), 3641–3647. https://doi.org/10.1021/la9030969.

(61) Capito, R. M.; Azevedo, H. S.; Velichko, Y. S.; Mata, A.; Stupp, S. I. Self-Assembly of Large and Small Molecules into Hierarchically Ordered Sacs and Membranes. *Science* **2008**, *319* (5871), 1812–1816. https://doi.org/10.1126/science.1154586.

(62) Carvajal, D.; Bitton, R.; Mantei, J. R.; Velichko, Y. S.; Stupp, S. I.; Shull, K. R. Physical Properties of Hierarchically Ordered Self-Assembled Planar and Spherical Membranes. *Soft Matter* **2010**, *6* (8), 1816. https://doi.org/10.1039/b923903k.

(63) Bitton, R.; Chow, L. W.; Zha, R. H.; Velichko, Y. S.; Pashuck, E. T.; Stupp, S. I. Electrostatic Control of Structure in Self-Assembled Membranes. *Small* **2014**, *10* (3), 500–505. https://doi.org/10.1002/smll.201300254.

(64) Velichko, Y. S.; Mantei, J. R.; Bitton, R.; Carvajal, D.; Shull, K. R.; Stupp, S. I. Electric Field Controlled Self-Assembly of Hierarchically Ordered Membranes. *Advanced Functional Materials* **2012**, *22* (2), 369–377. https://doi.org/10.1002/adfm.201101538.

(65) Borges, J.; Sousa, M. P.; Cinar, G.; Caridade, S. G.; Guler, M. O.; Mano, J. F. Nanoengineering Hybrid Supramolecular Multilayered Biomaterials Using Polysaccharides and Self-Assembling Peptide Amphiphiles. *Advanced Functional Materials* **2017**, 1605122. https://doi.org/10.1002/adfm.201605122.

(66) Inostroza-Brito, K. E.; Collin, E.; Siton-Mendelson, O.; Smith, K. H.; Monge-Marcet, A.; Ferreira, D. S.; Rodríguez, R. P.; Alonso, M.; Rodríguez-Cabello, J. C.; Reis, R. L.; Sagués, F.; Botto, L.; Bitton, R.; Azevedo, H. S.; Mata, A. Co-Assembly, Spatiotemporal Control and Morphogenesis of a Hybrid Protein-Peptide System. *Nature Chemistry* **2015**, *7* (11), 897–904. https://doi.org/10.1038/nchem.2349.

(67) Hedegaard, C. L.; Collin, E. C.; Redondo-Gómez, C.; Nguyen, L. T. H.; Ng, K. W.; Castrejón-Pita, A. A.; Castrejón-Pita, J. R.; Mata, A. Hydrodynamically Guided Hierarchical Self-Assembly of Peptide – Protein Bioinks. *Advanced Functional Materials* **2018**, *28*, 1–13. https://doi.org/10.1002/adfm.201703716.

(68) Zha, R. H.; Sur, S.; Stupp, S. I. Self-Assembly of Cytotoxic Peptide Amphiphiles into Supramolecular Membranes for Cancer Therapy. *Advanced Healthcare Materials* **2013**, *2* (1), 126–133. https://doi.org/10.1002/adhm.201200118.

(69) Standley, S. M.; Toft, D. J.; Cheng, H.; Soukasene, S.; Chen, J.; Raja, S. M.; Band, V.; Band, H.; Cryns, V. L.; Stupp, S. I. Induction of Cancer Cell Death by Self-Assembling Nanostructures Incorporating a Cytotoxic Peptide. *Cancer Res* **2010**, *70* (8), 3020–3026. https://doi.org/10.1158/0008-5472.CAN-09-3267.

(70) Toft, D. J.; Moyer, T. J.; Standley, S. M.; Ruff, Y.; Ugolkov, A.; Stupp, S. I.; Cryns, V. L. Coassembled Cytotoxic and Pegylated Peptide Amphiphiles Form Filamentous Nanostructures with Potent Antitumor Activity in Models of Breast Cancer. *ACS Nano* **2012**, *6* (9), 7956–7965. https://doi.org/10.1021/nn302503s.

(71) Chow, L. W.; Bitton, R.; Webber, M. J.; Carvajal, D.; Shull, K. R.; Sharma, A. K.; Stupp, S. I. A Bioactive Self-Assembled Membrane to Promote Angiogenesis. *Biomaterials* **2011**, *32* (6), 1574–1582. https://doi.org/10.1016/j.biomaterials.2010.10.048.

(72) Hou, X.; Zhang, Y. S.; Santiago, G. T.; Alvarez, M. M.; Ribas, J.; Jonas, S. J.; Weiss, P. S.; Andrews, A. M.; Aizenberg, J.; Khademhosseini, A. Interplay between Materials and Microfluidics. *Nat Rev Mater* **2017**, *2* (5), 17016. https://doi.org/10.1038/natrevmats.2017.16.

(73) Nielsen, J. B.; Hanson, R. L.; Almughamsi, H. M.; Pang, C.; Fish, T. R.; Woolley, A. T. Microfluidics: Innovations in Materials and Their Fabrication and Functionalization. *Anal. Chem.* **2020**, *92* (1), 150–168. https://doi.org/10.1021/acs.analchem.9b04986.

(74) Abdelgawad, M.; Watson, M. W. L.; Young, E. W. K.; Mudrik, J. M.; Ungrin, M. D.; Wheeler, A. R. Soft Lithography: Masters on Demand. *Lab Chip* **2008**, *8* (8), 1379. https://doi.org/10.1039/b804050h.

(75) Herranz-Blanco, B.; Ginestar, E.; Zhang, H.; Hirvonen, J.; Santos, H. A. Microfluidics Platform for Glass Capillaries and Its Application in Droplet and Nanoparticle Fabrication. *International Journal of Pharmaceutics* **2017**, *516* (1–2), 100–105. https://doi.org/10.1016/j.ijpharm.2016.11.024.

(76) Xia, Y.; Whitesides, G. M. Soft Lithography. *Annual Review of Materials Science* **1998**, *28* (1), 153–184. https://doi.org/10.1146/annurev.matsci.28.1.153.

(77) McDonald, J. C.; Duffy, D. C.; Anderson, J. R.; Chiu, D. T.; Wu, H.; Schueller, O. J. A.; Whitesides, G. M. Fabrication of Microfluidic Systems in Poly(Dimethylsiloxane). *Electrophoresis* **2000**, *21* (1), 27–40. https://doi.org/10.1002/(SICI)1522-2683(20000101)21:1<27::AID-ELPS27>3.0.CO;2-C.

(78) Mao, A. S.; Shin, J.-W.; Utech, S.; Wang, H.; Uzun, O.; Li, W.; Cooper, M.; Hu, Y.; Zhang, L.; Weitz, D. A.; Mooney, D. J. Deterministic Encapsulation of Single Cells in Thin Tunable Microgels for Niche Modelling and Therapeutic Delivery. *Nature Mater* **2017**, *16* (2), 236–243. https://doi.org/10.1038/nmat4781.

(79) Mao, A. S.; Özkale, B.; Shah, N. J.; Vining, K. H.; Descombes, T.; Zhang, L.; Tringides, C. M.; Wong, S.-W.; Shin, J.-W.; Scadden, D. T.; Weitz, D. A.; Mooney, D. J. Programmable Microencapsulation for Enhanced Mesenchymal Stem Cell Persistence and Immunomodulation. *Proc Natl Acad Sci USA* **2019**, *116* (31), 15392–15397. https://doi.org/10.1073/pnas.1819415116.

(80) Headen, D. M.; García, J. R.; García, A. J. Parallel Droplet Microfluidics for High Throughput Cell Encapsulation and Synthetic Microgel Generation. *Microsyst Nanoeng* **2018**, *4* (1), 17076. https://doi.org/10.1038/micronano.2017.76.

(81) Kamperman, T.; Henke, S.; Visser, C. W.; Karperien, M.; Leijten, J. Centering Single Cells in Microgels via Delayed Crosslinking Supports Long-Term 3D Culture by Preventing Cell Escape. *Small* **2017**, *13* (22), 1603711. https://doi.org/10.1002/smll.201603711.

(82) Liu, D.; Zhang, H.; Fontana, F.; Hirvonen, J. T.; Santos, H. A. Microfluidic-Assisted Fabrication of Carriers for Controlled Drug Delivery. *Lab Chip* **2017**, *17* (11), 1856–1883. https://doi.org/10.1039/C7LC00242D.

(83) Wang, W.; Zhang, M.-J.; Chu, L.-Y. Functional Polymeric Microparticles Engineered from Controllable Microfluidic Emulsions. *Acc. Chem. Res.* **2014**, *47* (2), 373–384. https://doi.org/10.1021/ar4001263.

(84) Duncanson, W. J.; Lin, T.; Abate, A. R.; Seiffert, S.; Shah, R. K.; Weitz, D. A. Microfluidic Synthesis of Advanced Microparticles for Encapsulation and Controlled Release. *Lab Chip* **2012**, *12* (12), 2135. https://doi.org/10.1039/c2lc21164e.

(85) Trantidou, T.; Friddin, M.; Elani, Y.; Brooks, N. J.; Law, R. V.; Seddon, J. M.; Ces, O. Engineering Compartmentalized Biomimetic Micro- and Nanocontainers. *ACS Nano* **2017**, *11* (7), 6549–6565. https://doi.org/10.1021/acsnano.7b03245.

(86) Kamiya, K.; Takeuchi, S. Giant Liposome Formation toward the Synthesis of Well-Defined Artificial Cells. *J. Mater. Chem. B* **2017**, *5* (30), 5911–5923. https://doi.org/10.1039/C7TB01322A.

(87) Deng, N.-N.; Yelleswarapu, M.; Zheng, L.; Huck, W. T. S. Microfluidic Assembly of Monodisperse Vesosomes as Artificial Cell Models. *J. Am. Chem. Soc.* **2017**, *139* (2), 587–590. https://doi.org/10.1021/jacs.6b10977.

(88) Ho, K. K. Y.; Lee, L. M.; Liu, A. P. Mechanically Activated Artificial Cell by Using Microfluidics. *Sci Rep* **2016**, *6* (1), 32912. https://doi.org/10.1038/srep32912.

(89) Ai, Y.; Xie, R.; Xiong, J.; Liang, Q. Microfluidics for Biosynthesizing: From Droplets and Vesicles to Artificial Cells. *Small* **2020**, *16* (9), 1903940. https://doi.org/10.1002/smll.201903940.

(90) Del Bakhshayesh, A. R.; Asadi, N.; Alihemmati, A.; Tayefi Nasrabadi, H.; Montaseri, A.; Davaran, S.; Saghati, S.; Akbarzadeh, A.; Abedelahi, A. An Overview of Advanced Biocompatible and Biomimetic Materials for Creation of Replacement Structures in the Musculoskeletal Systems: Focusing on Cartilage Tissue Engineering. *J Biol Eng* **2019**, *13* (1), 85. https://doi.org/10.1186/s13036-019-0209-9.

(91) Huang, G.; Li, F.; Zhao, X.; Ma, Y.; Li, Y.; Lin, M.; Jin, G.; Lu, T. J.; Genin, G. M.; Xu, F. Functional and Biomimetic Materials for Engineering of the Three-Dimensional Cell Microenvironment. *Chem. Rev.* **2017**, *117* (20), 12764–12850. https://doi.org/10.1021/acs.chemrev.7b00094.

(92) Kim, H. D.; Amirthalingam, S.; Kim, S. L.; Lee, S. S.; Rangasamy, J.; Hwang, N. S. Biomimetic Materials and Fabrication Approaches for Bone Tissue Engineering. *Advanced Healthcare Materials* **2017**, *6* (23), 1700612. https://doi.org/10.1002/adhm.201700612.

(93) Levin, A.; Hakala, T. A.; Schnaider, L.; Bernardes, G. J. L.; Gazit, E.; Knowles, T. P. J. Biomimetic Peptide Self-Assembly for Functional Materials. *Nat Rev Chem* **2020**, *4* (11), 615–634. https://doi.org/10.1038/s41570-020-0215-y.

(94) Silvestri, A.; Boffito, M.; Sartori, S.; Ciardelli, G. Biomimetic Materials and Scaffolds for Myocardial Tissue Regeneration. *Macromolecular Bioscience* **2013**, *13* (8), 984–1019. https://doi.org/10.1002/mabi.201200483.

(95) Bowers, S. L. K.; Banerjee, I.; Baudino, T. A. The Extracellular Matrix: At the Center of It All. *Journal of Molecular and Cellular Cardiology* **2010**, *48* (3), 474–482. https://doi.org/10.1016/j.yjmcc.2009.08.024.

(96) Mecham, R. P. Overview of Extracellular Matrix. *Current Protocols in Cell Biology* **2012**, *57* (1). https://doi.org/10.1002/0471143030.cb1001s57.

(97) Theocharis, A. D.; Skandalis, S. S.; Gialeli, C.; Karamanos, N. K. Extracellular Matrix Structure. *Advanced Drug Delivery Reviews* **2016**, *97*, 4–27. https://doi.org/10.1016/j.addr.2015.11.001.

(98) Bosman, F. T.; Stamenkovic, I. Functional Structure and Composition of the Extracellular Matrix: Structure and Composition of the Extracellular Matrix. *J. Pathol.* **2003**, *200* (4), 423–428. https://doi.org/10.1002/path.1437.

(99) Daniele, M. A.; Boyd, D. A.; Adams, A. A.; Ligler, F. S. Microfluidic Strategies for Design and Assembly of Microfibers and Nanofibers with Tissue Engineering and Regenerative Medicine Applications. *Adv. Healthcare Mater.* **2015**, *4* (1), 11–28. https://doi.org/10.1002/adhm.201400144.

(100) Ma, S.; Mukherjee, N. Microfluidics Fabrication of Soft Microtissues and Bottom-Up Assembly. *Adv. Biosys.* **2018**, *2* (9), 1800119. https://doi.org/10.1002/adbi.201800119.

(101) Du, X.; Li, Q.; Wu, G.; Chen, S. Multifunctional Micro/Nanoscale Fibers Based on Microfluidic Spinning Technology. *Adv. Mater.* **2019**, *31* (52), 1903733. https://doi.org/10.1002/adma.201903733.

(102) Cheng, J.; Jun, Y.; Qin, J.; Lee, S.-H. Electrospinning versus Microfluidic Spinning of Functional Fibers for Biomedical Applications. *Biomaterials* **2017**, *114*, 121–143. https://doi.org/10.1016/j.biomaterials.2016.10.040.

(103) Chung, B. G.; Lee, K.-H.; Khademhosseini, A.; Lee, S.-H. Microfluidic Fabrication of Microengineered Hydrogels and Their Application in Tissue Engineering. *Lab Chip* **2012**, *12* (1), 45–59. https://doi.org/10.1039/C1LC20859D.

(104) Jun, Y.; Kang, E.; Chae, S.; Lee, S.-H. Microfluidic Spinning of Micro- and Nano-Scale Fibers for Tissue Engineering. *Lab Chip* **2014**, *14* (13), 2145–2160. https://doi.org/10.1039/C3LC51414E.

(105) Choi, C.-H.; Yi, H.; Hwang, S.; Weitz, D. A.; Lee, C.-S. Microfluidic Fabrication of Complex-Shaped Microfibers by Liquid Template-Aided Multiphase Microflow. *Lab Chip* **2011**, *11* (8), 1477. https://doi.org/10.1039/c0lc00711k.

(106) Sharifi, F.; Bai, Z.; Montazami, R.; Hashemi, N. Mechanical and Physical Properties of Poly(Vinyl Alcohol) Microfibers Fabricated by a Microfluidic Approach. *RSC Adv.* **2016**, *6* (60), 55343–55353. https://doi.org/10.1039/C6RA09519D.

(107) Duboin, A.; Middleton, R.; Malloggi, F.; Monti, F.; Tabeling, P. Cusps, Spouts and Microfiber Synthesis with Microfluidics. *Soft Matter* **2013**, *9* (11), 3041. https://doi.org/10.1039/c2sm27142g.

(108) Jung, J.-H.; Choi, C.-H.; Chung, S.; Chung, Y.-M.; Lee, C.-S. Microfluidic Synthesis of a Cell Adhesive Janus Polyurethane Microfiber. *Lab Chip* **2009**, *9* (17), 2596. https://doi.org/10.1039/b901308c.

(109) Nunes, J. K.; Sadlej, K.; Tam, J. I.; Stone, H. A. Control of the Length of Microfibers. *Lab Chip* **2012**, *12* (13), 2301. https://doi.org/10.1039/c2lc40280g.

(110) Yamada, M.; Utoh, R.; Ohashi, K.; Tatsumi, K.; Yamato, M.; Okano, T.; Seki, M. Controlled Formation of Heterotypic Hepatic Micro-Organoids in Anisotropic Hydrogel Microfibers for Long-Term Preservation of Liver-Specific Functions. *Biomaterials* **2012**, *33* (33), 8304–8315. https://doi.org/10.1016/j.biomaterials.2012.07.068.

(111) Yamada, M.; Sugaya, S.; Naganuma, Y.; Seki, M. Microfluidic Synthesis of Chemically and Physically Anisotropic Hydrogel Microfibers for Guided Cell Growth and Networking. *Soft Matter* **2012**, *8* (11), 3122. https://doi.org/10.1039/c2sm07263g.

(112) Jeong, W.; Kim, J.; Kim, S.; Lee, S.; Mensing, G.; Beebe, David. J. Hydrodynamic Microfabrication via "on the Fly" Photopolymerization of Microscale Fibers and Tubes. *Lab Chip* **2004**, *4* (6), 576–580. https://doi.org/10.1039/B411249K.

(113) Lee, K. H.; Shin, S. J.; Park, Y.; Lee, S.-H. Synthesis of Cell-Laden Alginate Hollow Fibers Using Microfluidic Chips and Microvascularized Tissue-Engineering Applications. *Small* **2009**, *5* (11), 1264–1268. https://doi.org/10.1002/smll.200801667.

(114) Yu, Y.; Shang, L.; Guo, J.; Wang, J.; Zhao, Y. Design of Capillary Microfluidics for Spinning Cell-Laden Microfibers. *Nat Protoc* **2018**, *13* (11), 2557–2579. https://doi.org/10.1038/s41596-018-0051-4.

(115) Onoe, H.; Okitsu, T.; Itou, A.; Kato-Negishi, M.; Gojo, R.; Kiriya, D.; Sato, K.; Miura, S.; Iwanaga, S.; Kuribayashi-Shigetomi, K.; Matsunaga, Y. T.; Shimoyama, Y.; Takeuchi, S. Metre-Long Cell-Laden Microfibres Exhibit Tissue Morphologies and Functions. *Nature Mater* **2013**, *12* (6), 584–590. https://doi.org/10.1038/nmat3606.

(116) Hsiao, A. Y.; Okitsu, T.; Onoe, H.; Kiyosawa, M.; Teramae, H.; Iwanaga, S.; Kazama, T.; Matsumoto, T.; Takeuchi, S. Smooth Muscle-Like Tissue Constructs with Circumferentially Oriented Cells Formed by the Cell Fiber Technology. *PLoS ONE* **2015**, *10* (3), e0119010. https://doi.org/10.1371/journal.pone.0119010.

(117) Cheng, Y.; Zheng, F.; Lu, J.; Shang, L.; Xie, Z.; Zhao, Y.; Chen, Y.; Gu, Z. Bioinspired Multicompartmental Microfibers from Microfluidics. *Adv. Mater.* **2014**, *26* (30), 5184–5190. https://doi.org/10.1002/adma.201400798.

(118) Cheng, Y.; Yu, Y.; Fu, F.; Wang, J.; Shang, L.; Gu, Z.; Zhao, Y. Controlled Fabrication of Bioactive Microfibers for Creating Tissue Constructs Using Microfluidic Techniques. *ACS Appl. Mater. Interfaces* **2016**, *8* (2), 1080–1086. https://doi.org/10.1021/acsami.5b11445.

(119) Shang, L.; Fu, F.; Cheng, Y.; Yu, Y.; Wang, J.; Gu, Z.; Zhao, Y. Bioinspired Multifunctional Spindle-Knotted Microfibers from Microfluidics. *Small* **2017**, *13* (4), 1600286. https://doi.org/10.1002/smll.201600286.

(120) Boyd, D. A.; Shields, A. R.; Howell, P. B.; Ligler, F. S. Design and Fabrication of Uniquely Shaped Thiol–Ene Microfibers Using a Two-Stage Hydrodynamic Focusing Design. *Lab Chip* **2013**, *13* (15), 3105. https://doi.org/10.1039/c3lc50413a.

(121) Boyd, D. A.; Shields, A. R.; Naciri, J.; Ligler, F. S. Hydrodynamic Shaping, Polymerization, and Subsequent Modification of Thiol Click Fibers. *ACS Appl. Mater. Interfaces* **2013**, *5* (1), 114–119. https://doi.org/10.1021/am3022834.

(122) Lee, M. G.; Choi, S.; Park, J.-K. Three-Dimensional Hydrodynamic Focusing with a Single Sheath Flow in a Single-Layer Microfluidic Device. *Lab Chip* **2009**, *9* (21), 3155. https://doi.org/10.1039/b910712f.

(123) Thangawng, A. L.; Howell, Jr, P. B.; Spillmann, C. M.; Naciri, J.; Ligler, F. S. UV Polymerization of Hydrodynamically Shaped Fibers. *Lab Chip* **2011**, *11* (6), 1157. https://doi.org/10.1039/c0lc00392a.

(124) Thangawng, A. L.; Howell Jr, P. B.; Richards, J. J.; Erickson, J. S.; Ligler, F. S. A Simple Sheath-Flow Microfluidic Device for Micro/Nanomanufacturing: Fabrication of Hydrodynamically Shaped Polymer Fibers. *Lab Chip* **2009**, *9* (21), 3126. https://doi.org/10.1039/b910581f.

(125) Hu, M.; Kurisawa, M.; Deng, R.; Teo, C.-M.; Schumacher, A.; Thong, Y.-X.; Wang, L.; Schumacher, K. M.; Ying, J. Y. Cell Immobilization in Gelatin–Hydroxyphenylpropionic Acid Hydrogel Fibers. *Biomaterials* **2009**, *30* (21), 3523–3531. https://doi.org/10.1016/j.biomaterials.2009.03.004.

(126) Hu, M.; Deng, R.; Schumacher, K. M.; Kurisawa, M.; Ye, H.; Purnamawati, K.; Ying, J. Y. Hydrodynamic Spinning of Hydrogel Fibers. *Biomaterials* **2010**, *31* (5), 863–869. https://doi.org/10.1016/j.biomaterials.2009.10.002.

(127) Daniele, M. A.; North, S. H.; Naciri, J.; Howell, P. B.; Foulger, S. H.; Ligler, F. S.; Adams, A. A. Rapid and Continuous Hydrodynamically Controlled Fabrication of Biohybrid Microfibers. *Advanced Functional Materials* **2013**, *23* (6), 698–704. https://doi.org/10.1002/adfm.201202258.

(128) Nunes, J. K.; Constantin, H.; Stone, H. A. Microfluidic Tailoring of the Two-Dimensional Morphology of Crimped Microfibers. *Soft Matter* **2013**, *9* (16), 4227. https://doi.org/10.1039/c3sm27579e.

(129) Takei, T.; Kishihara, N.; Sakai, S.; Kawakami, K. Novel Technique to Control Inner and Outer Diameter of Calcium-Alginate Hydrogel Hollow Microfibers, and Immobilization of Mammalian Cells. *Biochemical Engineering Journal* **2010**, *49* (1), 143–147. https://doi.org/10.1016/j.bej.2009.12.012.

(130) Mazzitelli, S.; Capretto, L.; Carugo, D.; Zhang, X.; Piva, R.; Nastruzzi, C. Optimised Production of Multifunctional Microfibres by Microfluidic Chip Technology for Tissue Engineering Applications. *Lab Chip* **2011**, *11* (10), 1776. https://doi.org/10.1039/c1lc20082h.

(131) Kang, E.; Jeong, G. S.; Choi, Y. Y.; Lee, K. H.; Khademhosseini, A.; Lee, S.-H. Digitally Tunable Physicochemical Coding of Material Composition and Topography in Continuous Microfibres. *Nature Mater* **2011**, *10* (11), 877–883. https://doi.org/10.1038/nmat3108.

(132) Kang, E.; Choi, Y. Y.; Chae, S.-K.; Moon, J.-H.; Chang, J.-Y.; Lee, S.-H. Microfluidic Spinning of Flat Alginate Fibers with Grooves for Cell-Aligning Scaffolds. *Adv. Mater.* **2012**, *24* (31), 4271–4277. https://doi.org/10.1002/adma.201201232.

(133) Yeh, C.-H.; Lin, P.-W.; Lin, Y.-C. Chitosan Microfiber Fabrication Using a Microfluidic Chip and Its Application to Cell Cultures. *Microfluid Nanofluid* **2010**, *8* (1), 115–121. https://doi.org/10.1007/s10404-009-0485-7.

(134) Lee, K. H.; Shin, S. J.; Kim, C.-B.; Kim, J. K.; Cho, Y. W.; Chung, B. G.; Lee, S.-H. Microfluidic Synthesis of Pure Chitosan Microfibers for Bio-Artificial Liver Chip. *Lab Chip* **2010**, *10* (10), 1328. https://doi.org/10.1039/b924987g.

(135) Lavin, D. M.; Zhang, L.; Furtado, S.; Hopkins, R. A.; Mathiowitz, E. Effects of Protein Molecular Weight on the Intrinsic Material Properties and Release Kinetics of Wet Spun

Polymeric Microfiber Delivery Systems. *Acta Biomaterialia* **2013**, *9* (1), 4569–4578. https://doi.org/10.1016/j.actbio.2012.08.005.

(136) Lavin, D. M.; Stefani, R. M.; Zhang, L.; Furtado, S.; Hopkins, R. A.; Mathiowitz, E. Multifunctional Polymeric Microfibers with Prolonged Drug Delivery and Structural Support Capabilities. *Acta Biomaterialia* **2012**, *8* (5), 1891–1900. https://doi.org/10.1016/j.actbio.2012.01.019.

(137) Lin, Y.-S.; Huang, K.-S.; Yang, C.-H.; Wang, C.-Y.; Yang, Y.-S.; Hsu, H.-C.; Liao, Y.-J.; Tsai, C.-W. Microfluidic Synthesis of Microfibers for Magnetic-Responsive Controlled Drug Release and Cell Culture. *PLoS ONE* **2012**, *7* (3), e33184. https://doi.org/10.1371/journal.pone.0033184.

(138) Chen, C.; Chen, X.; Zhang, H.; Zhang, Q.; Wang, L.; Li, C.; Dai, B.; Yang, J.; Liu, J.; Sun, D. Electrically-Responsive Core-Shell Hybrid Microfibers for Controlled Drug Release and Cell Culture. *Acta Biomaterialia* **2017**, *55*, 434–442. https://doi.org/10.1016/j.actbio.2017.04.005.

(139) Wei, D.; Sun, J.; Bolderson, J.; Zhong, M.; Dalby, M. J.; Cusack, M.; Yin, H.; Fan, H.; Zhang, X. Continuous Fabrication and Assembly of Spatial Cell-Laden Fibers for a Tissue-Like Construct via a Photolithographic-Based Microfluidic Chip. *ACS Appl. Mater. Interfaces* **2017**, *9* (17), 14606–14617. https://doi.org/10.1021/acsami.7b00078.

(140) Wei, D.; Sun, J.; Yang, Y.; Wu, C.; Chen, S.; Guo, Z.; Fan, H.; Zhang, X. Cell Alignment Guided by Nano/Micro Oriented Collagen Fibers and the Synergistic Vascularization for Nervous Cell Functional Expression. *Materials Today Chemistry* **2018**, *8*, 85–95. https://doi.org/10.1016/j.mtchem.2018.03.001.

(141) Jia, L.; Han, F.; Yang, H.; Turnbull, G.; Wang, J.; Clarke, J.; Shu, W.; Guo, M.; Li, B. Microfluidic Fabrication of Biomimetic Helical Hydrogel Microfibers for Blood-Vessel-on-a-Chip Applications. *Adv. Healthcare Mater.* **2019**, *8* (13), 1900435. https://doi.org/10.1002/adhm.201900435.

(142) Kim, B. J.; Choi, J. Y.; Choi, H.; Han, S.; Seo, J.; Kim, J.; Joo, S.; Kim, H. M.; Oh, C.; Hong, S.; Kim, P.; Choi, I. S. Astrocyte-Encapsulated Hydrogel Microfibers Enhance Neuronal Circuit Generation. *Adv. Healthcare Mater.* **2020**, *9* (5), 1901072. https://doi.org/10.1002/adhm.201901072.

(143) Yajima, Y.; Lee, C. N.; Yamada, M.; Utoh, R.; Seki, M. Development of a Perfusable 3D Liver Cell Cultivation System via Bundling-up Assembly of Cell-Laden Microfibers. *Journal of Bioscience and Bioengineering* **2018**, *126* (1), 111–118. https://doi.org/10.1016/j.jbiosc.2018.01.022.

(144) Ebrahimi, M.; Ostrovidov, S.; Salehi, S.; Kim, S. B.; Bae, H.; Khademhosseini, A. Enhanced Skeletal Muscle Formation on Microfluidic Spun Gelatin Methacryloyl (GelMA) Fibres Using Surface Patterning and Agrin Treatment. *Journal of Tissue Engineering and Regenerative Medicine* **2018**, *12* (11), 2151–2163. https://doi.org/10.1002/term.2738.

(145) Srivastava, S.; Tirrell, M. V. Polyelectrolyte Complexation. *Advances in Chemical Physics* **2016**, *161*, 499–544. https://doi.org/10.1002/9781119290971.ch7.

(146) Decher, G. Fuzzy Nanoassemblies: Toward Layered Polymeric Multicomposites. *Science (New York, N.Y.)* **1997**, *277* (5330), 1232–1237. https://doi.org/10.1126/science.277.5330.1232.

(147) Shah, N. J.; Macdonald, M. L.; Beben, Y. M.; Padera, R. F.; Samuel, R. E.; Hammond, P. T. Tunable Dual Growth Factor Delivery from Polyelectrolyte Multilayer Films. *Biomaterials* **2011**, *32* (26), 6183–6193. https://doi.org/10.1016/j.biomaterials.2011.04.036.

(148) Cui, H.; Pan, N.; Fan, W.; Liu, C.; Li, Y.; Xia, Y.; Sui, K. Ultrafast Fabrication of Gradient Nanoporous All-Polysaccharide Films as Strong, Superfast, and Multiresponsive Actuators. *Advanced Functional Materials* **2019**, *29* (20), 1807692. https://doi.org/10.1002/adfm.201807692.

(149) Kuo, C. H.; Leon, L.; Chung, E. J.; Huang, R. T.; Sontag, T. J.; Reardon, C. A.; Getz, G. S.; Tirrell, M. V.; Fang, Y. Inhibition of Atherosclerosis-Promoting MicroRNAs via Targeted Polyelectrolyte Complex Micelles. *Journal of Materials Chemistry B* **2014**, *2* (46), 8142–8153. https://doi.org/10.1039/c4tb00977k.

(150) Voets, I. K.; de Keizer, A.; Cohen Stuart, M. A. Complex Coacervate Core Micelles. *Advances in Colloid and Interface Science* **2009**, *147–148* (C), 300–318. https://doi.org/10.1016/j.cis.2008.09.012.

(151) Srivastava, S.; Andreev, M.; Levi, A. E.; Goldfeld, D. J.; Mao, J.; Heller, W. T.; Prabhu, V. M.; de Pablo, J. J.; Tirrell, M. V. Gel Phase Formation in Dilute Triblock Copolyelectrolyte Complexes. *Nature Communications* **2017**, *8*, 14131. https://doi.org/10.1038/ncomms14131.

(152) Hunt, J. N.; Feldman, K. E.; Lynd, N. A.; Deek, J.; Campos, L. M.; Spruell, J. M.; Hernandez, B. M.; Kramer, E. J.; Hawker, C. J. Tunable, High Modulus Hydrogels Driven by Ionic Coacervation. *Advanced Materials* **2011**, *23* (20), 2327–2331. https://doi.org/10.1002/adma.201004230.

(153) Overbeek, J. T.; Voorn, M. J. Phase Separation in Polyelectrolyte Solutions; Theory of Complex Coacervation. *Journal of cellular physiology. Supplement* **1957**, *49*, 7–22. https://doi.org/10.1002/jcp.1030490404.

(154) Wang, Q.; Schlenoff, J. B. The Polyelectrolyte Complex/Coacervate Continuum. *Macromolecules* **2014**, *47* (9), 3108–3116. https://doi.org/10.1021/ma500500q.

(155) Brangwynne, C. P.; Tompa, P.; Pappu, R. V. Polymer Physics of Intracellular Phase Transitions. *Nature Physics* **2015**, *11* (11), 899–904. https://doi.org/10.1038/nphys3532.

(156) Banani, S. F.; Lee, H. O.; Hyman, A. A.; Rosen, M. K. Biomolecular Condensates: Organizers of Cellular Biochemistry. *Nature Reviews Molecular Cell Biology* **2017**, *18* (5), 285–298. https://doi.org/10.1038/nrm.2017.7.

(157) Matsusaki, M.; Sakaue, K.; Kadowaki, K.; Akashi, M. Three-Dimensional Human Tissue Chips Fabricated by Rapid and Automatic Inkjet Cell Printing. *Advanced Healthcare Materials* **2013**, *2* (4), 534–539. https://doi.org/10.1002/adhm.201200299.

(158) Wang, J.; Xue, Y. F.; Chen, X. C.; Hu, M.; Ren, K. F.; Ji, J. Humidity-Triggered Relaxation of Polyelectrolyte Complexes as a Robust Approach to Generate Extracellular Matrix Biomimetic Films. *Advanced Healthcare Materials* **2020**, *9* (14), 1–10. https://doi.org/10.1002/adhm.202000381.

(159) Rutz, A. L.; Hyland, K. E.; Jakus, A. E.; Burghardt, W. R.; Shah, R. N. A Multimaterial Bioink Method for 3D Printing Tunable, Cell-Compatible Hydrogels. *Advanced Materials* **2015**, *27* (9), 1607–1614. https://doi.org/10.1002/adma.201405076.

(160) Chen, X. C.; Ren, K. F.; Zhang, J. H.; Li, D. D.; Zhao, E.; Zhao, Z. J.; Xu, Z. K.; Ji, J. Humidity-Triggered Self-Healing of Microporous Polyelectrolyte Multilayer Coatings for

Hydrophobic Drug Delivery. *Advanced Functional Materials* **2015**, *25* (48), 7470–7477. https://doi.org/10.1002/adfm.201503258.

(161) Silva, C. L.; Pereira, J. C.; Ramalho, A.; Pais, A. A. C. C.; Sousa, J. J. S. Films Based on Chitosan Polyelectrolyte Complexes for Skin Drug Delivery: Development and Characterization. *Journal of Membrane Science* **2008**, *320* (1–2), 268–279. https://doi.org/10.1016/j.memsci.2008.04.011.

(162) Webber, M. J.; Appel, E. A.; Meijer, E. W.; Langer, R. Supramolecular Biomaterials. *Nature Materials* **2015**, *15* (1), 13–26. https://doi.org/10.1038/nmat4474.

(163) Webber, M. J.; Langer, R. Drug Delivery by Supramolecular Design. *Chemical Society Reviews* **2017**, *46* (21), 6600–6620. https://doi.org/10.1039/c7cs00391a.

(164) Sun, X.; James, T. D. Glucose Sensing in Supramolecular Chemistry. *Chemical Reviews* **2015**, *115* (15), 8001–8037. https://doi.org/10.1021/cr500562m.

(165) Newcomb, C. J.; Sur, S.; Ortony, J. H.; Lee, O. S.; Matson, J. B.; Boekhoven, J.; Yu, J. M.; Schatz, G. C.; Stupp, S. I. Cell Death versus Cell Survival Instructed by Supramolecular Cohesion of Nanostructures. *Nature Communications* **2014**, *5*, 1–10. https://doi.org/10.1038/ncomms4321.

(166) Tantakitti, F.; Boekhoven, J.; Wang, X.; Kazantsev, R. V.; Yu, T.; Li, J.; Zhuang, E.; Zandi, R.; Ortony, J. H.; Newcomb, C. J.; Palmer, L. C.; Shekhawat, G. S.; Olvera de la Cruz, M.; Schatz, G. C.; Stupp, S. I. Energy Landscapes and Functions of Supramolecular Systems. *Nature Materials* **2016**, *15* (4), 469–476. https://doi.org/10.1038/nmat4538.

(167) Lee, S. S.; Fyrner, T.; Chen, F.; Álvarez, Z.; Sleep, E.; Chun, D. S.; Weiner, J. A.; Cook, R. W.; Freshman, R. D.; Schallmo, M. S.; Katchko, K. M.; Schneider, A. D.; Smith, J. T.; Yun, C.; Singh, G.; Hashmi, S. Z.; McClendon, M. T.; Yu, Z.; Stock, S. R.; Hsu, W. K.; Hsu, E. L.; Stupp, S. I. Sulfated Glycopeptide Nanostructures for Multipotent Protein Activation. *Nature Nanotechnology* **2017**, *12* (8), 821–829. https://doi.org/10.1038/nnano.2017.109.

(168) Godbe, J. M.; Freeman, R.; Burbulla, L. F.; Lewis, J.; Krainc, D.; Stupp, S. I. Gelator Length Precisely Tunes Supramolecular Hydrogel Stiffness and Neuronal Phenotype in 3D Culture. *ACS Biomaterials Science and Engineering* **2020**, *6* (2), 1196–1207. https://doi.org/10.1021/acsbiomaterials.9b01585.

(169) Radvar, E.; Azevedo, H. S. Supramolecular Nanofibrous Peptide/Polymer Hydrogels for the Multiplexing of Bioactive Signals. *ACS Biomaterials Science and Engineering* **2019**, *5* (9), 4646–4656. https://doi.org/10.1021/acsbiomaterials.9b00941.

(170) Li, J.; Mooney, D. J. Designing Hydrogels for Controlled Drug Delivery. *Nature Reviews Materials* **2016**, *1* (12), 16071. https://doi.org/10.1038/natrevmats.2016.71.

(171) Murakami, K.; Aoki, H.; Nakamura, S.; Nakamura, S. ichiro; Takikawa, M.; Hanzawa, M.; Kishimoto, S.; Hattori, H.; Tanaka, Y.; Kiyosawa, T.; Sato, Y.; Ishihara, M. Hydrogel Blends of Chitin/Chitosan, Fucoidan and Alginate as Healing-Impaired Wound Dressings. *Biomaterials* **2010**, *31* (1), 83–90. https://doi.org/10.1016/j.biomaterials.2009.09.031.

(172) Jayakumar, R.; Prabaharan, M.; Sudheesh Kumar, P. T.; Nair, S. V.; Tamura, H. Biomaterials Based on Chitin and Chitosan in Wound Dressing Applications. *Biotechnology Advances* **2011**, *29* (3), 322–337. https://doi.org/10.1016/j.biotechadv.2011.01.005.

(173) Ottino, J. M. *The Kinematics of Mixing: Streching, Chaos, and Transport*; Cambridge University Press: Cambridge, 1989.

(174) Hobbs, D. M.; Muzzio, F. J. The Kenics Static Mixer : A Three-Dimensional Chaotic Flow. *Chemical Engineering Journal* **1997**, *67* (June 1996), 153–166.

(175) Wiggins, S.; Ottino, J. M. Foundations of Chaotic Mixing. *Philospophical Transactions of the Royal Society A* **2004**, *362*, 937–970.

(176) Moyer, T. J.; Finbloom, J. A.; Chen, F.; Toft, D. J.; Cryns, V. L.; Stupp, S. I. PH and Amphiphilic Structure Direct Supramolecular Behavior in Biofunctional Assemblies. *Journal of the American Chemical Society* **2014**, *136* (42), 14746–14752. https://doi.org/10.1021/ja5042429.

(177) Tsonchev, S.; Niece, K. L.; Schatz, G. C.; Ratner, M. A.; Stupp, S. I. Phase Diagram for Assembly of Biologically-Active Peptide Amphiphiles. *Journal of Physical Chemistry B* **2008**, *112* (2), 441–447. https://doi.org/10.1021/jp076273z.

(178) Goldberger, J. E.; Berns, E. J.; Bitton, R.; Newcomb, C. J.; Stupp, S. I. Electrostatic Control of Bioactivity. *Angewandte Chemie* **2011**, *123* (28), 6416–6419. https://doi.org/10.1002/ange.201100202.

(179) Zha, R. H.; Velichko, Y. S.; Bitton, R.; Stupp, S. I. Molecular Design for Growth of Supramolecular Membranes with Hierarchical Structure. *Soft matter* **2016**, *12*, 1401–1410. https://doi.org/10.1039/c5sm02381e.

(180) Weigand, S. J.; Keane, D. T. Nuclear Instruments and Methods in Physics Research A DND-CAT ' s New Triple Area Detector System for Simultaneous Data Collection at Multiple Length Scales. *Nuclear Inst. and Methods in Physics Research, A* **2011**, *649* (1), 61–63. https://doi.org/10.1016/j.nima.2010.12.045.

(181) Toby, B. H.; Dreele, R. B. Von. GSAS-II : The Genesis of a Modern Open-Source All Purpose Crystallography Software Package. *Journal of Applied Crystallography* **2013**, *46*, 544–549. https://doi.org/10.1107/S0021889813003531.

(182) Torres, Y.; Gluais, M.; Da Silva, N.; Rey, S.; Grémare, A.; Magnan, L.; Kawecki, F.; L'Heureux, N. Cell-Assembled Extracellular Matrix (CAM) Sheet Production: Translation from Using Human to Large Animal Cells. *J Tissue Eng* **2021**, *12*, 2041731420978327. https://doi.org/10.1177/2041731420978327.

(183) Barthold, J. E.; St. Martin, B. M.; Sridhar, S. L.; Vernerey, F.; Schneider, S. E.; Wacquez, A.; Ferguson, V. L.; Calve, S.; Neu, C. P. Recellularization and Integration of Dense Extracellular Matrix by Percolation of Tissue Microparticles. *Advanced Functional Materials* **2021**, *31* (35), 2103355. https://doi.org/10.1002/adfm.202103355.

(184) Blache, U.; Stevens, M. M.; Gentleman, E. Harnessing the Secreted Extracellular Matrix to Engineer Tissues. *Nat Biomed Eng* **2020**, *4* (4), 357–363. https://doi.org/10.1038/s41551-019-0500-6.

(185) Kular, J. K.; Basu, S.; Sharma, R. I. The Extracellular Matrix: Structure, Composition, Age-Related Differences, Tools for Analysis and Applications for Tissue Engineering. *J Tissue Eng* **2014**, *5*, 2041731414557112. https://doi.org/10.1177/2041731414557112.

(186) Nicolas, J.; Magli, S.; Rabbachin, L.; Sampaolesi, S.; Nicotra, F.; Russo, L. 3D Extracellular Matrix Mimics: Fundamental Concepts and Role of Materials Chemistry to Influence Stem Cell Fate. *Biomacromolecules* **2020**, *21* (6), 1968–1994. https://doi.org/10.1021/acs.biomac.0c00045.

(187) Jun, H.-W.; Yuwono, V.; Paramonov, S. E.; Hartgerink, J. D. Enzyme-Mediated Degradation of Peptide-Amphiphile Nanofiber Networks. *Advanced Materials* **2005**, *17* (21), 2612–2617. https://doi.org/10.1002/adma.200500855.

(188) Jeong, S. H.; Kim, M.; Kim, T. Y.; Kim, H.; Ju, J. H.; Hahn, S. K. Supramolecular Injectable Hyaluronate Hydrogels for Cartilage Tissue Regeneration. *ACS Appl. Bio Mater.* **2020**, *3* (8), 5040–5047. https://doi.org/10.1021/acsabm.0c00537.

(189) Jeong, S. H.; Kim, M.; Kim, T. Y.; Choi, H.; Hahn, S. K. Biomimetic Supramolecular Drug Delivery Hydrogels for Accelerated Skin Tissue Regeneration. *ACS Biomater. Sci. Eng.* **2021**, *7* (9), 4581–4590. https://doi.org/10.1021/acsbiomaterials.1c00705.

(190) Wang, Y.; Zhao, Q.; Zhang, H.; Yang, S.; Jia, X. A Novel Poly(Amido Amine)-Dendrimer-Based Hydrogel as a Mimic for the Extracellular Matrix. *Advanced Materials* **2014**, *26* (24), 4163–4167. https://doi.org/10.1002/adma.201400323.

(191) Bella, A.; Ray, S.; Shaw, M.; Ryadnov, M. G. Arbitrary Self-Assembly of Peptide Extracellular Microscopic Matrices. *Angewandte Chemie International Edition* **2012**, *51* (2), 428–431. https://doi.org/10.1002/anie.201104647.

(192) Chow, L. W.; Wang, L.; Kaufman, D. B.; Stupp, S. I. Self-Assembling Nanostructures to Deliver Angiogenic Factors to Pancreatic Islets. *Biomaterials* **2010**, *31* (24), 6154–6161. https://doi.org/10.1016/j.biomaterials.2010.04.002.

(193) Lombardo, D.; Calandra, P.; Pasqua, L.; Magazù, S. Self-Assembly of Organic Nanomaterials and Biomaterials: The Bottom-Up Approach for Functional Nanostructures Formation and Advanced Applications. *Materials* **2020**, *13* (5), 1048. https://doi.org/10.3390/ma13051048.

(194) Varanko, A.; Saha, S.; Chilkoti, A. Recent Trends in Protein and Peptide-Based Biomaterials for Advanced Drug Delivery. *Advanced Drug Delivery Reviews* **2020**, *156*, 133–187. https://doi.org/10.1016/j.addr.2020.08.008.

(195) Kim, B. S.; Kim, H.; Gao, G.; Jang, J.; Cho, D.-W. Decellularized Extracellular Matrix: A Step towards the next Generation Source for Bioink Manufacturing. *Biofabrication* **2017**, *9* (3), 034104. https://doi.org/10.1088/1758-5090/aa7e98.

(196) Stendahl, J. C.; Kaufman, D. B.; Stupp, S. I. Extracellular Matrix in Pancreatic Islets: Relevance to Scaffold Design and Transplantation. *Cell Transplant* **2009**, *18* (1), 1–12. https://doi.org/10.3727/096368909788237195.

(197) Sather, N. A.; Sai, H.; Sasselli, I. R.; Sato, K.; Ji, W.; Synatschke, C. V.; Zambrotta, R. T.; Edelbrock, J. F.; Kohlmeyer, R. R.; Hardin, J. O.; Berrigan, J. D.; Durstock, M. F.; Mirau, P.; Stupp, S. I. 3D Printing of Supramolecular Polymer Hydrogels with Hierarchical Structure. *Small* **2021**, *17* (5), 2005743. https://doi.org/10.1002/smll.202005743.

(198) Ulijn, R. V.; Lampel, A. Order/Disorder in Protein and Peptide-Based Biomaterials. *Israel Journal of Chemistry* **2020**, *60* (12), 1129–1140. https://doi.org/10.1002/ijch.201900051.

(199) Montanero, J. M.; Gañán-Calvo, A. M. Dripping, Jetting and Tip Streaming. *Rep. Prog. Phys.* **2020**, *83* (9), 097001. https://doi.org/10.1088/1361-6633/aba482.

(200) Armstrong, M.; Vahey, M. D.; Hunt, T. P.; Fletcher, D. A. Forming and Loading Giant Unilamellar Vesicles with Acoustic Jetting. *Biomicrofluidics* **2020**, *14* (6), 064105. https://doi.org/10.1063/5.0021742.

(201) Li, Y.; Zhu, T.; Wang, L.; Jiang, J.; Xie, G.; Huangfu, X.; Dong, S.; Zhao, J. Tissue-Engineered Decellularized Allografts for Anterior Cruciate Ligament Reconstruction. *ACS Biomater. Sci. Eng.* **2020**, *6* (10), 5700–5710. https://doi.org/10.1021/acsbiomaterials.0c00269.

(202) Amini, Z.; Lari, R. A Systematic Review of Decellularized Allograft and Xenograft–Derived Scaffolds in Bone Tissue Regeneration. *Tissue and Cell* **2021**, *69*, 101494. https://doi.org/10.1016/j.tice.2021.101494.

(203) Rubert Pérez, C. M.; Álvarez, Z.; Chen, F.; Aytun, T.; Stupp, S. I. Mimicking the Bioactivity of Fibroblast Growth Factor-2 Using Supramolecular Nanoribbons. *ACS Biomater. Sci. Eng.* **2017**, *3* (9), 2166–2175. https://doi.org/10.1021/acsbiomaterials.7b00347.

(204) Kassam, H. A.; Bahnson, E. M.; Cartaya, A.; Jiang, W.; Avram, M. J.; Tsihlis, N. D.; Stupp, S. I.; Kibbe, M. R. Pharmacokinetics and Biodistribution of a Collagen-targeted Peptide Amphiphile for Cardiovascular Applications. *Pharmacol. Res. Perspect.* **2020**, *8* (6). https://doi.org/10.1002/prp2.672.

(205) Berns, E. J.; Álvarez, Z.; Goldberger, J. E.; Boekhoven, J.; Kessler, J. A.; Kuhn, H. G.; Stupp, S. I. A Tenascin-C Mimetic Peptide Amphiphile Nanofiber Gel Promotes Neurite Outgrowth and Cell Migration of Neurosphere-Derived Cells. *Acta Biomaterialia* **2016**, *37*, 50–58. https://doi.org/10.1016/j.actbio.2016.04.010.

(206) Bury, M. I.; Fuller, N. J.; Clemons, T. D.; Sturm, R. M.; Morrison, C. D.; Lisy-Snow, D. C.; Nolan, B. G.; Tarczynski, C.; Ayello, E. M. T.; Boyce, A.; Muckian, B.; Ahmad, N.; Hunter, C. J.; Karver, M. R.; Stupp, S. I.; Sharma, A. K. Self-Assembling Nanofibers Inhibit Inflammation in a Murine Model of Crohn's-Disease-Like Ileitis. *Adv. Therap.* **2021**, *4* (4), 2000274. https://doi.org/10.1002/adtp.202000274.

(207) Stendahl, J. C.; Wang, L.-J.; Chow, L. W.; Kaufman, D. B.; Stupp, S. I. Growth Factor Delivery From Self-Assembling Nanofibers to Facilitate Islet Transplantation. *Transplantation* **2008**, *86* (3), 478–481. https://doi.org/10.1097/TP.0b013e3181806d9d.

(208) Bond, C. W.; Angeloni, N. L.; Harrington, D. A.; Stupp, S. I.; McKenna, K. E.; Podlasek, C. A. Peptide Amphiphile Nanofiber Delivery of Sonic Hedgehog Protein to Reduce Smooth Muscle Apoptosis in the Penis after Cavernous Nerve Resection. *The Journal of Sexual Medicine* **2011**, *8* (1), 78–89. https://doi.org/10.1111/j.1743-6109.2010.02001.x.

(209) Lucaciu, O. P.; Soritau, O.; Baciut, G.; Lucaciu, D.; Baciut, M.; Campian, R.; Bran, S. The Role of Bone Morphogenetic Proteins in Tissue Engineering Particulate Bone Grafts. *Particulate Science and Technology* **2014**, *32* (4), 377–383. https://doi.org/10.1080/02726351.2013.879462.

(210) Borena, B. M.; Martens, A.; Broeckx, S. Y.; Meyer, E.; Chiers, K.; Duchateau, L.; Spaas, J. H. Regenerative Skin Wound Healing in Mammals: State-of-the-Art on Growth Factor and Stem Cell Based Treatments. *Cell Physiol Biochem* **2015**, *36* (1), 1–23. https://doi.org/10.1159/000374049.

(211) Álvarez, Z.; Kolberg-Edelbrock, A. N.; Sasselli, I. R.; Ortega, J. A.; Qiu, R.; Syrgiannis, Z.; Mirau, P. A.; Chen, F.; Chin, S. M.; Weigand, S.; Kiskinis, E.; Stupp, S. I. Bioactive Scaffolds with Enhanced Supramolecular Motion Promote Recovery from Spinal Cord Injury. *Science* **2021**, *374* (6569), 848–856. https://doi.org/10.1126/science.abh3602.

(212) Bastings, M. M. C.; Koudstaal, S.; Kieltyka, R. E.; Nakano, Y.; Pape, A. C. H.; Feyen, D. A. M.; van Slochteren, F. J.; Doevendans, P. A.; Sluijter, J. P. G.; Meijer, E. W.;

Chamuleau, S. A. J.; Dankers, P. Y. W. A Fast PH-Switchable and Self-Healing Supramolecular Hydrogel Carrier for Guided, Local Catheter Injection in the Infarcted Myocardium. *Advanced Healthcare Materials* **2014**, *3* (1), 70–78. https://doi.org/10.1002/adhm.201300076.

(213) Webber, M. J.; Appel, E. A.; Meijer, E. W.; Langer, R. Supramolecular Biomaterials. *Nature Mater* **2016**, *15* (1), 13–26. https://doi.org/10.1038/nmat4474.

(214) Yoon, H.-J.; Jang, W.-D. Polymeric Supramolecular Systems for Drug Delivery. *J. Mater. Chem.* **2010**, *20* (2), 211–222. https://doi.org/10.1039/B910948J.

(215) Rösler, A.; Vandermeulen, G. W. M.; Klok, H.-A. Advanced Drug Delivery Devices via Self-Assembly of Amphiphilic Block Copolymers. *Advanced Drug Delivery Reviews* **2012**, *64*, 270–279. https://doi.org/10.1016/j.addr.2012.09.026.

(216) Webber, M. J.; Pashuck, E. T. (Macro)Molecular Self-Assembly for Hydrogel Drug Delivery. *Advanced Drug Delivery Reviews* **2021**, *172*, 275–295. https://doi.org/10.1016/j.addr.2021.01.006.

(217) Lee, S. S.; Fyrner, T.; Chen, F.; Álvarez, Z.; Sleep, E.; Chun, D. S.; Weiner, J. A.; Cook, R. W.; Freshman, R. D.; Schallmo, M. S.; Katchko, K. M.; Schneider, A. D.; Smith, J. T.; Yun, C.; Singh, G.; Hashmi, S. Z.; McClendon, M. T.; Yu, Z.; Stock, S. R.; Hsu, W. K.; Hsu, E. L.; Stupp, S. I. Sulfated Glycopeptide Nanostructures for Multipotent Protein Activation. *Nature Nanotech* **2017**, *12* (8), 821–829. https://doi.org/10.1038/nnano.2017.109.

(218) Sur, S.; Tantakitti, F.; Matson, J. B.; Stupp, S. I. Epitope Topography Controls Bioactivity in Supramolecular Nanofibers. *Biomater. Sci.* **2015**, *3* (3), 520–532. https://doi.org/10.1039/C4BM00326H.

(219) Mercel, A. I.; Marulanda, K.; Gillis, D. C.; Sun, K.; Clemons, T. D.; Willcox, S.; Griffith, J.; Peters, E. B.; Karver, M. R.; Tsihlis, N. D.; Maile, R.; Stupp, S. I.; Kibbe, M. R. Development of Novel Nanofibers Targeted to Smoke-Injured Lungs. *Biomaterials* **2021**, *274*, 120862. https://doi.org/10.1016/j.biomaterials.2021.120862.

(220) Arslan, E.; Sardan Ekiz, M.; Eren Cimenci, C.; Can, N.; Gemci, M. H.; Ozkan, H.; Guler, M. O.; Tekinay, A. B. Protective Therapeutic Effects of Peptide Nanofiber and Hyaluronic

Acid Hybrid Membrane in in Vivo Osteoarthritis Model. *Acta Biomaterialia* **2018**, *73*, 263–274. https://doi.org/10.1016/j.actbio.2018.04.015.

(221) Cotey, T. J.; Sai, H.; Perez, C.; Palmer, L. C.; Stupp, S. I. Hybrid Gels *via* Bulk Interfacial Complexation of Supramolecular Polymers and Polyelectrolytes. *Soft Matter* **2021**, *17* (19), 4949–4956. https://doi.org/10.1039/D1SM00168J.

(222) Takeuchi, S.; Garstecki, P.; Weibel, D. B.; Whitesides, G. M. An Axisymmetric Flow-Focusing Microfluidic Device. *Advanced Materials* **2005**, *17* (8), 1067–1072. https://doi.org/10.1002/adma.200401738.

(223) Anna, S. L.; Bontoux, N.; Stone, H. A. Formation of Dispersions Using "Flow Focusing" in Microchannels. *Appl. Phys. Lett.* **2003**, *82* (3), 364–366. https://doi.org/10.1063/1.1537519.

(224) Lu, M.; Ozcelik, A.; Grigsby, C. L.; Zhao, Y.; Guo, F.; Leong, K. W.; Huang, T. J. Microfluidic Hydrodynamic Focusing for Synthesis of Nanomaterials. *Nano Today* **2016**, *11* (6), 778–792. https://doi.org/10.1016/j.nantod.2016.10.006.

VITA

Thomas Cotey

EDUCATION

Northwestern University, Evanston, IL:
PhD Candidate, Materials Science and Engineering, GPA: 3.78/4.00
Honors: National Science Foundation Graduate Research Fellow
Certificate: Management for Scientists and Engineers, Kellogg School of Management
Case Western Reserve University, Cleveland, OH: May 2016
BSE, magna cum laude, Polymer Science and Engineering, Chemistry Minor, GPA: 3.87/4.00
Honors: The Macromolecular Senior Achievement Award, Tau Beta Pi Engineering Honor Society

EXPERIENCE

Graduate Researcher: October 2016 - Present
Stupp Research Group – Materials Science and Engineering – Northwestern University

- Directed collaborative interdisciplinary projects focused on developing novel materials for biomedical applications formed via polyelectrolyte complexation between engineered surfactants and polymers using bulk flow and microfluidic devices
- Supervised and trained undergraduate engineering students in experimental design, data analysis, technical communication, and materials characterization
- Managed laboratory equipment for >40 users (lyophilizer and microfluidics system), developed written protocols, coordinated one-on-one trainings, performed maintenance and troubleshooting
- Conducted design of experiments, optimized materials synthesis, performed materials characterization using a variety of instruments and techniques, managed laboratory equipment, coordinated trainings

Undergraduate Researcher: January 2015 – May 2016
Korley Research Group – Macromolecular Science and Engineering - CWRU

- Produced and analyzed low molecular weight gels and polymer blends

Research Experience for Undergraduates Summer Researcher: May 2015 - August 2015
Davis Research Group – Macromolecules and Interfaces Institute - Virginia Tech

- Developed and examined drug loaded polymer nanoparticles

Undergraduate Researcher: January 2014 - December 2014
Karathanasis Research Group – Biomedical Engineering - CWRU

- Synthesized and characterized nanoparticles and liposomes for targeting and treatment of metastatic cancer

PUBLICATIONS AND PRESENTATIONS

- J. Kolberg-Edelbrock*, **T. Cotey***, S. Ma, G.M. Kapsalis, D.M. Bondoc, S.R. Lee, A. Kolberg-Edelbrock, S.I. Stupp, "Extracellular mimetic scaffolds by microfluidic superstructuring of nanofibers," *In Preparation*
- **T. Cotey***, Jack Kolberg-Edelbrock*, S. Ma, Garifalia M. Kapsalis, S.R. Lee, E. Bruckner, D.M. Bondoc, S.I. Stupp, "Microfluidic superstructuring of biomaterials based on covalent and supramolecular polymers," *In Preparation*
- O. Dumele,* L. Đorđević,* H. Sai, **T. Cotey**, H. Sangji, K. Sato, A. Dannenhoffer, S.I. Stupp, " Photocatalytic Aqueous CO_2 Reduction to CO and CH_4 Sensitized by Ullazine Supramolecular Polymers" *Journal of the American Chemical Society*, volume 144, pages 3127-3136, 2022. doi.org/10.1021/jacs.1c12155
- **T. Cotey**, H. Sai, C. Perez, L.C. Palmer, S.I. Stupp "Hybrid Gels Via Interfacial Complexation of Peptide Amphiphiles and Polyelectrolytes," *Soft Matter,* volume 17, pages 4949-4956, 2021. doi: 10.1039/D1SM00168J
- Presentation: "Gels Via Interfacial Complexation of Peptide Amphiphiles and Polyelectrolytes," ACS Spring National Meeting 2020, doi.org/10.1021/scimeetings.0c06462
- Poster Presentation: "Design and Fabrication of Chitosan Nanoparticles for the Delivery of Rosmarinic Acid" at Polymers in Medicine and Biology, 2015, Sonoma Valley, CA.
- P.M. Peiris, P. Deb, E. Doolittle, G. Doron, A. Goldberg, P. Govender, S. Shah, S. Rao, S. Carbone, **T. Cotey**, M. Sylvestre, S. Singh, W.P. Schiemann, Z. Lee, E. Karathanasis, "Vascular Targeting of a Gold Nanoparticle to Breast Cancer Metastasis," *Journal of Pharmaceutical Sciences*, volume 104, Issue 8, pages 2600–2610, 2015. doi: 10.1002/jps.24518

MATERIALS CHARACTERIZATION TECHNIQUES

- Rheometry
- Confocal Microscopy
- Polarized Optical Microscopy
- SEM
- DLS
- Zeta Potential
- TGA
- DSC
- Absorbance Spectroscopy
- Fluorescence Spectroscopy

TEACHING

- Led discussion sessions, performed demonstrations, developed course materials, led technical writing and communication sessions, directed review sessions, proctored exams, conducted evaluations

Courses:

Teaching Assistant: Spring 2021
Soft Materials - Materials Science and Engineering - NU

Teaching Assistant: Fall 2019
Principles of the Properties of Materials - Materials Science and Engineering - NU

Teaching Assistant: Spring 2016
Polymer Properties and Design - Macromolecular Science and Engineering - CWRU

LEADERSHIP AND COMMUNITY

Volunteer Tutor: Fall 2020
Chicago Boys and Girls Club

- Developed individualized lesson plans for Chicago Public Schools middle school students

Graduate Student Mentor: 2020 and Summer 2018
Northwestern University Materials Science and Engineering:

- Mentored undergraduate engineering students in conducting materials characterization, experimental design, data analysis, technical writing, and communication

Mentor: Fall 2018 – Summer 2019
Materials Science Alliance for an Inclusive Community - Northwestern University

- Fostered relationship with a first year Northwestern graduate student and provided mentorship on getting acclimated to and succeeding in graduate school

Volunteer and Outreach Chair: June 2017 – June 2018
Materials Science Student Association – Northwestern University

- Organized 4 fundraisers and raised $3000 for non-profit charitable organizations
- Coordinated Materials Science and Engineering department Letters to a Prescientist pen-pal program

Scientist Pen Pal: 2017 – 2021
Letters to a Prescientist

- Fostered connections with students from high-poverty schools to broaden scientific awareness and inspire students to consider STEM careers

Science Mentor: Fall 2016
Junior Science Club – Northwestern University

- Conducted hands on experiments and demonstrations with elementary and middle school students at a Chicago Boys and Girls Club to encourage interest in science and engineering

Science Mentor: Summer 2015
Youth Experiencing Science – Virginia Tech

- Designed activities to improve understanding of scientific principles and worked with elementary school students to increase interest in science education

AWARDS

- NSF Graduate Research Fellowship 2018
- NSF Graduate Research Fellowship Honorable Mention 2016
- The Macromolecular Senior Achievement Award 2016
- Member of Tau Beta Pi Engineering Honor Society
- CWRU Dean's List High Honors: Spring 2013, 2014, 2015, 2016; Fall 2013, 2014, 2015
- 2nd Place National Biomaterials Education Challenge 2014